UNIVERSIDAD AUTÓNOMA DE BAJA CALIFORNIA
FACULTAD DE CIENCIAS MARINAS
INSTITUTO DE INVESTIGACIONES OCEANOLÓGICAS

DOCTORADO EN CIENCIAS EN OCEANOGRAFÍA COSTERA

COMPORTAMIENTO CÍCLICO DEL SISTEMA BARRA-BERMA EN UNA PLAYA DOMINADA POR OLEAJE REMOTO: OBSERVACIONES Y MODELACIÓN

TESIS

QUE PARA CUBRIR PARCIALMENTE LOS REQUISITOS NECESARIOS
PARA OBTENER EL GRADO DE DOCTOR

PRESENTA

TADASHI KONO MARTÍNEZ

Ensenada, Baja California, México
Junio 2025

FACULTAD DE CIENCIAS MARINAS

INSTITUTO DE INVESTIGACIONES OCEANOLÓGICAS

POSGRADO EN OCEANOGRAFIA COSTERA

COMPORTAMIENTO CÍCLICO DEL SISTEMA BARRA-BERMA EN UNA PLAYA DOMINADA POR OLEAJE REMOTO: OBSERVACIONES Y MODELACIÓN

TESIS

QUE PARA CUBRIR PARCIALMENTE LOS REQUISITOS NECESARIOS
PARA OBTENER EL GRADO DE

DOCTOR EN CIENCIAS EN OCEANOGRAFÍA COSTERA

PRESENTA:

TADASHI KONO MARTÍNEZ

Aprobada por:

Dra. Amaia Ruiz de Alegría Arzaburu
Directora de tesis

Giovanni Co

Dr. Giovanni Coco
Sinodal

Dr. Ismael de Jesús Mariño Tapia
Sinodal

Dr. Hector García Nava
Sinodal

Dra. Cira Gabriela Montaño Moctezuma
Sinodal

INDEX

Resumen

Este estudio analiza los procesos físicos que controlan la morfodinámica de la playa arenosa de La Misión (Baja California), de 2 km de longitud, con énfasis en la variabilidad estacional y espacial del sistema morfológico barra-berma. El objetivo es comprender los mecanismos de intercambio sedimentario entre la berma y la barra submareal, en relación con las condiciones hidrodinámicas (oleaje, corrientes y mareas), así como caracterizar los patrones de circulación costera bajo diferentes configuraciones morfológicas estacionales. Para ello, se analizaron mediciones morfológicas mensuales recolectadas entre 2015 y 2020, que incluyen 27 perfiles batimétricos y 32 topográficos, complementados con datos de oleaje obtenidos mediante un ADCP ubicado a 20 m de profundidad y 2 km mar adentro. Adicionalmente, durante un periodo de dos semanas se midieron corrientes con tres ADCPs instalados a 4 m de profundidad en la zona cercana a la rompiente. Los datos revelaron un ciclo estacional en el sistema berma-barra: las bermas se forman durante periodos de baja energía, se erosionan bajo condiciones energéticas altas, y se reconstruyen en condiciones moderadas. De forma complementaria, las barras submareales se desarrollan cuando las bermas se erosionan, migran mar adentro con el incremento del oleaje y regresan hacia la costa al disminuir la energía, aportando sedimento a la reconstrucción de la berma. Aunque este ciclo se repite anualmente, presenta variaciones espaciales. En el sector sur, la barra submareal permanece más tiempo alejada de la costa debido a flujos persistentes hacia mar adentro (-0.2 m/s). En contraste, en el norte predominan flujos débiles hacia tierra (~0.1 m/s), lo que favorece una reconstrucción más rápida de la berma. Además, el oleaje en el norte es menos energético que en el sur. Para caracterizar la circulación costera bajo distintas configuraciones morfológicas, se implementó el modelo numérico XBeach en modo Surfbeat, validado con mediciones de corrientes cercanas a la rompiente. Los resultados indican dos patrones principales de circulación: fuera de la zona de rompiente, las corrientes están dominadas por la marea, mientras que dentro de la rompiente, la dirección del oleaje controla las corrientes longitudinales. En condiciones de oleaje en calma, la asimetría positiva del oleaje puede facilitar el retorno de sedimento desde mar adentro hacia la playa, siendo la marea quien determina la sección de la costa que recibe mayor aporte. Dentro de la rompiente, las corrientes inducidas por oleaje transportan el sedimento hacia el norte si el oleaje proviene del suroeste, o hacia el sur si proviene del noroeste. Durante verano-otoño, se observan flujos longitudinales hacia el norte, sin barra y con oleaje suroeste, lo que favorece el crecimiento de la berma en el norte. En invierno, el oleaje es más energético y perpendicular, con presencia de barra mar adentro, reduciendo flujos longitudinales y promoviendo corrientes transversales. En primavera, los flujos longitudinales vuelven a intensificarse hacia el norte, pero la presencia de una barra cercana a la rompiente en el sur genera corrientes de retorno, disminuyendo la variabilidad a lo largo de la costa.

Palabras clave: XBeach, sesgo, resaca, corrientes de retorno, oleaje, berma y barra.

Abstract

This study examines the physical processes driving the morphodynamics of La Misión, a sandy, semi-enclosed beach in Baja California, with a focus on the seasonal variability of the berm–bar morphological system. The objective is to improve the understanding of sediment exchange between the berm and the subtidal sandbar in relation to hydrodynamic conditions —waves, currents, and tides—on seasonal to interannual timescales, and to characterize circulation patterns associated with different seasonal morphological configurations. Between 2015 and 2020, monthly morphological measurements were collected, including 27 bathymetric and 32 topographic beach profiles, along with wave measurements from an ADCP deployed at 20 m depth, 2 km offshore. Additionally, nearshore currents were measured over a two-week period using three ADCPs installed at a depth of 4 m. Analysis revealed a seasonal cycle in the berm–bar system: berms typically formed during low-energy conditions, eroded during high-energy events, and rebuilt during moderate-energy conditions as sandbars migrated shoreward. Sandbars formed when berms were eroded and migrated offshore by high-energy waves; as wave energy decreased, these sandbars returned to the shore, supplying sediment for berm recovery. While this cycle repeated annually, spatial variability was evident. In the southern beach, sandbars remained offshore longer due to stronger offshore-directed flows (0.3 – 0.8 m/s). In contrast, the northern section exhibited weaker onshore flows (~0.1 m/s), facilitating quicker onshore sandbar migration and berm reconstruction. Wave energy was also lower in the north (Hs approximately 0.3 m lower), suggesting enhanced energy dissipation and sediment accumulation. To characterize circulation under different morphological states, the XBeach numerical model was implemented in Surfbeat mode and validated with nearshore measurements. The model identified two dominant circulation regimes: offshore of the surf zone, currents were primarily tide-driven, while within the surf zone, wave direction controlled alongshore flows. The northern section was characterized by frequently onshore flows, while the southern section by offshore flows in mostly of the seasons due to the headland. During calm wave conditions, offshore stored sediment could return to the beach due to positive wave skewness beyond the surf zone, but tidally-induced current direction determined the beach section receiving sediment input. Inside the surf zone, wave-induced currents dominated sediment transport—northward under southwestern waves and southward under northwestern waves. Circulation patterns varied seasonally. Low-energy conditions in summer-autumn and the absence of a sandbar resulted in dominant northward flows favoring a faster recovery in the berm at the north. In winter, higher wave energy, shore-normal wave incidence, and an offshore sandbar reduced alongshore flows and enhanced cross-shore currents through sandbar gaps. In spring, lower wave energy and southwestern to western wave directions favored alongshore flows in the northern section, where no sandbar was present. Meanwhile, in the southern section, a nearshore sandbar intensified offshore-directed cross-shore flows, leading to rip current formation.

Keywords: XBeach, skewness, undertow, rip currents, waves, berm and sandbar

LIST OF FIGURES

LIST OF TABLES

AGRADECIMIENTOS

A la Dra. Amaia Ruíz de Alegría Arzaburu por su excepcional dedicación y paciencia en instruirme a mi manera en **cómo** divulgar y ejercer la ciencia. Por resaltar lo que es ser un investigador comprometido, constante y responsable, que da lo mejor de si en todo momento y ante cualquier circunstancia.

Al Dr. Giovanni Coco por su paciencia y sus comentarios consistentes durante el desarrollo del Doctorado. Al Dr. Ismael Mariño por su humildad y objetividad durante las evaluaciones del proyecto y valiosos consejos. Al Dr. Hector Garcia por su tiempo en atender mis dudas. A la Dra. Gaby Montaño, por sus grandes consejos de como divulgar el mensaje científico.

Al Dr. Adán Mejía por su siempre buena disposición en brindarme apoyo, animo y su gran amistad.

Al equipo técnico de MORDICS aunque ya no estén todos pero fueron parte de cuando inicie el Doctorado: Ernesto Carsolio, Julio López, Adrián Vidal, Eduardo Gil, Angélica Romero, Efraín Chávez, Berenice Soto, Martin Vizcarra, David Gracia, Beatriz Gasalla, Arantxa Villa por haber hecho posible este trabajo y sobre todo, por su gran amistad y disposición en todo momento que fue requerido.

A mis amigos cercanos Ari, Alex, Alicia, Javi, Fatima, Sandy, Manuel, Mauricio, Mario y Geral, por su apoyo moral y emocional y las buenas reuniones sociales para sobrellevar los problemas de esta vida.

A mis padres, por todo su apoyo emocional y económico, sobre todo la última etapa del Doctorado, mis guías y ejemplos a seguir en esta vida. A mis hermanos de igual manera por su apoyo moral.

A mi amada pareja Reyna Xochitl, por todo su apoyo emocional durante todo el Doctorado, por su bello espíritu alegre y perfecto en el amor, por ser mi refugio de paz, mi inspiración y compañera de vida.

A mis mascotas Jazz y Yuba+ por acompañarme a lo largo del proceso, a pesar de los días largos y pesados, siempre han estado para aliviar esas penas o dolor.

Agradecimiento a SECIHTI por la beca otorgada (**CVU: 600001**) y al proyecto UC-MEXUS CN-18-179 **Y** CONACyT CB-2014-238765 por el apoyo económico para el desarrollo de esta investigación.

CHAPTER 1. Introduction / Introducción

This chapter provides a concise overview of sandy beach morphodynamics, with a particular focus on beaches where cross-shore sediment transport predominates. The primary goal of this research is to enhance the understanding of sediment exchange between subaerial and subtidal morphological features, such as berms and sandbars, over seasonal to interannual time scales. Therefore, this section offers background information on the dynamics of these features.

Este capítulo provee una concisa descripción general de la morfodinámica de playas de arena, enfocándose en la dominancia del transporte transversal de los sedimentos. La principal meta de esta investigación es mejorar el entendimiento del intercambio de sedimento entre los rasgos morfológicos de la parte subaérea y submareal como son las bermas y barras submareales en escalas de tiempo desde estacional a interanual Por lo que esta sección ofrece antecedentes sobre la dinámica de estos rasgos.

1.1. Sandy beach morphodynamics / Morfodinámica de playas de arena

The beach acts as a dynamic interface between the land and the sea, offering a unique space for a variety of recreational, touristic, nautical, and fishing activities. A beach is generally defined as an accumulation of sediment (sand, gravel, pebbles) that is constantly reshaped by waves and tidal forces. The interaction between the morphological shape of the beach and the hydrodynamics generated by the wind, tides, waves and currents is known as beach morphodynamics. The dynamic nature of the beach not only supports diverse biodiversity (Defeo et al., 2009; Amaral et al., 2016), but also plays a fundamental role in coastal ecosystem conservation, as its morphological characteristics influence coastal resilience.

The beach is divided into three sections based on wave processes: the offshore zone, surf zone and swash zone (Figure 1.1), and each section displays unique morphological features. Sandbars, formed by the complex interaction between waves and currents, are identified as amplifications of the elevation of the beach profile (Figure 1.1), and these features are typically indicative of the morphodynamic state of the beach. Sandbars can be located in the subtidal section between the surf and swash zone, or in the intertidal beach and influenced by the tidal cycle (Holman & Bowen, 1982; van Maanen et al., 2008; Ruessink et al., 2009; Aagaard et al., 2013; van de Lageweg et al., 2013a; Splinter et al., 2018; Phillips et al., 2019). Typically located immediately above the spring high tide line, berms are constructional morphological features with a triangular cross-section and a quasi-planar surface that extend seaward from the dune toe, often separated by a distinctive slope change from the steeper beachface (King, 1959; Hine, 1979; Masselink & Hughes, 2003).

Sandbars constitute the first line of defense against coastal erosion and inundation and are considered important sand reservoirs for the nearshore sediment budget; thus, contributing to coastal resilience (Senechal et al., 2015).

Sandbars migrate across the beach in relation to the incoming wave energy, and often associated with berm removal or reconstruction. When the wave energy is low and persistent over several weeks or months, subtidal sandbars tend to migrate landwards, later allowing berm reconstruction. Instead, high-energy conditions induce berm erosion, and the formation and offshore migration of the sandbar. Thus, the energy of waves determines the distribution of the sediment across the beach, which is often analyzed through the size and location of subtidal sandbars (Ruessink et al., 2009; Vidal-Ruiz & Ruiz de Alegría-Arzaburu, 2019, 2020).

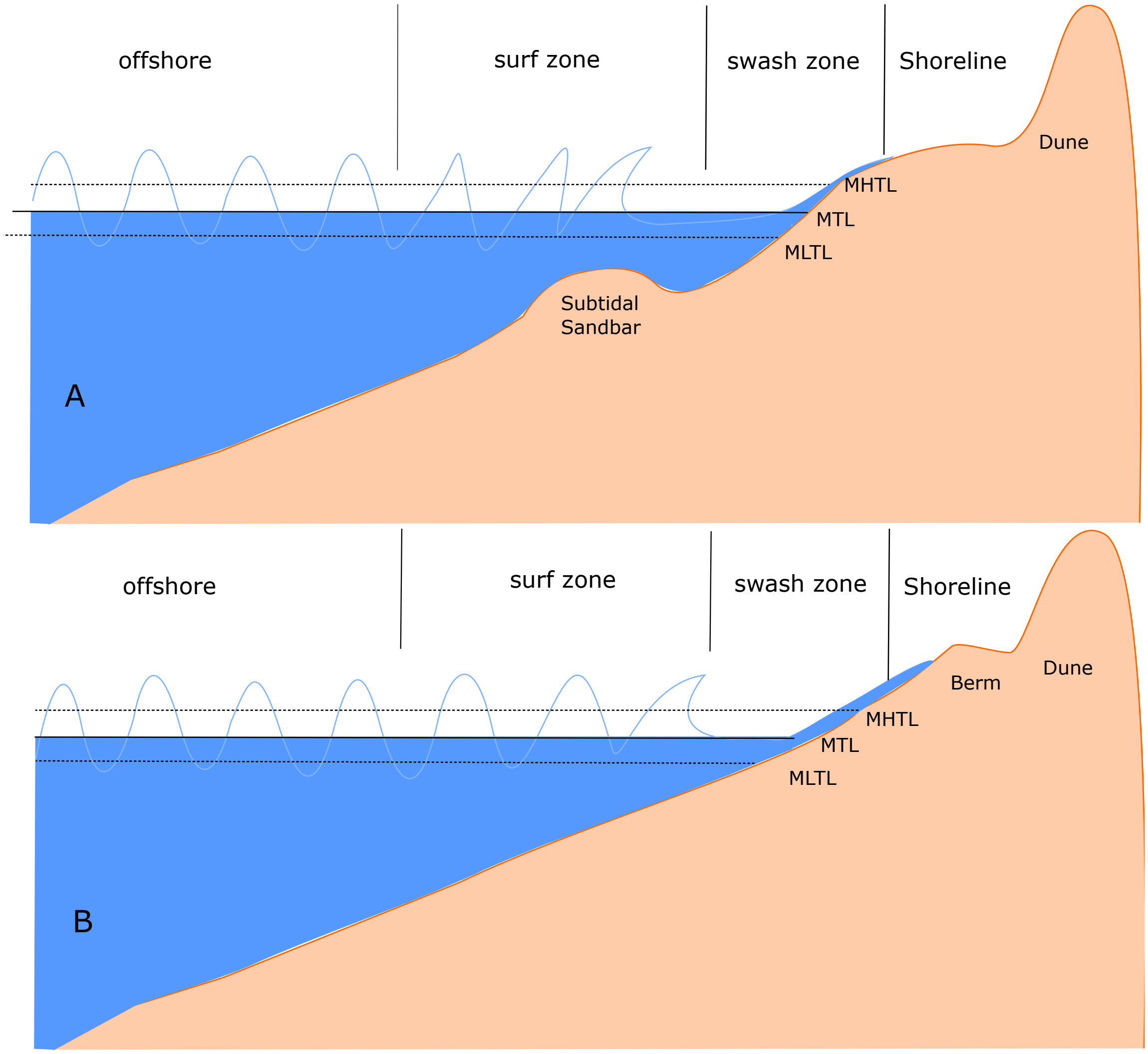

Figure 1.1 Schematic diagram of the beach profile from the shoaling zone (offshore) to the dunes, highlighting the main morphological features: sandbars, berms and dunes. (A) Typical winter beach profile and (B) Typical summer beach profile for sandy beaches. MLTL = Mean Low Tide Level; MTL = Mean Tide Level and MHTL = Mean High Tide Level.

Figura 1.1 Diagrama esquemático del perfil de playa desde la zona de asomeramiento hasta las dunas, denotando los principales rasgos morfológicos: barras submareales, bermas y dunas. (A) Perfil de playa típico de invierno y (B) perfil de playa típico de verano para playas de arena. BMI = Bajamar Media Inferior; NMM = Nivel Medio del Mar y PMS = Pleamar Media Superior.

The beaches in California and Baja California are highly seasonal, in response to the incoming wave characteristics. Shepard (1950) was one of the earliest researchers describing the seasonality of sandy beaches. He showed that higher energy winter waves erode the upper beach, narrowing the berm and forming a sandbar, while the summer lower energy waves induce beach accretion, thus, sandbar erosion and the formation of a wider berm. The width of the berm changed with the tidal range, being narrower during spring tides and wider during neap tides. More recently, Ruiz de Alegría-Arzaburu et al. (2017) indicated a similar seasonal behavior of Ensenada Beach in Baja California and demonstrated that the subaerial beach (above MLLT; mean low low-tide level) reached maximum sand volumes by the end of summer and minimum volumes in the late winter or early spring. In contrast, the subtidal beach (below MLLT) exhibited an opposite trend, with maximum and minimum volumes in late winter and summer, respectively. A similar seasonal pattern to Ensenada was observed at La Misión Beach (located 30 km north from Ensenada), but in contrast to Ensenada, significant alongshore seasonal variations were observed (Ruiz de Alegría-Arzaburu et al., 2022). Alongshore morphological variations at La Misión have been primarily associated with the presence of rip currents (Ruiz de Alegría-Arzaburu et al., 2022). In this research we conclude that alongshore undertow intensity variations caused by wave directionality differences are an additional factor inducing morphological changes along La Misión (Kono-Martínez et al., 2023).

La playa actúa como una interfaz dinámica entre la tierra y el mar, ofreciendo un espacio único para gran variedad de actividades recreativas, turísticas, náuticas y pesqueras. Generalmente, la playa está definida como una acumulación de sedimentos (arena, grava y guijarros) que está siendo constantemente moldeada por las fuerzas del oleaje y marea. La interacción entre la forma de la playa y la hidrodinámica generada por el viento, marea, oleaje y corrientes se conoce como morfodinámica de la playa. La naturaleza dinámica de la playa no solo sustenta biodiversidad (Defeo et al., 2009; Amaral et al., 2016), sino que también desempeña un papel fundamental en la conservación de los ecosistemas costeros, ya que sus características morfológicas influyen en la resiliencia costera.

La playa se divide en tres zonas según los procesos del oleaje: la zona mar adentro (*offshore*), la zona de rompiente (*surf zone*) y la zona de lavado (*swash zone*) (Figura 1.1), y cada sección presenta características morfológicas únicas. Las barras de arena formadas por la compleja interacción entre olas y corrientes se identifican como elevaciones en el perfil de playa (Figura 1.1), y estos rasgos son típicamente indicativos del estado morfodinámico de la playa. Las barras de arena pueden localizarse en la sección submareal entre la zona de rompientes y la zona de lavado, o bien en la playa intermareal influenciado por el ciclo de mareas (Holman & Bowen, 1982; van Maanen et al., 2008; Ruessink et al., 2009; Aagaard et al., 2013; van de Lageweg et al., 2013a; Splinter et al., 2018; Phillips et al., 2019). Las bermas, típicamente ubicadas justo por encima del alcance de la marea, son rasgos morfológicos indicativos de construcción, transversalmente presentan una sección triangular cercano a la cresta y cuasi plana en la parte posterior que se extiende hacia el mar desde la base de la duna, a menudo posterior a la cresta hay un cambio distintivo en la pendiente (King, 1959; Hine, 1979; Masselink & Hughes, 2003).

Las barras de arena constituyen la primera línea de defensa contra la erosión costera y la inundación, y se consideran importantes reservorios de arena para el balance sedimentario de la zona cercana a la costa; por lo tanto, contribuyen a la resiliencia costera (Senechal et al., 2015). Las barras de arena migran a lo largo de la playa en relación con la energía del oleaje entrante, y a menudo están asociadas con la remoción o reconstrucción de la berma. Cuando la energía del oleaje es baja y persistente durante varias semanas o meses, las barras de arena tienden a migrar hacia tierra, lo que posteriormente permite la reconstrucción de la berma. En cambio, condiciones de alta energía inducen la erosión de la berma y la formación y migración hacia mar adentro de la barra de arena. Así, la energía de las olas determina la distribución del sedimento a lo largo de la playa, lo cual suele analizarse a través del tamaño y la ubicación de las barras (Ruessink et al., 2009; Vidal-Ruiz & Ruiz de Alegría-Arzaburu, 2019, 2020).

Las playas de California y Baja California presentan una marcada estacionalidad, en respuesta a las características del oleaje incidente. Shepard (1950) fue uno de los primeros investigadores en describir la estacionalidad de las playas arenosas. Él mostró que el oleaje de invierno de mayor energía erosiona la parte subaérea de la playa, reduciendo el ancho de la berma y formando una barra de arena mar adentro, mientras que el oleaje de verano de menor energía induce acreción en la playa, lo que conlleva la erosión de la barra de arena y la formación de una berma más ancha. El ancho de la berma varia con el rango de marea, siendo más angosta durante las mareas de sicigia y más ancha durante las mareas muertas. Más reciente, Ruiz de Alegría-Arzaburu et al. (2017) indicaron un comportamiento estacional similar en la Playa de Ensenada, en Baja California, y demostraron que la playa subaérea (por encima del nivel medio de bajamar media inferior, MLLT por sus siglas en inglés) alcanzaba volúmenes máximos de arena al final del verano y mínimos a finales del invierno o inicios de primavera. En contraste, la playa submareal (por debajo del MLLT) mostraba una tendencia opuesta, con volúmenes máximos y mínimos a finales del invierno y en verano, respectivamente. El patrón estacional del sistema barra-berma similar al de Ensenada fue observado en Playa La Misión (ubicada 30 km al norte de Ensenada), pero a diferencia de Ensenada, se observaron variaciones estacionales significativas a lo largo de la costa (Ruiz de Alegría-Arzaburu et al., 2022). Las variaciones morfológicas a lo largo de la playa en La Misión han sido asociadas principalmente a la presencia de flujos de retorno (Ruiz de Alegría-Arzaburu et al., 2022). En esta investigación, concluimos que las variaciones en la intensidad de la corriente de retorno a lo largo de la costa, inducidas por diferencias en la direccionalidad del oleaje, son un factor adicional que provoca cambios morfológicos en La Misión (Kono-Martínez et al., 2023).

1.2. Scientific context on sandbar and berm dynamics

The first efforts in the study of sandbar morphodynamics primarily relied on observations, but these were scarce due to their complexity and cost for gathering high-resolution spatio-temporal data (Di Leonardo & Ruggiero, 2015). The addition of video-monitoring techniques allowed the description of sandbar and berm dynamics at different sites and in the short and medium term (Ruessink & Kroon, 1994; Brander, 1999; Ranasinghe et al., 2004; Sedrati & Anthony, 2007; Masselink et al., 2008; Ruessink et al., 2009; Coco et al., 2014; Phillips et al., 2019; Vidal-Ruiz & Ruiz de Alegría-Arzaburu, 2019, 2020).

Since sandbars contain significant volumes of sand that contribute to beach recovery during the summer, cross-shore and alongshore sandbar dynamics have been a relevant research topic over the past several decades. Offshore sandbar migrations are typically observed during energetic wave events (Holman & Sallenger, 1993; van Maanen et al., 2008; Ruessink et al., 2009; Vidal-Ruiz & Ruiz de Alegría-Arzaburu, 2019, 2020), often leading to intense offshore-directed flows such as undertow (Mariño-Tapia et al., 2007) and the development of strong rip currents (Short, 1999). Conversely, the physical processes contributing to onshore sandbar migration are less well understood. It is generally accepted that onshore sandbar movement occurs during low wave energy conditions, triggered by positively skewed wave orbital velocities that promote the welding of the sandbar to the shoreline (Hoefel & Elgar, 2003; Hsu et al., 2006; Ruessink et al., 2007; van Maanen et al., 2008; van de Lageweg et al., 2013a; Fernández-Mora et al., 2015; Cheng et al., 2016), ultimately contributing to berm rebuilding driven by swash zone processes (Austin & Masselink, 2006; Phillips et al., 2019).

The crest of the berm is located at the upper runup limit; thus, its formation and vertical growth are predominantly controlled by the spring-neap tidal cycle (Shepard, 1950; Hine, 1979; Jensen et al., 2009; Russell et al., 2009). The first research describing the formation mechanisms of the berm were undertaken by Hine (1979), and concluded that the conditions for berm formation were the following: (1) the highest high tide during neap tides; (2) the migration and welding of the subtidal sandbar to shoreline; and (3) the presence of an intertidal sandbar with a crest at the same level as the highest high tide during spring tides. For the berm reconstruction, the supratidal beach may show progradation (shoreward growth of the shoreline) or aggradation (vertical growth of the crest) (Dubois, 1988), and these processes will depend on the swash incidence (Baldock et al., 2008). Both processes can also be combined and occur simultaneously (Weir et al., 2006; Phillips et al., 2019). Several studies have shown that once the berm is formed, swash overtopping allows berm growth in coincidence with the growth of the shoreline (Austin & Masselink, 2006; Weir et al., 2006).

Despite the existence of multiple datasets that study the morphological behavior of sandbars and berms, there is still a remaining need to further understand how sand exchanges occur between these features, and how the processes vary at different time scales. For this purpose, it is essential to gather measurements in the short-term (days to weeks) and long-term (years to decades), and analyze sediment exchange variations along the beach. Sediment exchanges between sandbars and berms are complex processes influenced by the morphodynamic beach state. Hence, better characterizing spatial and temporal variations of these processes is essential to improve predictions of the coastal change in the future and contribute to adequate management strategies that allow the conservation of the coastal zone.

Beaches may present alongshore morphology variations (Figure 1.2.1) associated with swash oscillations associated with wave runup and nearshore current variations, which play a crucial role in determining the distribution of sediment and the morphological evolution of the beach over the time (Aagaard et al., 2004; Cooper & Pilkey, 2004; Dodet et al., 2019). These variations can lead to the formation of features such as sandbars (Kono-Martínez et al., 2023), cusps, and rip channels, significantly impacting coastal stability and resilience (Brander, 1999; van Gaalen et al., 2011; Gallop et al., 2011; Senechal et al., 2015).

Semi-enclosed beaches, located between headlands, natural capes or promontories, present unique alongshore hydrodynamic variations. The interaction between waves and currents within these embayed sites often results in complex flow patterns leading to significant spatial variability in sediment transport and beach morphology (Loureiro et al., 2012; Robinet et al., 2020). Alongshore variations in wave energy, influenced by factors such as the orientation of the beach (Bryan et al., 2009; Ruiz de Alegría-Arzaburu et al., 2010; van de Lageweg et al., 2013), the shape of the embayment, and the location and geometry of the headlands, generate nearshore circulation patterns that induce uneven erosion and deposition along the shoreline, often affecting the stability of the beach (Robinet et al., 2020). In addition, the complex flow patterns in embayed beaches often results in the formation of rip currents and small-scale eddies. Rip currents, strong narrow offshore flows, can interact with alongshore currents and lead to the redistribution of sediment, creating zones of erosion and deposition along the beach too (Brander, 1999). Similarly, undertow currents, offshore flows beneath incoming waves, contribute to the offshore transport of sediment (Mariño-Tapia et al., 2007), and alongshore variations can occur associated with the embayment geometry (Robinet et al., 2020). In addition, in meso- and macro-tidal environments, tides can also play a significant role in contributing to alongshore cross-shore flow variations (Bruneau et al., 2014; Castelle et al., 2020). Overall, understanding the interaction between the nearshore morphology and alongshore flows is complex, and this is usually carried out using idealized numerical models due to the limitations to collect the required concurrent morphological and hydrodynamic data.

Los primeros esfuerzos en estudiar la morfodinámica de las barras submareales se basaron principalmente en observaciones, pero estas eran escasas debido a la complejidad y el costo de obtener datos espacio-temporales de alta resolución (Di Leonardo & Ruggiero, 2015). La incorporación de técnicas como video monitoreo permitió describir la dinámica de las barras submareales y la berma en diferentes sitios y en el corto y mediano plazo (Ruessink & Kroon, 1994; Brander, 1999; Ranasinghe et al., 2004; Sedrati & Anthony, 2007; Masselink et al., 2008; Ruessink et al., 2009; Coco et al., 2014; Phillips et al., 2019; Vidal-Ruiz & Ruiz de Alegría-Arzaburu, 2019, 2020).

Dado que las barras submareales contienen volúmenes importantes de arena que contribuyen a la recuperación de la playa en verano, su dinámica transversal y a lo largo de la costa ha sido un tema de investigación relevante en las últimas décadas. Las migraciones hacia mar afuera de las barras submareales se observan durante eventos de oleaje energético (Holman & Sallenger, 1993; van Maanen et al., 2008; Ruessink et al., 2009; Vidal-Ruiz & Ruiz de Alegría-Arzaburu, 2019, 2020), debido a flujos intensos hacia mar afuera como la resaca (Mariño-Tapia et al., 2007), pero también en presencia de intensas corrientes de retorno (Short, 1999). Por el contrario, los procesos físicos que contribuyen a las migraciones hacia tierra de las barras submareales son menos comprendidos. Se acepta generalmente que estos movimientos ocurren durante condiciones de baja energía del oleaje, inducidos por velocidades orbitales de oleaje con asimetría positiva, que provocan la fusión de la barra submareal con la línea de costa (Hoefel & Elgar, 2003; Hsu et al., 2006; Ruessink et al., 2007; van Maanen et al., 2008; van de Lageweg et al., 2013a; Fernández-Mora et al., 2015; Cheng et al., 2016), lo cual finalmente contribuye a la reconstrucción de la berma, impulsada por procesos en la zona de lavado (Austin & Masselink, 2006; Phillips et al., 2019).

La cresta de la berma se encuentra en el límite superior del alcance de las olas (runup); por lo tanto, su formación y crecimiento vertical están controlados predominantemente por el ciclo de marea viva-muerta (Shepard, 1950; Hine, 1979; Jensen et al., 2009; Russell et al., 2009). Las primeras investigaciones que describieron los mecanismos de formación de la berma fueron llevadas a cabo por Hine (1979), quien concluyó que las condiciones para su formación eran las siguientes: (1) el cambio de la marea de baja a alta durante mareas muertas/vivas; (2) la migración y fusión de la barra submareal con la línea de costa; y (3) la presencia de una barra intermareal con cresta al mismo nivel que la marea durante mareas muertas/vivas. Para la reconstrucción de la berma, la playa subaérea puede mostrar progradación (crecimiento hacia tierra de la línea de costa) o agradación (crecimiento vertical de la cresta) (Dubois, 1988), estos procesos pueden combinarse y ocurrir simultáneamente (Weir et al., 2006; Phillips et al., 2019), sin embargo, ambos dependerán de la incidencia del swash (Baldock et al., 2008). Diversos estudios han mostrado que, una vez formada la berma, el sobreexcedente por swash permite su crecimiento en coincidencia con la acreción de la línea de costa (Austin & Masselink, 2006; Weir et al., 2006).

A pesar de la existencia de múltiples conjuntos de datos que estudian el comportamiento morfológico de las barras submareales y bermas, aún existe la necesidad de entender mejor cómo ocurre el intercambio de sedimento entre estas formas morfológicas, y cómo varían a distintas escalas temporales. Para ello, es esencial recopilar mediciones en el corto plazo (días a semanas) y largo plazo (años a décadas), y analizar las variaciones en el intercambio de sedimentos a lo largo de la playa. Los intercambios de sedimento entre barras submareales y bermas son procesos complejos, influenciados por el estado morfodinámico de la playa. Por lo tanto, caracterizar mejor las variaciones espaciales y temporales de estos procesos es esencial para mejorar las predicciones del cambio costero en el futuro y contribuir a estrategias de manejo adecuadas que permitan conservar la zona costera.

Las playas pueden presentar variaciones morfológicas a lo largo de la costa (Figura 1.2.1), asociadas con oscilaciones del *swash* relacionadas con el alcance del oleaje y variaciones de corrientes en la zona cercana a la costa, las cuales juegan un papel crucial en la distribución del sedimento y la evolución morfológica de la playa a escalas estacionales e interanuales (Aagaard et al., 2004; Cooper & Pilkey, 2004; Dodet et al., 2019). Estas variaciones pueden dar lugar a la formación de elementos como barras submareales (Kono-Martínez et al., 2023), cúspides y canales de retorno, impactando significativamente la estabilidad y resiliencia costera (Brander, 1999; van Gaalen et al., 2011; Gallop et al., 2011; Senechal et al., 2015).

Las playas semi-encajada, localizadas entre cabos, promontorios o acantilados naturales, presentan variaciones hidrodinámicas a lo largo de la costa que son únicas. La interacción entre oleaje y corrientes dentro de estos sitios encajados a menudo da lugar a patrones de flujo complejos que generan una variabilidad espacial significativa en el transporte de sedimentos y la morfología de la playa (Loureiro et al., 2012; Robinet et al., 2020). Las variaciones a lo largo de la costa en la energía del oleaje, influenciadas por factores como la orientación de la playa (Bryan et al., 2009; Ruiz de Alegría-Arzaburu et al., 2010; van de Lageweg et al., 2013), la forma de la ensenada y la ubicación y geometría de los promontorios, generan patrones de circulación costera que inducen erosión y acreción desigual a lo largo de la línea de costa, afectando a menudo la estabilidad de la playa (Robinet et al., 2020). Además, los patrones de flujo complejos en playas encajadas frecuentemente generan corrientes de retorno y remolinos de pequeña escala. Las corrientes de retorno, flujos fuertes y angostos que se dirigen mar adentro, pueden interactuar con las corrientes a lo largo de la costa y generar redistribuciones de sedimento, creando zonas de erosión y acreción a lo largo de la playa (Brander, 1999). De forma similar, los flujos de retorno por resaca, flujos mar adentro que ocurren bajo las olas entrantes, contribuyen al transporte de sedimento hacia mar adentro (Mariño-Tapia et al., 2007), y pueden presentar variaciones a lo largo de la costa dependiendo de la geometría de la bahía (Robinet et al., 2020). Además, en ambientes meso y macro mareales, las mareas juegan un papel importante en contribuir a las variaciones de flujo tanto a lo largo como transversal la costa (Bruneau et al., 2014; Castelle et al., 2020). En general, entender la interacción entre la morfología de la zona cercana a la costa y los flujos a lo largo de la misma es complejo, y usualmente se lleva a cabo mediante modelos numéricos idealizados debido a las limitaciones para obtener los datos morfológicos e hidrodinámicos concurrentes necesarios.

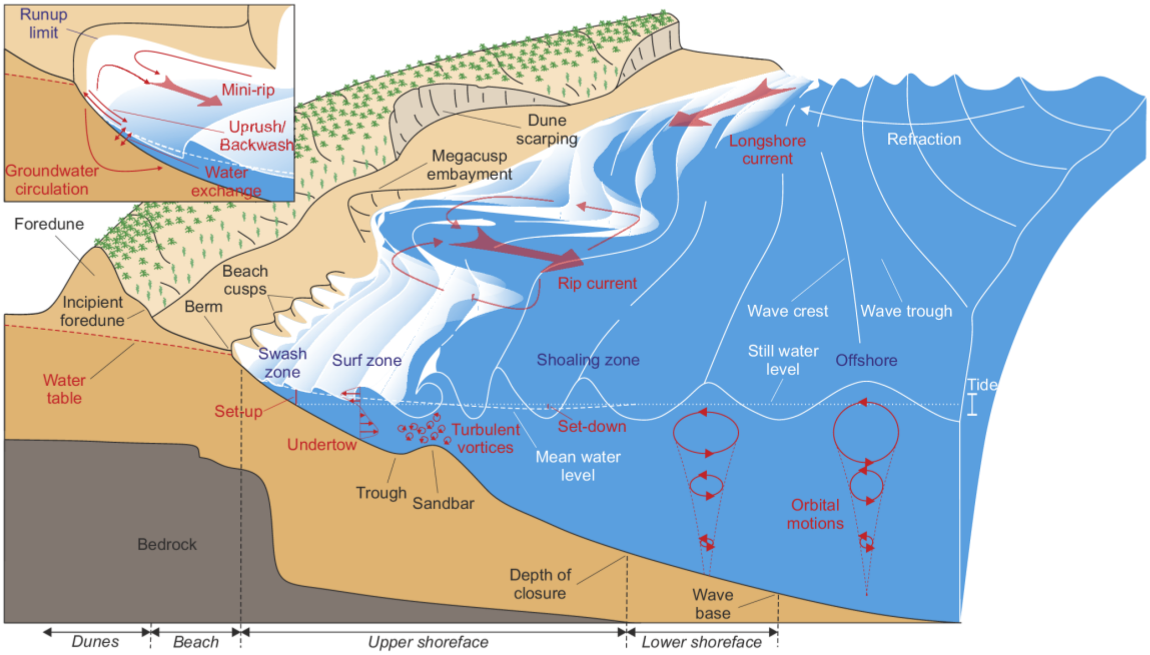

Figure 1.2.1 Schematic 3D beach profile denoting the main alongshore variations processes in sandy beaches (Castelle & Masselink, 2022).

Figura 1.2.1 Esquema de perfil de playa en 3D. denotando los principales procesos longitudinales para playas de arena (Castelle & Masselink, 2022).

1.3. Research objectives and thesis outline / Objetivos de investigación y esquema de tesis

The main purpose of this study is to gain a better understanding of sediment exchanges between the sandbar and the berm over seasonal to multi-annual timescales, focused on processes inducing alongshore variability, and based on field measurements and numerical modeling. The specific research objectives are the following:

1. To determine the processes involved in the formation, removal, and reconstruction of sandbars and berms, and their sediment exchanges on a highly dynamic beach, through the analysis of morphological and hydrodynamic data gathered from field surveys conducted monthly over a 5-year period.
2. To characterize nearshore circulation patterns for different morphodynamics beach states defined from the long-term morphological dataset, using a validated process-based hydrodynamic model, to contribute to the understanding of the processes involved in the alongshore variations of the sandbar-berm cycle.

The thesis is structured as follows: Chapter 2 describes the field site and presents the general methodology used to identify morphological features and describe sandbar-berm cycles. Chapter 3 examines the physical processes influencing spatiotemporal variations in sandbar-berm cycles in relation to hydrodynamic forcings. Chapter 4 determines the spatial variations in nearshore circulation patterns for different morphodynamic beach states, and their contributions to the sandbar-berm cycle. Chapter 5 summarizes the main findings of this research and discusses future perspectives.

El objetivo principal de este estudio es obtener una mejor comprensión de los intercambios de sedimento entre la barra submareal y la berma en escalas temporales que van desde lo estacional hasta lo multianual, con un enfoque en los procesos que inducen variabilidad a lo largo de la costa, y basado en mediciones de campo y modelación numérica. Los objetivos específicos de la investigación son los siguientes:

1. Determinar los procesos involucrados en la formación, remoción y reconstrucción de barras submareales y bermas, así como sus intercambios de sedimento en una playa altamente dinámica, mediante el análisis de datos morfológicos e hidrodinámicos recolectados mensualmente durante un período de 5 años.

2. Caracterizar los patrones de circulación en la zona cercana a la costa para diferentes estados morfodinámicos de la playa, definidos a partir del conjunto de datos morfológicos de largo plazo, utilizando un modelo hidrodinámico de base física validado, para contribuir a la comprensión de los procesos involucrados en las variaciones a lo largo de la costa del ciclo

barral–berma.

La tesis está estructurada de la siguiente manera: el Capítulo 2 describe el sitio de estudio y presenta la metodología general utilizada para identificar los rasgos morfológicos y descripción de los ciclos barra –berma. El Capítulo 3 examina los procesos físicos que influyen en las variaciones espacio-temporales de los ciclos barra–berma en relación con los forzamientos hidrodinámicos. El Capítulo 4 examina las variaciones espaciales en los patrones de circulación costera para diferentes estados morfodinámicos de la playa y sus contribuciones al ciclo barra–berma. El Capítulo 5 resume los principales hallazgos de esta investigación y discute perspectivas futuras.

References

Aagaard, T., Davidson-Arnott, R., Greenwood, B., & Nielsen, J. (2004). Sediment supply from shoreface to dunes: linking sediment transport measurements and long-term morphological evolution. *Geomorphology*, *60*(1), 205–224. https://doi.org/https://doi.org/10.1016/j.geomorph.2003.08.002

Aagaard, T., Greenwood, B., & Hughes, M. (2013). Sediment transport on dissipative, intermediate and reflective beaches. *Earth-Science Reviews*, *124*, 32–50. https://doi.org/https://doi.org/10.1016/j.earscirev.2013.05.002

Amaral, A. C. Z., Corte, G. N., Filho, J. S. R., Denadai, M. R., Colling, L. A., Borzone, C., Veloso, V., Omena, E. P., Zalmon, I. R., Rocha-Barreira, C. de A., Souza, J. R. B. de, Rosa, L. C. da, & Almeida, T. C. M. de. (2016). Brazilian sandy beaches: characteristics, ecosystem services, impacts, knowledge and priorities. *Brazilian Journal of Oceanography*, *64*.

Austin, M. J., & Masselink, G. (2006). Observations of morphological change and sediment transport on a steep gravel beach. *Marine Geology*, *229*(1), 59–77. https://doi.org/https://doi.org/10.1016/j.margeo.2006.02.003

Baldock, T. E., Weir, F., & Hughes, M. G. (2008). Morphodynamic evolution of a coastal lagoon entrance during swash overwash. *Geomorphology*, *95*(3), 398–411. https://doi.org/https://doi.org/10.1016/j.geomorph.2007.07.001

Blossier, B., Bryan, K. R., Daly, C. J., & Winter, C. (2016). Nearshore sandbar rotation at single-barred embayed beaches. *Journal of Geophysical Research: Oceans*, *121*(4), 2286–2313. https://doi.org/https://doi.org/10.1002/2015JC011031

Brander, R. W. (1999). Field observations on the morphodynamic evolution of a low-energy rip current system. *Marine Geology*, *157*(3), 199–217. https://doi.org/https://doi.org/10.1016/S0025-3227(98)00152-2

Bruneau, N., Bertin, X., Castelle, B., & Bonneton, P. (2014). Tide-induced flow signature in rip currents on a meso-macrotidal beach. *Ocean Modelling*, *74*, 53–59. https://doi.org/https://doi.org/10.1016/j.ocemod.2013.12.002

Bryan, K., Gallop, S., Lageweg, W. I., & Coco, G. (2009). *Observations of rip channels, sandbar-shoreline coupling and beach rotation at Tairua Beach, New Zealand*. https://doi.org/10.13140/RG.2.1.3687.6241

Castelle, B., Scott, T., Brander, R., Mccarroll, R., Tellier, E., de Korte, E., Tackuy, L., Robinet, A., Bruno, S., & Salmi, L.-R. (2020). Wave and Tide

Controls on Rip Current Activity and Drowning Incidents in Southwest France. *Journal of Coastal Research*, *95*, 769. https://doi.org/10.2112/SI95-150.1

Cheng, J., Wang, P., & Smith, E. R. (2016). Hydrodynamic Conditions Associated with an Onshore Migrating and Stable Sandbar. *Journal of Coastal Research*, *32*(1), 153 – 163. https://doi.org/10.2112/JCOASTRES-D-14-00174.1

Coco, G., Senechal, N., Rejas, A., Bryan, K. R., Capo, S., Parisot, J. P., Brown, J. A., & MacMahan, J. H. M. (2014). Beach response to a sequence of extreme storms. *Geomorphology*, *204*, 493–501. https://doi.org/https://doi.org/10.1016/j.geomorph.2013.08.028

Cooper, J. A. G., & Pilkey, O. H. (2004). Sea-level rise and shoreline retreat: time to abandon the Bruun Rule. *Global and Planetary Change*, *43*(3), 157–171. https://doi.org/https://doi.org/10.1016/j.gloplacha.2004.07.001

Defeo, O., McLachlan, A., Schoeman, D. S., Schlacher, T. A., Dugan, J., Jones, A., Lastra, M., & Scapini, F. (2009). Threats to sandy beach ecosystems: A review. *Estuarine, Coastal and Shelf Science*, *81*(1), 1–12. https://doi.org/https://doi.org/10.1016/j.ecss.2008.09.022

Di Leonardo, D., & Ruggiero, P. (2015). Regional scale sandbar variability: Observations from the U.S. Pacific Northwest. *Continental Shelf Research*, *95*, 74–88. https://doi.org/https://doi.org/10.1016/j.csr.2014.12.012

Dodet, G., Bertin, X., Bouchette, F., Gravelle, M., Testut, L., & Wöppelmann, G. (2019). Characterization of Sea-level Variations Along the Metropolitan Coasts of France: Waves, Tides, Storm Surges and Long-term Changes. *Journal of Coastal Research*, *88*(sp1), 10–24. https://doi.org/10.2112/SI88-003.1

Dubois, R. N. (1988). Seasonal changes in beach topography and beach volume in Delaware. *Marine Geology*, *81*(1), 79–96. https://doi.org/https://doi.org/10.1016/0025-3227(88)90019-9

Fernández-Mora, A., Calvete, D., Falqués, A., & de Swart, H. E. (2015). Onshore sandbar migration in the surf zone: New insights into the wave-induced sediment transport mechanisms. *Geophysical Research Letters*, *42*(8), 2869–2877. https://doi.org/https://doi.org/10.1002/2014GL063004

Gallop, S. L., Bosserelle, C., Pattiaratchi, C. B., & Eliot, I. G. (2011). Rock topography causes spatial variation in the wave, current and beach response to sea breeze activity. *Marine Geology*, *290*, 29–40. https://api.semanticscholar.org/CorpusID:129305667

Hine, A. C. (1979). Mechanisms of berm development and resulting beach growth along a barrier spit complex. *Sedimentology*, *26*(3), 333–351. https://doi.org/https://doi.org/10.1111/j.1365-3091.1979.tb00913.x

Hoefel, F., & Elgar, S. (2003). Wave-Induced Sediment Transport and Sandbar Migration. *Science*, *299*(5614), 1885–1887. https://doi.org/10.1126/science.1081448

Holman, R. A., & Bowen, A. J. (1982). Bars, bumps, and holes: Models for the generation of complex beach topography. *Journal of Geophysical Research: Oceans*, *87*(C1), 457–468. https://doi.org/https://doi.org/10.1029/JC087iC01p00457

Holman, R. A., & Sallenger, A. H. (1993). Sand Bar Generation: A Discussion of the Duck Experiment Series. *Journal of Coastal Research*, 76–92. http://www.jstor.org/stable/25735724

Hsu, T.-W., Tseng, I.-F., & Lee, C.-P. (2006). A New Shape Function for Bar-Type Beach Profiles. *Journal of Coastal Research*, *22*(3 (223)), 728–736. https://doi.org/10.2112/04-0340.1

Jensen, S. G., Aagaard, T., Baldock, T. E., Kroon, A., & Hughes, M. (2009). Berm formation and dynamics on a gently sloping beach; the effect of water level and swash overtopping. *Earth Surface Processes and Landforms*, *34*(11), 1533–1546. https://doi.org/https://doi.org/10.1002/esp.1845

King, C. A. M. (1959). Beaches and coasts: London. *Edward Arnold Ltd*, *403*.

Kono-Martínez, T., Ruiz de Alegría-Arzaburu, A., Mariño-Tapia, I., & Coco, G. (2023). Alongshore variability in berm and sandbar migration patterns on a highly dynamic beach. *Geomorphology*, *443*, 108935. https://doi.org/https://doi.org/10.1016/j.geomorph.2023.108935

Loureiro, C., Ferreira, Ó., & Cooper, J. A. G. (2012). Geologically constrained morphological variability and boundary effects on embayed beaches. *Marine Geology*, *329–331*, 1–15. https://doi.org/https://doi.org/10.1016/j.margeo.2012.09.010

Mariño-Tapia, I. J., Russell, P. E., O'Hare, T. J., Davidson, M. A., & Huntley, D. A. (2007). Cross-shore sediment transport on natural beaches and its relation to sandbar migration patterns: 1. Field observations and derivation of a transport parameterization. *Journal of Geophysical Research: Oceans*, *112*(C3). https://doi.org/https://doi.org/10.1029/2005JC002893

Masselink, G., Austin, M., Tinker, J., O'Hare, T., & Russell, P. (2008). Cross-shore sediment transport and morphological response on a macrotidal beach with intertidal bar morphology, Truc Vert, France. *Marine Geology*, *251*(3), 141–155. https://doi.org/https://doi.org/10.1016/j.margeo.2008.01.010

Masselink, G., & Hughes, M. (2003). *An Introduction to Coastal Processes and Geomorphology*. https://doi.org/10.4324/9780203783740

Phillips, M. S., Blenkinsopp, C. E., Splinter, K. D., Harley, M. D., & Turner, I. L. (2019). Modes of Berm and Beachface Recovery Following Storm Reset: Observations Using a Continuously Scanning Lidar. *Journal of Geophysical Research: Earth Surface*, *124*(3), 720–736. https://doi.org/https://doi.org/10.1029/2018JF004895

Ranasinghe, R., McLoughlin, R., Short, A., & Symonds, G. (2004). The Southern Oscillation Index, wave climate, and beach rotation. *Marine Geology*, *204*(3), 273–287. https://doi.org/https://doi.org/10.1016/S0025-3227(04)00002-7

Robinet, A., Castelle, B., Idier, D., Harley, M. D., & Splinter, K. D. (2020). Controls of local geology and cross-shore/longshore processes on embayed beach shoreline variability. *Marine Geology*, *422*, 106118. https://doi.org/https://doi.org/10.1016/j.margeo.2020.106118

Ruessink, B. G., & Kroon, A. (1994). The behaviour of a multiple bar system in the nearshore zone of Terschelling, the Netherlands: 1965–1993. *Marine Geology*, *121*(3), 187–197. https://doi.org/https://doi.org/10.1016/0025-3227(94)90030-2

Ruessink, B. G., Kuriyama, Y., Reniers, A. J. H. M., Roelvink, J. A., & Walstra, D. J. R. (2007). Modeling cross-shore sandbar behavior on the timescale of weeks. *Journal of Geophysical Research: Earth Surface*, *112*(F3). https://doi.org/https://doi.org/10.1029/2006JF000730

Ruessink, B. G., Pape, L., & Turner, I. L. (2009). Daily to interannual cross-shore sandbar migration: Observations from a multiple sandbar system. *Continental Shelf Research*, *29*(14), 1663–1677. https://doi.org/https://doi.org/10.1016/j.csr.2009.05.011

Ruiz de Alegría-Arzaburu, A., Gracia-Barrera, A. D., Kono-Martínez, T., & Coco, G. (2022). Subaerial and upper-shoreface morphodynamics of a highly-dynamic enclosed beach in NW Baja California. *Geomorphology*, *413*, 108336. https://doi.org/https://doi.org/10.1016/j.geomorph.2022.108336

Ruiz de Alegría-Arzaburu, A., Vidal-Ruiz, J. A., García-Nava, H., & Romero-

Arteaga, A. (2017). Seasonal morphodynamics of the subaerial and subtidal sections of an intermediate and mesotidal beach. *Geomorphology*, *295*, 383–392. https://doi.org/https://doi.org/10.1016/j.geomorph.2017.07.021

Russell, P. E., Masselink, G., Blenkinsopp, C., & Turner, I. L. (2009). A Comparison of Berm Accretion in the Swash Zone on Sand and Gravel Beaches at the Timescale of Individual Waves. *Journal of Coastal Research*, 1791–1795. http://www.jstor.org/stable/25738098

Sedrati, M., & Anthony, E. J. (2007). Storm-generated morphological change and longshore sand transport in the intertidal zone of a multi-barred macrotidal beach. *Marine Geology*, *244*(1), 209–229. https://doi.org/https://doi.org/10.1016/j.margeo.2007.07.002

Senechal, N., Coco, G., Castelle, B., & Marieu, V. (2015). Storm impact on the seasonal shoreline dynamics of a meso- to macrotidal open sandy beach (Biscarrosse, France). *Geomorphology*, *228*, 448–461. https://doi.org/https://doi.org/10.1016/j.geomorph.2014.09.025

Shepard, F. P. (1950). *Beach Cycles in Southern California*. University of California, San Diego, Scripps Institution of Oceanography. https://books.google.com.mx/books?id=YeYjHQAACAAJ

Short, A. D. (1999). *Handbook of beach and shoreface morphodynamics*. Great Britain: John Wiley; ISBN 0-471-96570-7.

Splinter, K. D., Harley, M. D., & Turner, I. L. (2018). Remote Sensing Is Changing Our View of the Coast: Insights from 40 Years of Monitoring at Narrabeen-Collaroy, Australia. *Remote Sensing*, *10*(11). https://doi.org/10.3390/rs10111744

van de Lageweg, W. I., Bryan, K. R., Coco, G., & Ruessink, B. G. (2013). Observations of shoreline–sandbar coupling on an embayed beach. *Marine Geology*, *344*, 101–114. https://doi.org/https://doi.org/10.1016/j.margeo.2013.07.018

van Gaalen, J. F., Kruse, S. E., Coco, G., Collins, L., & Doering, T. (2011). Observations of beach cusp evolution at Melbourne Beach, Florida, USA. *Geomorphology*, *129*(1), 131–140. https://doi.org/https://doi.org/10.1016/j.geomorph.2011.01.019

van Maanen, B., de Ruiter, P. J., Coco, G., Bryan, K. R., & Ruessink, B. G. (2008). Onshore sandbar migration at Tairua Beach (New Zealand): Numerical simulations and field measurements. *Marine Geology*, *253*(3), 99–106. https://doi.org/https://doi.org/10.1016/j.margeo.2008.05.007

Vidal-Ruiz, J. A., & Ruiz de Alegría-Arzaburu, A. (2019). Variability of sandbar morphometrics over three seasonal cycles on a single-barred beach. *Geomorphology*, *333*, 61–72. https://doi.org/10.1016/j.geomorph.2019.02.034

Vidal-Ruiz, J. A., & Ruiz de Alegría-Arzaburu, A. (2020). Modes of onshore sandbar migration at a single-barred and swell-dominated beach. *Marine Geology*, *426*(November 2019), 106222. https://doi.org/10.1016/j.margeo.2020.106222

Weir, F. M., Hughes, M. G., & Baldock, T. E. (2006). Beach face and berm morphodynamics fronting a coastal lagoon. *Geomorphology*, *82*(3), 331–346. https://doi.org/https://doi.org/10.1016/j.geomorph.2006.05.015

CHAPTER 2. Methodology

This chapter describes the research site and the general methods employed for the field data collection and analysis and numerical model implementation. The field measurements section includes descriptions of the morphological, sedimentological, and hydrodynamic data collected on the field. Special emphasis is placed on explaining detection methods for the subaerial and subtidal morphological features, such as berms and sandbars, from topographic and bathymetric profiles. The final section describes the set-up and implementation of the XBeach numerical model to understand nearshore circulation patterns under different morphological conditions.

Este capítulo describe el sitio de investigación y la metodología general empleada para la colecta de datos de campo, análisis de datos e implementación de modelación numérica. La sección de mediciones de campo incluye descripciones de los datos colectados en campo: morfológicos, sedimentológicos e hidrodinámicos. Con especial énfasis en explicar los métodos de detección de los rasgos morfológicos subaéreos y submareales como son las bermas y barras a partir de perfiles topográficos y batimétricos. La sección final describe la configuración e implementación del modelo numérico XBeach para entender los patrones de circulación cercanos a la costa bajo diferentes escenarios morfológicos.

2.1. Field site description

The field site is La Misión Beach, located within Descanso Bay on the northwestern coast of the Baja California peninsula in Mexico (Figure 2.1.1. A). The northern section of Descanso Bay is shallow, with typical depths of less than 60 m, whereas the southern section features a canyon with depths of up to 600 m (Figure 2.1.1. B). This region is part of the California Current system, where oceanic currents generally flow parallel to the coast towards the equator and intensify in spring due to increased wind stress and rotation generating upwelling along the coast (Durazo et al., 2024).

The beach is partially enclosed by a headland at its southern end and sparse rocks at its northern end (Figures 2.1.2). The upper beach of the northern section features cliffs, while the central zone is an urbanized area with small dunes. At the southernmost end, there is a highway carpark that connects a tidal inlet with a bridge (Figures 2.1.2). The beach is approximately 2.2 km long, composed of medium sand with a median grain size (D_{50}) of 0.242 mm. Tides are semi-diurnal, with an average range of 1.8 m, varying from 2.3 m during spring tides to 0.5 m during neap tides.

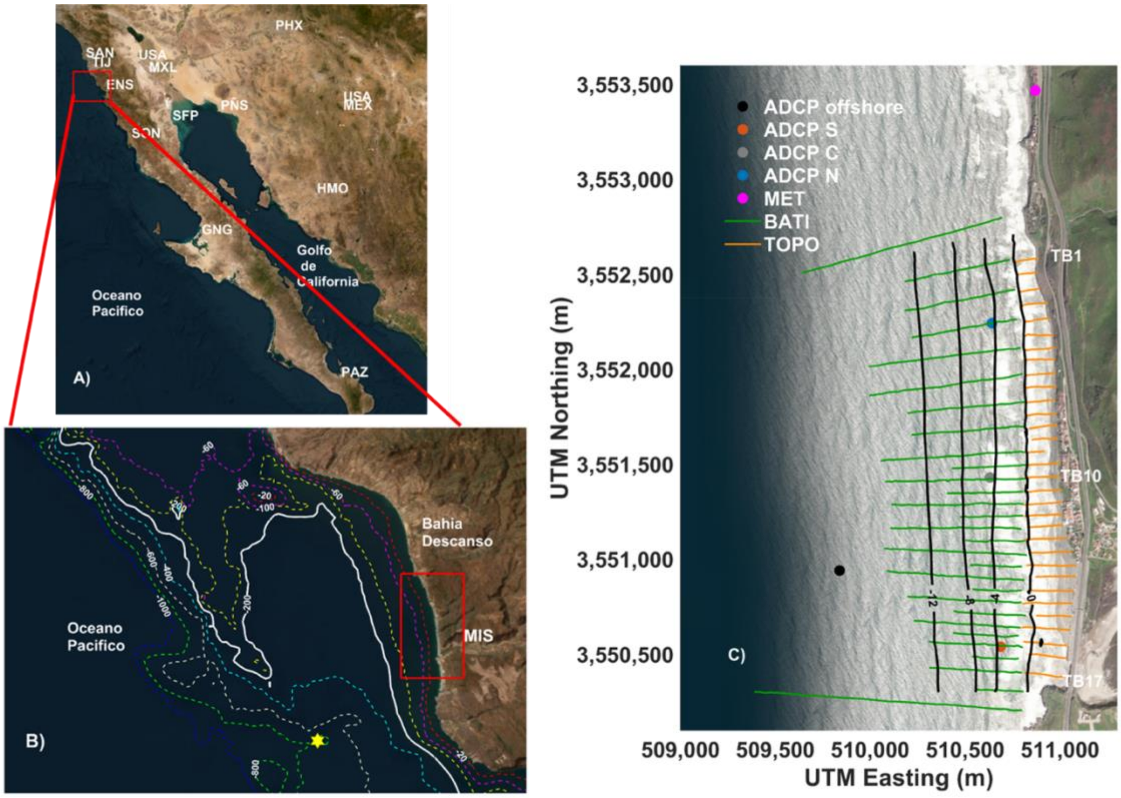

Figure 2.1.1 Study site location. (A) Northwestern Pacific coast in Mexico. (B) Zoom in into the northern Baja California Peninsula. The yellow dot represents the wave data from ERA5 reanalysis. (C) Zoom in into La Misión Beach, including topographic and bathymetric lines (orange and green), meteorological station location (MET) and ADCP mooring locations (colored dots).

Figura 2.1.1 Localización de la zona de estudio. (A) Noroeste de la costa del pacífico en México, (B) Acercamiento al norte de la península de Baja California. El punto amarillo representa los datos de oleaje de reanálisis de ERA5. (C) Acercamiento a playa La Misión, incluyendo líneas topográficas y batimétricas (naranjas y verdes), localización de la estación meteorológica (MET) y localización de las mediciones de ADCP (puntos de color).

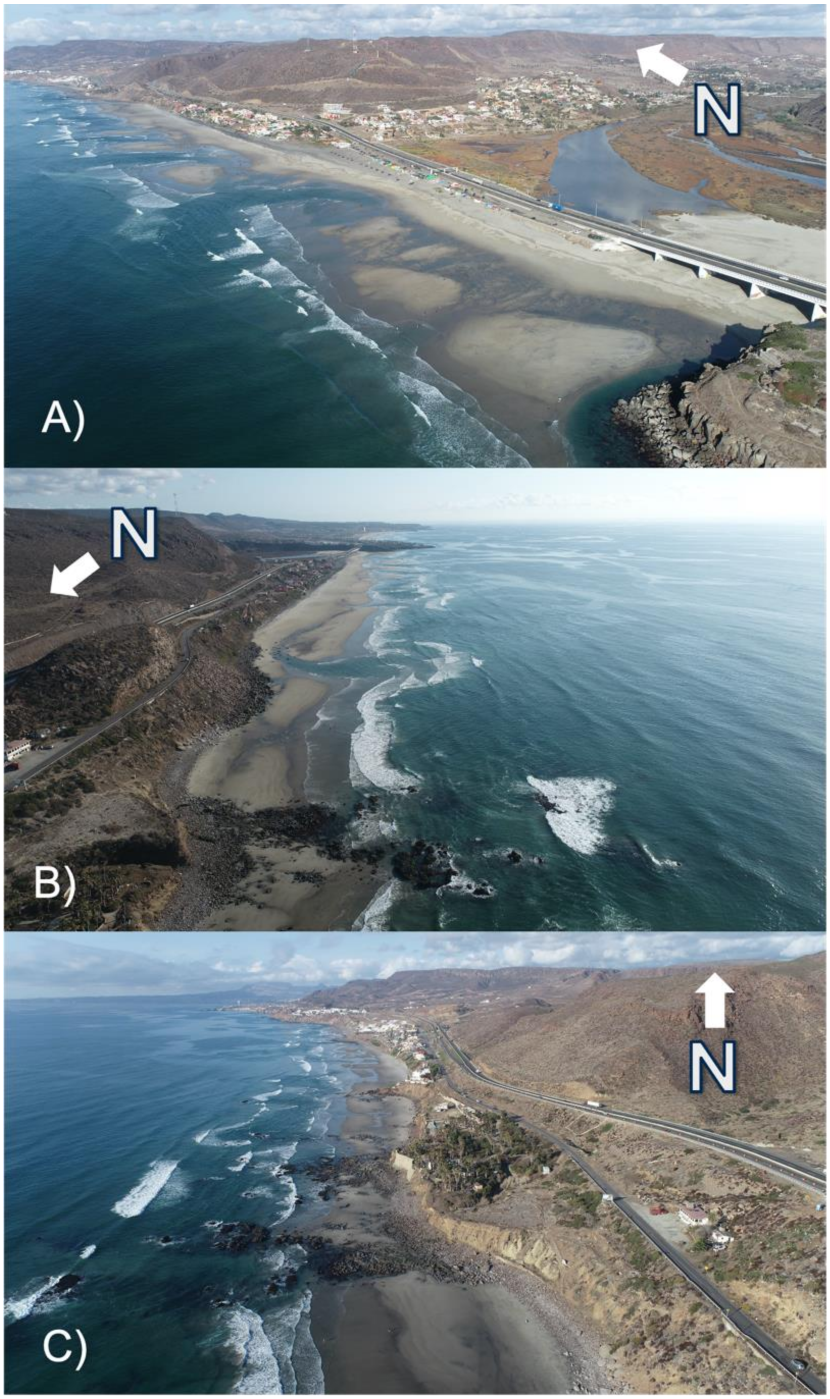

Figure 2.2.2 Aerial view of La Misión Beach: (A) facing northeast and (B) facing south. (C) facing north.

Figura 2.1.2. Vista aérea de playa La Misión. (A) mirando al noreste y (B) mirando al sur. (C) mirando al norte.

Incoming waves at La Misión Beach are primarily driven by swell–long period waves generated by distant weather systems–and exhibit notable seasonality in both height and direction. The annual average significant wave height, H_s, is 1.2 m with an associated spectral peak period of 11 s (Ruiz de Alegría-Arzaburu et al., 2022). High-energy waves, characterized by H_s exceeding 2 m and often surpassing 3 m, are prevalent during the winter and spring months from November to April (Figure 2.1.3. A). In contrast, low-energy waves with Hs less than 1 m dominate the summer and fall seasons, from May to October (Figure 2.1.3. B). During the winter, the preferential wave direction is shore-normal from the west, while in the summer it tends to shift to the west-southwest (Ruiz de Alegría-Arzaburu et al., 2022).

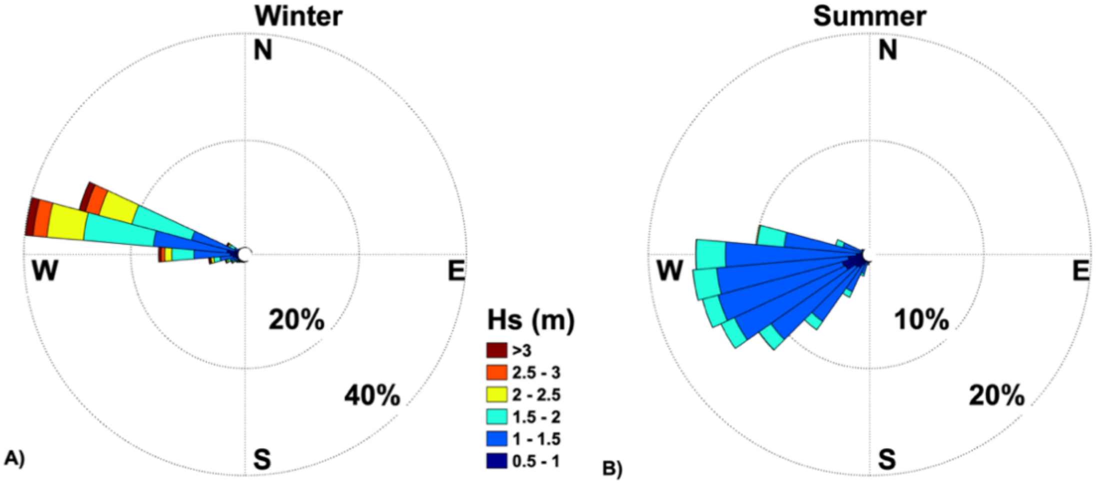

Figure 2.3.3 Wave roses for La Misión beach using ERA5 data (https://cds.climate.copernicus.eu/cdsapp#!/dataset/reanalysis-era5-single-levels?tab=overview) for: (A) winter; and (B) summer conditions.

Figura 2.1.3. Rosas de oleaje para playa La Misión utilizando datos de ERA5 https://cds.climate.copernicus.eu/cdsapp#!/dataset/reanalysis-era5-single-levels?tab=overview) para condiciones de: (A) invierno; y (B) verano.

Local meteorological data gathered between 2017 and 2020 indicate that the wind presents patterns dominated by breezes in the W to E and E to W directions (Figure 2.1.4A). Winds of highest intensity occur between December and February (Figure 2.1.4B), along with lowest air temperatures (<15°C) (Figure 2.1.4C), and coinciding with lowest relative humidity (60%) (Figure 2.1.4D) and highest precipitation (>0.002 mm) (Figure 2.1.4E). In spring, wind speed decrease, air temperature remains steady at around 15ºC, relative humidity reaches 70%, and precipitation decreases (<0.002 mm). In summer, winds are weak (1.7m/s), air temperature reaches monthly averages of 20^{o}C and the relative humidity increases up to 80%, and there is no precipitation. During fall, wind speeds increase (1.9m/s), air temperature remains above 15^{o}C, the relative humidity decreases to 70%, and precipitation increases towards the end of the season.

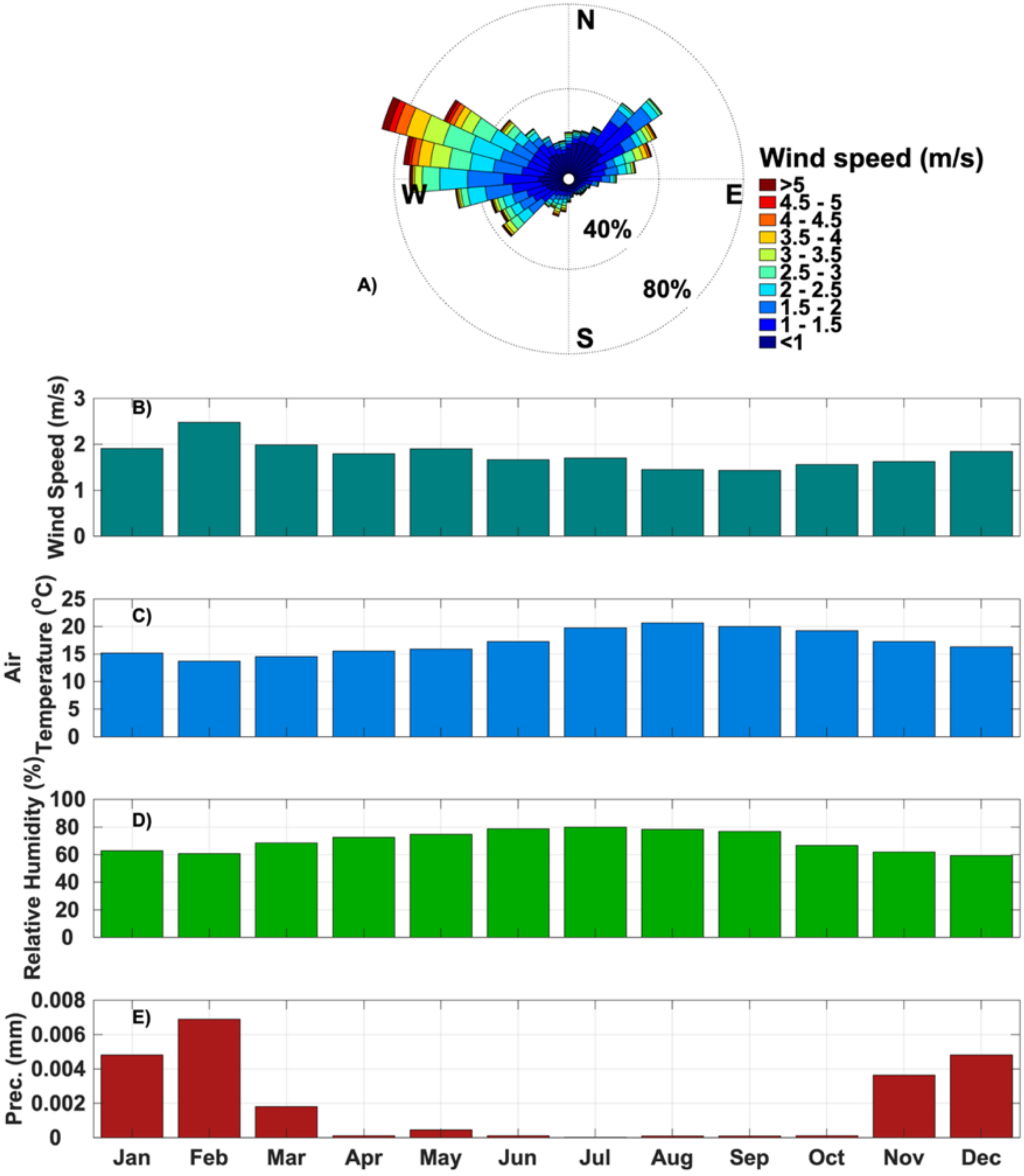

Figure 2.4.4 Climatology for local meteorological measurements near La Misión (La Fonda) from 2017 to 2020, Monthly-averaged: (A) Wind rose; (B) Wind speed; (C) Air temperature; (D) Relative humidity and (E) Precipitation.

Figura 2.1.4. Climatología de mediciones locales por la estación meteorológica cercana a La Misión (La Fonda) desde 2017 hasta 2020, promedios mensuales: (A) Rosa de los vientos; (B) Velocidad del viento; (C) Temperatura del aire; (D) Humedad relativa y (E) Precipitación.

Seasonal subaerial and subtidal beach variations are driven by fluctuations in the incoming wave energy. The most dissipative morphological conditions occur at the end of winter during high-energy waves. As spring and fall bring milder wave energy conditions, the beach transitions towards more reflective states (Figure 2.1.5). Subtidal sandbars form during winter and migrate onshore in spring until merging with the subaerial beach and contributing to the formation of a berm during summer-fall (Figure 2.1.5). The beach also exhibits significant alongshore morphological variations, primarily due to the presence of rip and feeder channels, which are believed to play a crucial role in facilitating the exchange of sediment between the inner subtidal and subaerial beach (Ruiz de Alegría-Arzaburu et al., 2022)

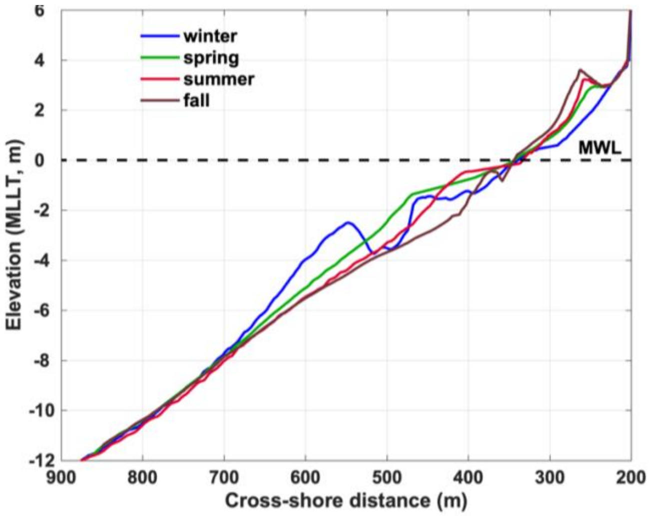

Figure 2.5.5. Typical seasonal topo-bathymetric beach profile change at La Misión Beach.
Figura 2.1.5. Cambio típico estacional del perfil topo-batimétrico de la playa en La Misión.

Alongshore morphological variations on the beach are influenced by the presence of rip currents and the inlet mouth (Figure 2.1.6). Rip currents create zones of erosion and deposition along the beach. They can carve out deeper channels in the nearshore zone, leading to localized erosion, while areas adjacent to these channels experience sediment accumulation and the formation of subtidal sandbars. It is believed that the Guadalupe stream inlet located in the southern beach end, interacts with the ocean-hydrodynamics occasionally, possibly modifying the sediment dynamics at specific times of the year and contributing to alongshore morphological variability (Figure 2.1.6). During periods of inlet opening, larger rip currents were observed, thus, the inlet could contribute to the formation of rip currents and enhance alongshore beach variations (Figure 2.1.6).

Figure 2.6.6. Aerial views of La Misión beach taken from UAV imagery. (a) Inlet opened on 2nd of March 2017. (b) Inlet closing in 21st March 2017. Note the input of sediments in (a) towards the beach, and the presence of wide rip currents in (b).

Figura 2.1.6. Vista aérea de playa La Misión fotografía obtenida de un VANT. (a) apertura de la boca del estuario durante 2 de marzo de 2017. (b) ensanchamiento del cauce en la boca del estuario durante el 21 de marzo 2017. Nótese la entrada de sedimentos en dirección hacia la playa en (a) y la presencia de amplias corrientes de retorno en (b).

2.2. Field measurements

2.2.1. Morphological data

Beach surveys were conducted on an almost monthly basis from November 2015 to October 2020. Each survey consisted of 32 topographic profiles spaced roughly 50 m along the shoreline, along with 7 bathymetric profiles spaced approximately 125 m in the northern half of the beach, and 20 bathymetric profiles spaced around 50 m apart in the southern half (Figure 2.1.1. C). All bathymetric profiles extended to depths of up to 12 m and covered a stretch of 2,200 m along the beach.

The topographies were measured using a RTK GPS (real-time kinematic Global Positioning System) with vertical accuracy within one-to-two centimeters (Figure 2.2.1.1.). Data were collected on foot, every second, down to the mean low low-tide level (MLLT; +36.474 m from ellipsoidal heights), utilizing a two-wheeled trolley operated by two people.

Figure. 2.2.1.1. Topographic data collection using RTK-GPS on foot using a two-wheeled pole.

Figura 2.2.1.1. Levantamiento de datos topográficos con RTK-GPS a pie utilizando un sistema de dos ruedas con una pértiga.

Nearshore bathymetric profiles were measured using a jetski equipped with a Sontek Hydrosurveyor ADCP with an integrated echo-sounder of 0.5 MHz. Depth measurements were radio-linked to a laptop installed in the back of the jetski inside a pelican case and synchronized with an RTK-GPS antenna to later calculate the relative depth (Figure 2.2.1.2.). A total of 17 complete topographic and bathymetric (TB) profiles were measured at each survey; the 17 profiles comprised co-linearly merged bathymetric data with topographic profiles (Figure 2.2.1.3).

Figure. 2.2.2.2 Equipment used for the collection of bathymetric data. Example of the Sontek M9 echo-sounder integrated on an ADCP (top left panel) and the equipment mounted onto the jetski (top right and bottom panels).

Figura 2.2.1.2. Equipo utilizado para el levantamiento de datos batimétricos. Ejemplo de eco-sonda Sontek M9 integrada sobre un ADCP (panel Izquierdo superior) y equipo montado sobre una moto acuática (panel superior derecho y panel inferior).

Figure. 2.2.3.3 Schematic diagram of the instruments used for the subaerial and subtidal morphological data collection at La Misión Beach.

Figura 2.2.1.3 Diagrama esquemático de los instrumentos utilizados para el levantamiento subaéreo y submareal morfológico en playa La Misión.

A linear interpolation was applied to the 17 TB profiles at 0.1 m in the cross-shore and 10 m in the alongshore direction to generate topo-bathymetric digital elevation models (DEMs), and to cover gaps due to limitations in data acquisition in the surf zone. DEMs capture the instantaneous morphological state of the beach. Therefore, by observing their temporal variations, we can deduce the temporal morphological evolution of the beach (see an example at Figure 2.3.1.). To achieve this, a 5-year average DEM was computed and then subtracted from each individual DEM (de-meaned). Subsequently, the differences in de-meaned DEMs over time were summed to describe the cumulative morphological changes of the beach.

2.2.2. Sediment characteristics

Sediment samples (100g of sand) were collected from six topographic profiles (T01, T06, T12, T18, T24 and T32) at the mean low-water mark (MLWM) every 3-4 months over a one-year period (2018-2019) to characterize seasonal grain size variations (Figure 2.2.2.1.). The samples were processed and sieved for grain size analysis (D_{50} and D_{90}) using the Folk & Ward (1957) method, which involves passing the sample through various gradually sized mesh sieves (Figure 2.2.2.1). The amount of material on each sieve was weighed to determine the percentage of the total mass, and D_{50} and D_{90} were calculated from the cumulative distribution curve (Blott & Pye, 2001).

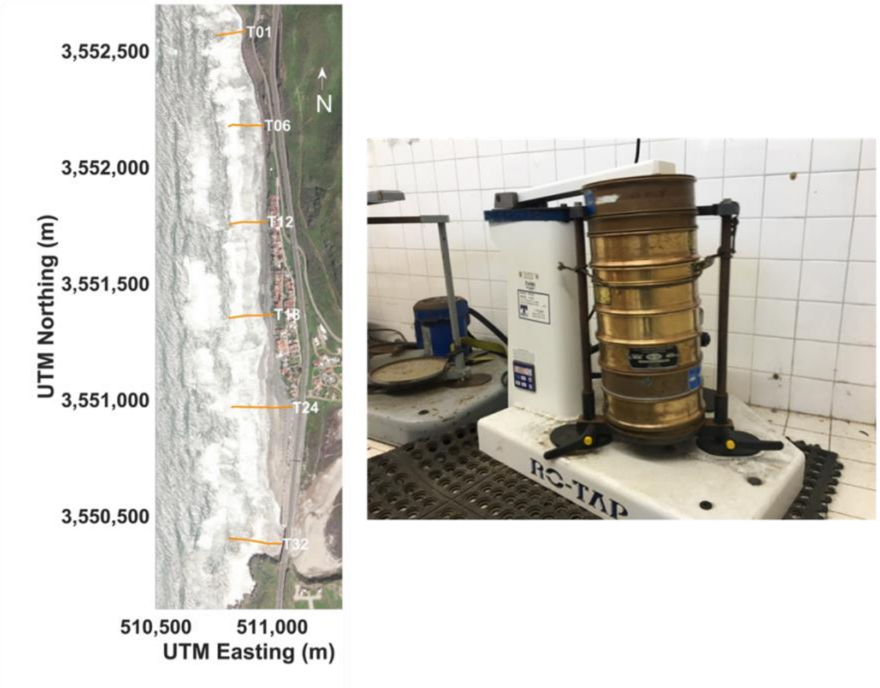

Figure 2.2.2.1. Location of beach profiles where sediment samples were collected (left panel). RX-29 RO-TAP sieve shaker used to carry out the sediment grain size analysis (right panel).

Figura 2.2.2.1. Localización de los perfiles de playa donde las muestras de sedimento fueron colectadas (panel Izquierdo). RX-29 RO-TAP tamizadora mecánica utilizada para llevar a cabo el análisis de tamaño de sedimento (panel derecho).

The average D_{50} for the 2018-2019 study period was 0.242 mm (Table I), and slight alongshore differences were observed between seasons. In winter and spring, D_{50} was slightly higher than summer and fall, and it was higher for the southern section of the beach than for the northern section.

Table I. Seasonal alongshore variations of the median grain diameter, D_{50}, at La Misión Beach from 2018-2019.

Tabla I. Variación estacional a lo largo de la playa del tamaño de grano del diámetro D_{50} en playa La Misión desde 2018-2019.

La Misión Beach D50 (mm)						
Season/Location	**T1**	**T6**	**T12**	**T18**	**T24**	**T32**
Winter	0.223	0.239	0.209	0.214	0.259	0.286
Spring	0.229	0.234	0.242	0.232	0.242	0.239
Summer	0.221	0.224	0.232	0.239	0.387	0.274
Fall	0.210	0.229	0.257	0.224	0.238	0.229

2.2.3. Wave data

ERA5 reanalysis data from the European Centre of Medium-Range Weather Forecast (ECMWF), provide a comprehensive global climate dataset. ERA5 combines model data with a vast array of observations, delivering hourly estimates of atmospheric, ocean and land-surface conditions at spatial resolution of approximately 31 km. This dataset offers a high-quality representation of historical climate variables, including wind, temperature and wave parameters. In this study, long-term variations in the wave climate were determined with the ERA5 dataset, which allowed identifying seasonal variations and interannual trends in wave characteristics. Additionally, hourly wave measurements at a depth of 19.5 m were collected using a 1 MHz Acoustic Doppler Current Profiler (ADCP; AWAC from Nortek; Figure 2.2.4.1), averaging over 17-minute intervals at a frequency of 2 Hz. These data were used to characterize nearshore wave conditions between May 2017 and October 2020 (Figure 2.1.1 c).

Integral wave parameters such as the significant wave height (H_S), associated spectral peak wave period (T_P), wave direction (Dir) and directional spreading, were obtained from the spectral wave data gathered by the ADCP (Figure 2.2.3.1). Missing wave measurements between November 2015 and May 2017 were surrogated; H_s and T_p were linearly correlated with measurements from Ensenada beach (Ruiz de Alegría-Arzaburu et al., 2017) and an artificial neural network analysis applied to offshore wave data (from the WaveWatchIII IOWAGA global model) was used to estimate wave directions.

Linear wave theory was applied to the time-series of hourly wave data over the five-year period to estimate the amount of wave energy received on the coast (Ruiz de Alegría-Arzaburu *et al.*, 2022). The total wave power (P_t; Eq. 1) and the cross-shore (P_x; Eq. 2) and alongshore (P_l; Eq. 3) components were estimated at a depth, *d*, of 19.5 m as follows:

$$P_t = nEC \qquad (1)$$

$$P_x = nEC\ cos\alpha \qquad (2)$$

$$P_y = nEC\ sin\alpha\ cos\alpha \qquad (3)$$

with n being the wave group to incident celerity ratio , $n = \frac{1}{2}(1 + \frac{4\pi d/L}{sinh 4\pi d/L})$; E the wave energy density, $E = \frac{1}{16}\rho g H_s^2$; C the wave celerity, $C = \frac{gT_p}{2\pi} tanh \frac{2\pi d}{L}$; L the wavelength; and α the angle between the coastline orientation and the wave direction. Integral wave parameters and wave energy fluxes were averaged between periods of morphological surveys.

2.2.4. Near surf-zone currents

Three simultaneous bottom-mounted ADCPs (2 MHz sidelooking Aquadopp) were moored at 3.5 to 5 m depths to determine alongshore variations in near-surfzone flows throughout the water column. The moorings were installed at a secure depth beyond wave breaking and to prevent sand coverage, and they were located on beach profiles exhibiting distinct morphological variations, with a separation of 1.8 km between them.

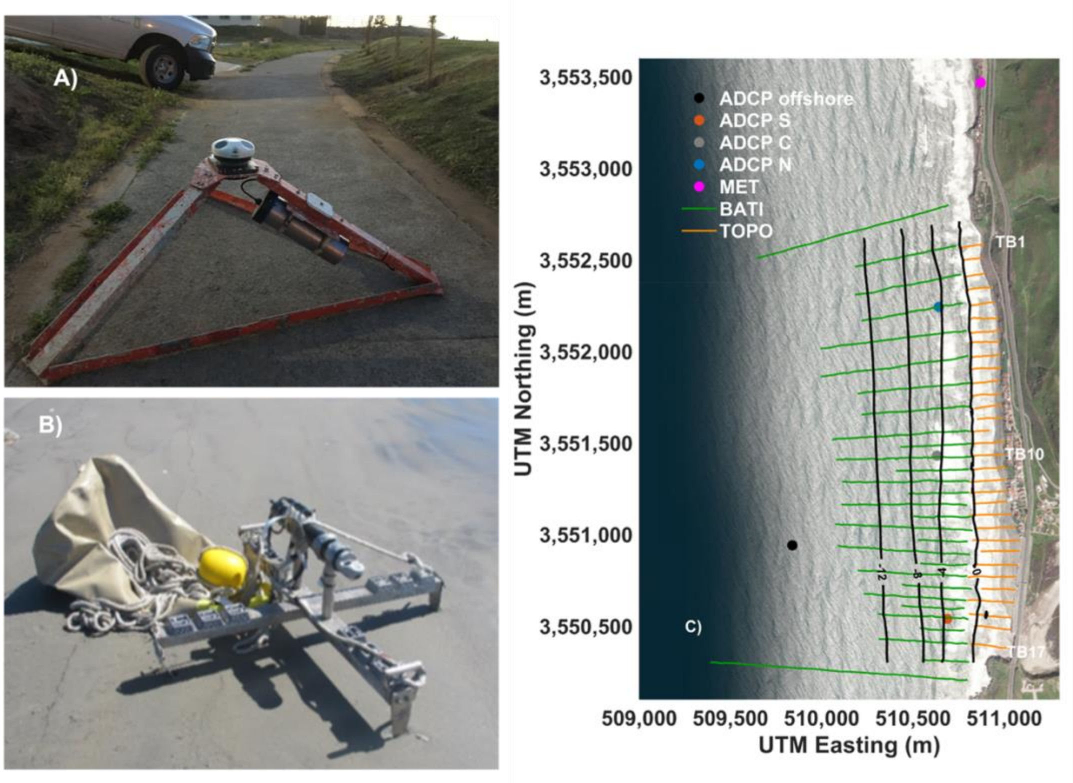

Figure 2.2.4.1 Instruments used to collect waves and current data. A) ADCP offshore, B) ADCP at Southern (S), Central (C) and Northern (N) section (Aquadopp 2MHz sidelooking). C) Location of instruments.

Figura 2.2.4.1. Instrumentos utilizados para colectar datos de oleaje y corrientes. A) ADCP mar adentro, B) ADCP en la sección Sur (S), Centro (C) y Norte (N) (Aquadopp 2MHz sidelooking), C) Localización de los instrumentos.

Current profiles were recorded continuously at 1 Hz for a two-week period from the 21st of September to the 7th of October 2021. The data were collected across 70 vertical bins of 0.1 m resolution, with a blanking distance of 0.1 m from the seabed, and the velocity components were rotated 4° clockwise to align them to the shoreline orientation. Data with instrument tilting angles greater than 20° were omitted and the uppermost 0.2 m of the water column (2 bins) were discarded due to sidelobe interference with the water surface. A right-handed east-north-up coordinate system was used; thus, positive cross-shore x (u), and longshore, y (v), flows were offcoast and upcoast directed.

The time-series of surface pressure (P) and orbital velocities (U,V) throughout the water column were analyzed following the PUV method (Pedersen et al., 2005), which assumes the presence of waves arriving from a primary direction at each frequency band. This involved separating signals per frequency band through a Fourier transform to isolate each wave direction. The directional spectrum was then computed using the parametric function specified by Pedersen et al. (2005), (Eq. 4):

$$E(f,\theta) = \mathrm{S(f)} * D(f,\theta) \qquad (4)$$

where E represents the energy density spectrum; S the wave density spectrum for individual frequencies denoted as f; and D the directional wave energy that depends on both frequency and direction.

A mid-water column layer between 1.5 m and 2.5 m depth (lower limit 1.5 m from seabed) was selected to calculate both the undertow flow and the wave orbital velocity skewness. The undertow, responsible for offshore sediment transport, was identified as an offshore directed mean flow (averaged over 1024 s), and compared to the equation proposed by Masselink and Black (1995) (Eq. 5) based on linear wave theory:

$$U = \frac{\frac{1}{8}\sqrt{\frac{g}{h}}\gamma^2 h}{1-\frac{\gamma}{2}}\left[\exp\left(-\left(\gamma\frac{h}{H_0}\right)^2\right)\right] \qquad (5)$$

with *g* being the gravitational acceleration, *h* the mean water depth, *Hₒ* the offshore wave height and γ the breaker index (set to 0.7).

The wave skewness (Sk) outside the surfzone produces net onshore sediment transport (Mariño-Tapia et al., 2007; Fernández-Mora et al., 2015; Grossmann et al., 2023). Sk was computed at both the northern and southern near-surfzone ADCP locations for the cross-shore Sk (u) and alongshore Sk (v) components (Eq. 6 and 7) following Mariño-Tapia et al., (2001):

$$\langle Sk(u)\rangle = \frac{\langle (u)^3\rangle}{\langle (u)^2\rangle^{3/2}} \qquad (6)$$

$$\langle Sk(v)\rangle = \frac{\langle (v)^3\rangle}{\langle (v)^2\rangle^{3/2}} \qquad (7)$$

where $\langle (u)\rangle$ and $\langle (v)\rangle$ corresponded to de-meaned 17-min averaged (1024 s bursts) cross-shore and longshore velocities for the selected mid water layer.

2.3. Berm and sandbar detection

Sandbar and berm positions were extracted from measured topo-bathymetric (TB) profiles over the 5-year study period (see dots and triangles in Figure 2.3.1.). First, each cross-shore (x) profile was subjected to linear interpolation at 0.1 m intervals. These profiles were then plotted against a reference profile derived from an exponential function $\mathrm{Ae}^{\mathrm{bx}}$, which was adjusted through least square fitting to the measured profile data, resulting in coefficients *A* and *b*. This method aligns with the approach taken by Ruessink and Kroon in 1994.

Reference profiles varied for each TB profile due to their distinct slopes. The maximum anomaly, representing the difference between measured and refence profiles, indicated the locations of berms and sandbars (Figure 2.3.1.). These positions were manually extracted in instances where multiple berms or sandbars were present, or in specific cases when crests exhibited a flat peak. This approach aligns with methods employed by Phillips et al. (2019), for instance. Feature elevations (Z_b) were defined relative to MLLT (m) and their cross-shore distances (X_b) were referred to Z=0 as November 2015 (the initial field survey). Morphological feature positions extracted from individual TB profiles were plotted against DEMs representing the morphological evolution at specific months representative of seasonal variations (Figure 2.3.1.).

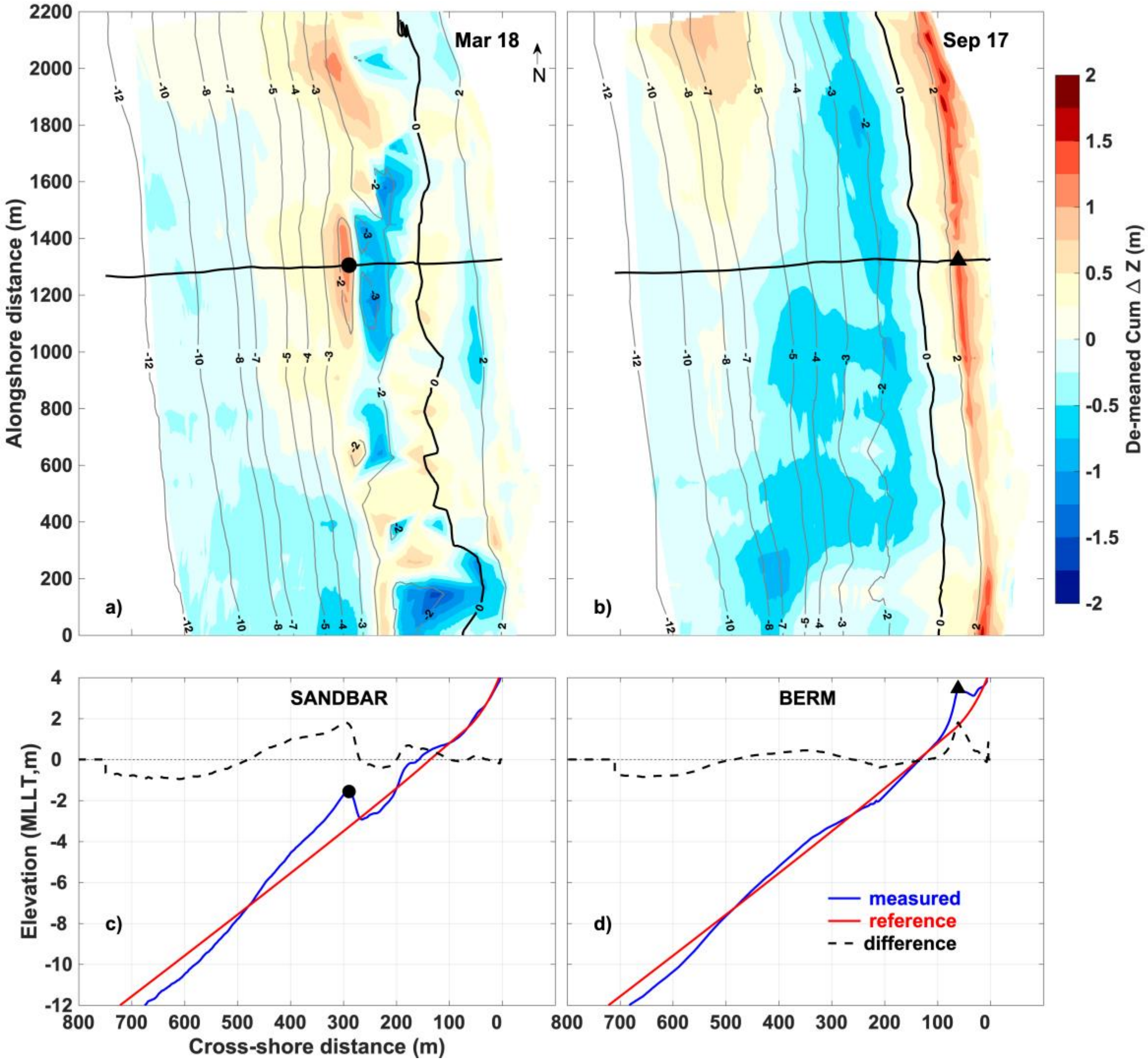

Figure 2.3.1. Example Digital Elevation Models (DEM) calculated from interpolating measured TB profiles for (a) March 2018 and (b) September 2017. The colorbar denotes accretion and erosion in warm and cold colors, respectively. The positions of sandbars (dot) and berms (triangle) from highlighted profiles in (a) and (b) are plotted in (c) and (d). Measured and reference profiles are denoted as blue and red lines, and the difference between them are the black dashed lines.

Figura 2.3.1. Ejemplos de Modelos Digitales de Elevación (DEM) calculados a partir de la interpolación de perfiles TB medidos para (a) marzo de 2018 y (b) septiembre de 2017. La barra de colores indica acreción y erosión mediante colores cálidos y fríos, respectivamente. Las posiciones de las barras de arena (puntos) y bermas (triángulos) de los perfiles destacados en (a) y (b) se muestran en (c) y (d). Los perfiles medidos y de referencia se representan con líneas azul y roja, respectivamente, y la diferencia entre ellos se indica con líneas negras discontinuas.

2.4. Modeling the nearshore circulation using XBeach

The XBeach (XB) third-generation process-based open-source numerical model was implemented at La Misión Beach for determining the spatial variability of waves and currents for different morphodynamic beach conditions. The model was developed by UNESCO-IHE and Deltares and was originally designed to assess the erosion of beaches and coastal dunes under the impact of storm waves (Roelvink et al., 2009).

In this study, the hydrostatic version of the model was used, which considers wave transformation processes in a single layer, and divides the wave spectrum into long-frequency (0.004–0.04 Hz or 5–30 s) and short-frequency waves (0.04–2 Hz or 30–300 s) to save computational time, in exchange for not simulating the phase of short waves. The threshold for frequency separation, f_{split} = 0.04 Hz depend on the mean period of the incident waves and is adjusted for each study case. Wave propagation and dissipation processes, as well as the effects of refraction, shoaling, and breaking were coupled with morphological equations that included bedload and suspended sediment, sediment transport, and erosion of the bed and dunes by overwash. See Appendix A and Appendix B for further details on the model description and parameters, respectively.

Numerical simulations were performed in two dimensions (2DH) using a staggered grid size of 263 x 209, with grid cell resolution of 16 m alongshore (Δy) and cross-shore (Δx) at depths ranging from 10 to 40 m, and with an alongshore resolution of 16 m and 4 m in the cross-shore for shallower depths above 10 m. The lateral boundaries (northern and southern) were set as neumann, while the front boundary (offshore) was set as abs2D at the 40-m isobath and fed by offshore ADCP data at 20m of depth (Figure 2.2.4.1 c). In order to get a better performance of wave propagation, a buffer zone of 500 m was added for the lateral boundaries (Figure 2.4.1). The wave boundary conditions were set as a JONSWAP wave spectrum, using the time series of H_s, T_p, wave direction and directional spreading obtained from the offshore ADCP measurements, and a peak enhancement of 3.3 (default) was used. The tidal signal was set in the front boundary (offshore) as the time series of water levels (referred to MLLT) derived from the offshore ADCP data. In order to consider the formation of tidal-induced alongshore currents, a tideloc = 4 was used which means that the tidal signal is applied along the entire boundary of the domain, including the open boundary and the lateral sides.

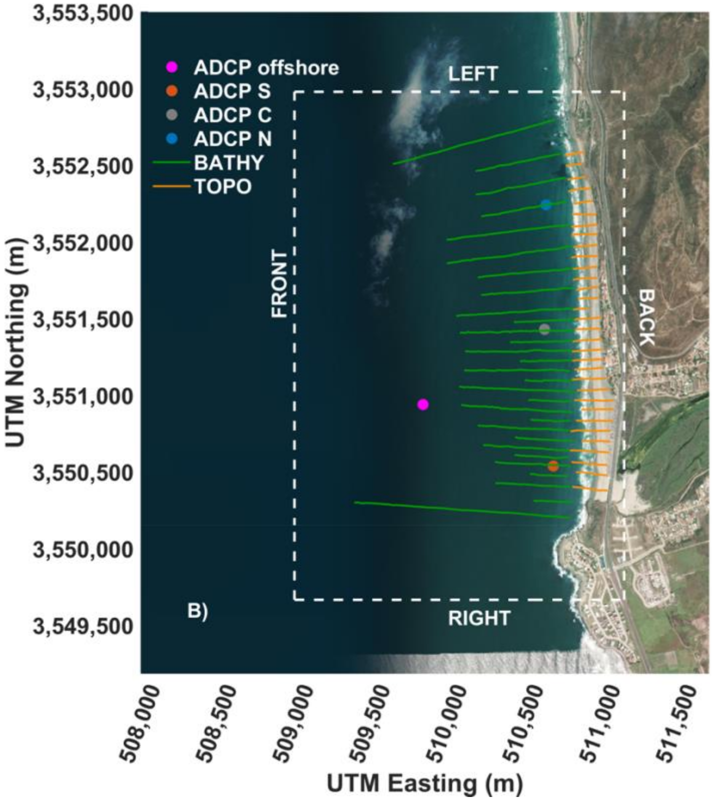

Figure 2.4.1 Limits of the boundaries for XBeach at La Misión beach.

Figura 2.4.1 Límites de las fronteras para XBeach en playa La Misión.

References

Blott, S. J., & Pye, K. (2001). GRADISTAT: a grain size distribution and statistics package for the analysis of unconsolidated sediments. *Earth Surface Processes and Landforms*, *26*(11), 1237–1248. https://doi.org/https://doi.org/10.1002/esp.261

Durazo, R., Flores-Vidal, X., Castro, R., Ocampo-Torres, F. J., Saavedra, J., Rodríguez-Padilla, I., & Larrañaga, M. (2024). Surface circulation in Todos Santos Bay, Baja California, México. *Continental Shelf Research*, *273*, 105171. https://doi.org/https://doi.org/10.1016/j.csr.2024.105171

Fernández-Mora, A., Calvete, D., Falqués, A., & de Swart, H. E. (2015). Onshore sandbar migration in the surf zone: New insights into the wave-induced sediment transport mechanisms. *Geophysical Research Letters*, *42*(8), 2869–2877. https://doi.org/https://doi.org/10.1002/2014GL063004

Folk, R. L., & Ward, W. C. (1957). Brazos River bar [Texas]; a study in the significance of grain size parameters. *Journal of Sedimentary Research*, *27*(1), 3–26.

Grossmann, F., Hurther, D., van der Zanden, J., Sánchez-Arcilla, A., & Alsina, J. M. (2023). Near-Bed Sediment Transport Processes During Onshore Bar Migration in Large-Scale Experiments: Comparison With Offshore Bar Migration. Journal of Geophysical Research: Oceans, 128(3), e2022JC018998. https://doi.org/https://doi.org/10.1029/2022JC018998

Mariño-Tapia, I., Russell, P. E., O’Hare, T. J., Davidson, M. A., & Huntley, D. A. (2007). Cross-shore sediment transport on natural beaches and its relation to sandbar migration patterns: 1. Field observations and derivation of a transport parameterization. Journal of Geophysical Research: Oceans, 112(C3). https://doi.org/https://doi.org/10.1029/2005JC002893

Mariño-Tapia, I., Russell, P.E., O'Hare, T.J., Davidson, M.A., Saulter, A.N., Miles, J.M., and Huntley, D.A. (2001). Relationship between vertical wave asymmetry and the fourth velocity moment in the surf zone: implications for sediment transport, In: B.L. Edge and J.M. Hemsley (eds), Proceedings of the Fourth International Symposium Waves 2001 (San Francisco), American Society of Civil Engineers, Virginia, USA, 1295-1305.

Masselink, G., & Black, K. P. (1995). Magnitude and cross-shore distribution of bed return flow measured on natural beaches. Coastal Engineering, 25(3), 165–190. https://doi.org/https://doi.org/10.1016/0378-3839(95)00002-S

Pedersen, T., Lohrmann, A., Krogstad, H.E. (2005). Wave measurements from a subsurface platform. Proceedings WAVES 2005, Madrid, Spain.

Phillips, M. S., Blenkinsopp, C. E., Splinter, K. D., Harley, M. D., & Turner, I. L. (2019). Modes of Berm and Beachface Recovery Following Storm Reset: Observations Using a Continuously Scanning Lidar. *Journal of Geophysical Research: Earth Surface*, *124*(3), 720–736. https://doi.org/https://doi.org/10.1029/2018JF004895

Roelvink, D. , Reniers, A. , Van-Dongeren, A. , Van-Thiel-de-Vries, J. , McCall, R. & Lescinski, J. (2009). Modelling storm impacts on beaches, dunes and barrier islands, Coastal Engineering, 56(11-12), 1133-1152.

Ruessink, B. G., & Kroon, A. (1994). The behaviour of a multiple bar system in the nearshore zone of Terschelling, the Netherlands: 1965–1993. *Marine Geology*, *121*(3), 187–197. https://doi.org/https://doi.org/10.1016/0025-3227(94)90030-2

Ruiz de Alegría-Arzaburu, A., Gracia-Barrera, A. D., Kono-Martínez, T., & Coco, G. (2022). Subaerial and upper-shoreface morphodynamics of a highly-dynamic enclosed beach in NW Baja California. *Geomorphology*, *413*, 108336. https://doi.org/https://doi.org/10.1016/j.geomorph.2022.108336

Ruiz de Alegría-Arzaburu, A., Vidal-Ruiz, J. A., García-Nava, H., & Romero-Arteaga, A. (2017). Seasonal morphodynamics of the subaerial and subtidal sections of an intermediate and mesotidal beach. *Geomorphology*, *295*, 383–392. https://doi.org/https://doi.org/10.1016/j.geomorph.2017.07.021

CHAPTER 3. Alongshore variability in berm and sandbar migration patterns on a highly dynamic beach[1]

[1] This chapter is based on an article published in Geomorphology: *Kono-Martínez, T., Ruiz de Alegría-Arzaburu, A., Mariño-Tapia, I., Coco, G., 2023. Alongshore variability in berm and sandbar migration patterns on a highly dynamic beach. Geomorphology, 443, 108935. ISSN:0169-555X. IF:4.1. https://doi.org/10.1016/j.geomorph.2023.108935*

Abstract

Sediment exchange between the shoreface and the foreshore is investigated through the analysis of sandbar and berm migration cycles at La Misión beach in Baja California, Mexico. In general, nearshore sandbars migrate onshore during low-energy wave conditions merging with the shoreline to become intertidal sandbars that later contribute to berm rebuilding. However, significant alongshore differences were observed in the sandbar welding and berm rebuilding process, which can be attributed to wave skewness of the demeaned alongshore component and near-surfzone flow variations. The analysis of topographic and bathymetric surveys collected monthly over a 5-year period revealed larger shoreline retreat and longer recovery times in the southern beach compared to the north. This was related to the inability of sandbars to weld to the intertidal beach during spring and summer, occurring only during extended periods of low-energy waves. In the southern beach, the berm formation process exhibited less dependence on incoming wave energy, persisting during mild-energy winters, and reforming in the presence of sandbars. Hydrodynamic measurements indicated that the southern part of the beach experienced relatively more intense net offshore flows (up to -0.2 ms^{-1}) due to undertow, and possibly related to the presence of persistent rip currents. In contrast, the berm in the northern beach followed a seasonal erosion and rebuilding process associated with sandbar migrations driven by variations in incoming wave energy and cross-shore sediment transport. This was characterized by larger near-bed wave velocity skewness compared to the south. Net flows in the north were predominantly onshore, reaching up to 0.1 ms^{-1} during lower-energy periods with oblique wave incidence. This study reveals the presence of considerably distinct sandbar and berm migration cycles along a relatively short beach of 2.2 km long. It also highlights how such variability can be related to the morphodynamic feedback with sandbars affecting hydrodynamics, particularly near-bed wave skewness and near-surfzone flow variations, which in turn influence sediment transport and morphological evolution.

Resumen

El intercambio de sedimentos entre la plataforma continental interna y la zona intermareal se investiga mediante el análisis de los ciclos de migración de barras y bermas en la playa La Misión, Baja California, México. En general, las barras submareales cercanas a la costa migran hacia tierra durante condiciones de oleaje de baja energía, uniéndose con la línea de costa para convertirse en barras intermareales, que posteriormente contribuyen a la reconstrucción de la berma. Sin embargo, se observaron diferencias significativas a lo largo de la costa en los procesos de unión de la barra y reconstrucción de la berma. Estas diferencias pueden atribuirse a la asimetría del oleaje en la componente longitudinal y a variaciones en los flujos en la zona de rompiente. El análisis de los levantamientos topográficos y batimétricos recolectados mensualmente durante un periodo de 5 años reveló un mayor retroceso de la línea de costa y tiempos de recuperación más prolongados en la sección sur de la playa en comparación con el norte. Esto se relacionó con la incapacidad de las barras de arena para unirse a la zona intermareal durante la primavera y el verano, durante periodos prolongados de oleaje de baja energía. En la sección sur, la formación de la berma mostró menor dependencia en la energía del oleaje entrante, persistiendo durante inviernos de energía moderada, incluso reformándose en presencia de barras cercanas a la costa. La parte sur de la playa experimentó flujos netos hacia mar adentro relativamente más intensos (de hasta -0.2 m/s), debidos a corrientes de resaca y posiblemente corrientes de retorno persistentes. En contraste, la berma en la sección norte mantuvo un proceso estacional de erosión y reconstrucción asociado con la migración de la barra, impulsada por variaciones en la energía del oleaje entrante y el transporte de sedimentos transversal. En el norte, la asimetría de la velocidad del oleaje cerca del fondo fue mayor que en el sur, adicionalmente, los flujos netos en el norte fueron predominantemente hacia la costa, alcanzando hasta 0.1 m/s durante periodos de baja energía con incidencia oblicua del oleaje. Este estudio revela la existencia de ciclos de formación de barra-berma considerablemente distintos a lo largo de una playa relativamente corta de 2.2 km de longitud. Destaca cómo dicha variabilidad puede estar relacionada con retroalimentaciones morfodinámicas, en las que la barra afecta la

hidrodinámica —particularmente la asimetría del oleaje cerca del fondo y las variaciones del flujo en la zona de rompiente—, lo que a su vez influye en el transporte de sedimentos y la evolución morfológica.

3.1. Introduction

Understanding the spatio-temporal exchange of sediment between the upper and lower shoreface and the subaerial beach is essential for improving our ability to predict coastal sediment budgets (Anthony and Aagaard, 2020). Variations in wave energy lead to changes in sediment transport both in terms of magnitude and direction across the beach profiles. Typically, storms result in erosion of the upper beach and the formation of sandbars that move the eroded sediment offshore (Shepard, 1950; Komar, 1974). The farther these sandbars migrate seaward during high-energy conditions, the longer it takes for the sediment to return to the shore, which usually occurs during periods of low wave-energy (Hsu et al., 2006; Ruessink et al., 2007; Vidal-Ruiz and Ruiz de Alegría-Arzaburu, 2020). The recovery of the subaerial beach after a storm, often referred to as beach rebuilding, is typically characterized by the formation and growth of a berm. This process is driven by onshore sediment transport and its subsequent rework by swash processes (Hine, 1979; Phillips et al., 2019).

The berm of a beach is a constructional morphological feature with a triangular cross-section and a quasi-planar surface that extends seaward from the dune toe, often separated by a distinctive slope change from the steeper beach face (King 1959; Hine, 1979; Masselink and Hughes, 2003). During low-energy wave conditions, sandbars migrate landward and weld to the shoreline, transferring sediment to the intertidal beach (Vidal-Ruiz and Ruiz de Alegría-Arzaburu, 2019). As a result, the onshore migration of sandbars plays a fundamental role in the overall beach recovery process (Jensen et al., 2009), while swash processes are responsible for the recovery of the beach face and the rebuilding of the berm once the sandbar has connected with the shoreline (Austin and Masselink, 2006).

The crest of the berm is typically located within the runup limit, and its formation and vertical growth are primarily influenced by the neap-spring tide cycle (Hine, 1979; Russell et al., 2009; Jensen et al., 2009). Initially, it was believed that the berm formation was controlled by the grain size, but once formed, its height appears to be independent of sediment size (Sunamura, 1989). Hine (1979) defined three mechanisms driving berm development, including: (1) the contribution of the upper neap high-tide limit; (2) the landward migration and welding of the swash sandbar to the beach face; and (3) the presence of an intertidal sandbar with a crest at the same elevation as the spring high-tide level.

During the process of rebuilding, the subaerial beach has the capacity to either extend the beach face seaward (progradation) or grow the berm vertically (aggradation) (Dubois, 1988). The choice between these options largely depends on the characteristics of the swash relative to the berm crest elevation (Baldock et al., 2008). However, it is possible for both progradation and aggradation processes to occur concurrently during berm recovery, meaning that beach face extension and berm heightening can occur simultaneously. Additionally, one can observe beach face erosion either with or without berm aggradation (Weir et al., 2006; Phillips et al., 2019). Prior research has indicated that once a berm is established, swash overtopping can lead to berm growth and concurrent sediment accumulation on the beach face (Weir et al., 2006; Austin and Masselink, 2006). Despite the relevant role of berms in long-term sediment budgets, the comprehension of the mechanisms governing their rebuilding remains limited (Puleo and Torres Freyermuth, 2016).

The cycles of sandbar and berm erosion and rebuilding processes have been extensively examined individually in existing literature. For example, previous studies assumed an alongshore uniform distribution of sandbars (Ruessink et al., 2007) and berms (Jensen et al., 2009; Castelle et al., 2017; Philips et al., 2019) along different beaches. Other studies have focused on understanding alongshore variations of sandbar in relation to nearshore flows (Shand et al., 1999) or slope changes and sandbar morphometrics (Tātui et al., 2011; Aleman et al., 2013; Melito et al., 2020). To our knowledge, this study shows the cyclic coupling of sandbars and berms over multiple years along a beach with complex morphology.

3.2. Methods

Wave data were gathered hourly from May 2017 to October 2020 using an offshore ADCP, with missing data estimated through correlations and neural network analysis. Wave energy and direction were analyzed to understand their impact on coastal dynamics. Additionally, nearshore currents were measured with bottom-mounted ADCPs to assess alongshore variations in flow, focusing on wave skewness and undertow.

Beach surveys were conducted nearly monthly from November 2015 to October 2020, involving topographic profiles spaced 50 meters apart and bathymetric profiles extending to depths of 12 meters. The data were collected using RTK GPS for topography and a jetski-mounted Sontek Hydrosurveyor ADCP for bathymetry. Morphological features such as sandbars and berms were manually detected and plotted on the digital elevation models (DEMs). These DEMs provided a detailed view of the beach's morphological evolution over the five-year period by subtracting the mean and calculating the cumulative differences.

3.3. Results

3.3.1. Nearshore wave characteristics

La Misión beach experienced highly seasonal wave characteristics over the 5-year study period from 2015 to 2020. Nearshore measurements showed maximum recorded H_s of 5 m with a T_p of 17 s and an associated P_t of approximately190 kWm^{-1} for predominant wave directions from the SW-W. The most energetic single event occurred in January 2017 and other high wave energy conditions happened during the El Niño 2015-2016 and 2018-2019 winters (Figure 3.3.1.1.). Average winter (November-to-April) waves were H_s = 1.5–1.8 m and T_p = 12 s during very energetic conditions (averaged P_t >20 kWm^{-1}) typical of El Niño years (i.e. 2015–2016 and 2018–2019), and H_s = 1.2 m and T_p = 11 s during less energetic conditions (averaged P_t <20 kWm^{-1}) corresponding to La Niña (i.e. 2017–2018) and neutral (i.e. 2019–2020) years (Figure 3.3.1.1.).

The summer periods (May-to-October) were characterized by low-energy conditions (averaged P_t<10 kWm^{-1}) with slight interannual variations and average H_s = 1 m and T_p =11 s. Waves were predominantly from SW in summer (220 to 250 degrees) and from W (260 to 280 degrees) in winter (Figure 3.3.1.1.c). Directional spectra results showed unimodal wave dominance of high energy in winter (predominantly from W; Figure 3.3.1.1.e), lesser energy in spring (Figure 3.3.1.1.f), and lower energy bimodal conditions in summer and fall (Figure 3.3.1.1.g).

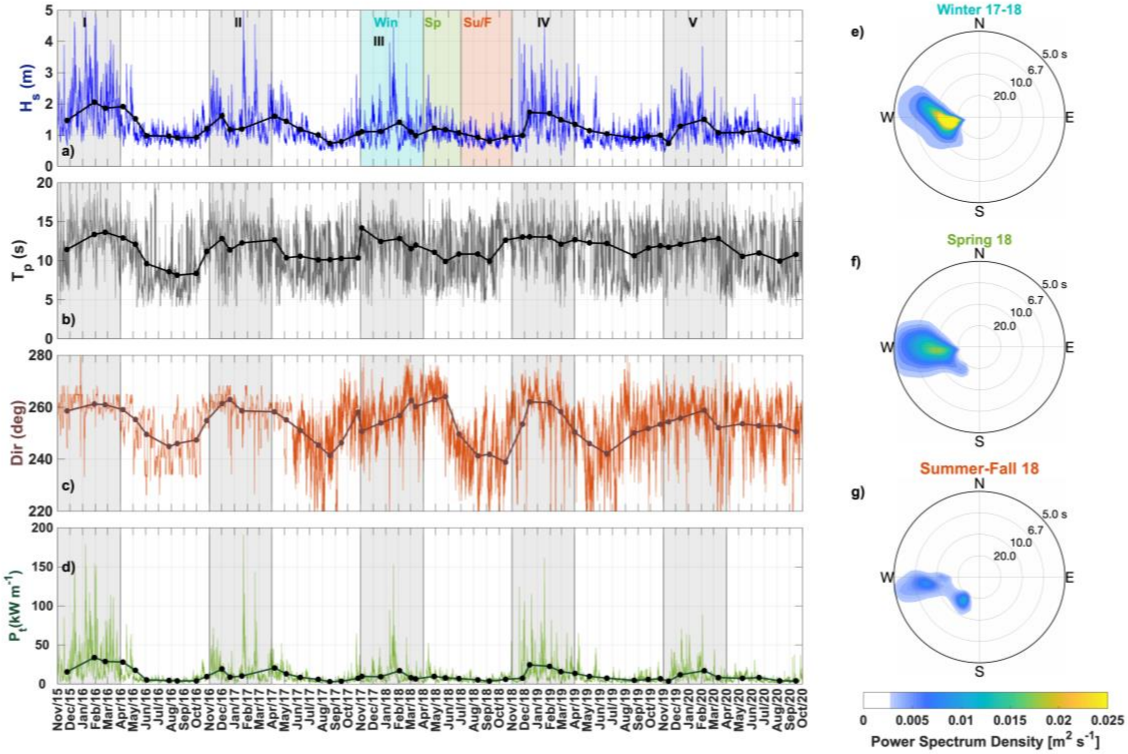

Figure 3.3.1.1 Solid lines represent hourly data, whereas dotted lines represent averaged data between survey times for the following parameters: (a) significant wave height (H_s); (b) spectral peak wave period (T_p); (c) average wave direction (Dir); and (d) total wave power averaged per survey period (P_t) between November 2015 and October 2020. Directional wave spectra for the 2017-2018 winter and 2018 spring and summer are presented in (e), (f) and (g), respectively. Shadowed gray/blue sections correspond to winter wave conditions (November to March) each year (I to V) and spring (green) and summer/fall (orange) represented April to June and July to October in 2018, respectively.

Figura 3.3.1.1. Las líneas sólidas representan datos horarios, mientras que las líneas punteadas representan datos promediados entre los tiempos de levantamiento para los siguientes parámetros: (a) altura significativa del oleaje (H_s); (b) periodo pico espectral del oleaje (T_p); (c) dirección media del oleaje (Dir); y (d) potencia total del oleaje p (Pt) entre noviembre de 2015 y octubre de 2020. Los espectros direccionales de oleaje para el invierno 2017-2018 y la primavera y verano de 2018 se presentan en (e), (f) y (g), respectivamente. Las secciones sombreadas en gris/azul corresponden a condiciones de oleaje invernal (de noviembre a marzo) de cada año (I a V), y la primavera (en verde) y el verano/otoño (en naranja) representan de abril a junio y de julio a octubre de 2018, respectivamente.

3.3.2. Morphodynamic state transitions on sandbar and berm positions

Seasonal morphodynamic beach state transitions were observed at La Misión beach, and the position of subaerial and subtidal morphological features varied significantly throughout the duration of the five-year investigation, spanning from 2015 to 2020. Figure 3.3.2.1 illustrates morphological changes in the beach, superimposed with the positions of the sandbar (indicated by dots) and the berm (represented by triangles), corresponding to particular months that exemplify each season, across the various years. Usually, the upper part of the beach undergoes erosion in the late fall and winter seasons, leading to the formation of a sandbar. This sandbar then moves towards the shore in periods of lower energy, which occur in spring and summer. This movement facilitates the recovery of the upper beach area and the reconstruction of the berm.

The most significant erosive conditions coincided with the most intense El Niño winters (2015-2016 and 2018-2019; depicted in Figure 3.3.1.1. I and IV), which triggered extensive erosion of the upper beach (vertical changes exceeding 2 m), leading to the migration of the outer sandbar farthest offshore up to depths of 4 and 5 m (see 16 and 19 in Figure 3.3.2.1 I). The upper sections of both the northern and southern beach experienced the most substantial erosion, yet the berm was preserved at selected locations in the southern area (Figure 3.3.2.1 I).

The reduction in wave energy during spring favored the transport of sediment towards the shore. Following winters with the least energy, the berm experienced partial recovery in spring, due to the sandbar nearing the shoreline (see 18 and 20 in Figure 3.3.2.1 II, also Figures 3.3.3.1 and 3.3.4.1.). In 2020, the recovery of the berm happened faster comparted to other years, attributed to the preceding low-energy winter conditions (Figure 3.3.1.1.). These conditions led to the formation of shallower sandbars, facilitating a quicker movement of sediment towards the shore during periods of reduced wave energy (see 20 in Figure 3.3.2.1II). On the contrary, after winters of high energy, the sandbar remained positioned farther offshore at depths exceeding 3 m, which subsequently led to a slower recovery of the berm (see 16 and 19 in Figure 3.3.2.1 II). In spring, the beach became rhythmic compared to other seasons. This can be noted through the irregular shape of the shoreline and the presence of rip channels across the intertidal beach and the surfzone. Notably, these rip channels are most pronounced along the southern section of the beach, persisting from winter through summer in the majority of years (Figure 3.3.2.1).

The calm wave conditions of summer (Figure 3.3.1.1) allowed the welding of the sandbar to the shoreline, leading to the subsequent reconstruction of the berm (Figure 3.3.2.1 III). In certain locations of the southern beach, sandbars were present at depths surpassing 3 m (Figure 3.3.2.1 III). The slight increase in wave energy during fall (Figure 3.3.1.1) induced the formation of a shallow sandbar while the berm persisted in all instances, except for the year 2016 (see 16 in Figure 3.3.2.1 V). In that particular fall, (November 2016) the berm was almost completely washed away along the beach (Figure 3.3.2.1IV fall and dashed line in Figure 3.3.3.1 I), resulting in the formation of a sandbar that migrated to depths of up to 2 m (Figure 3.3.2.1IV). In the south, the berm was small in August, while it was comparatively larger in the north (red line in Figure 3.3.3.1 I).

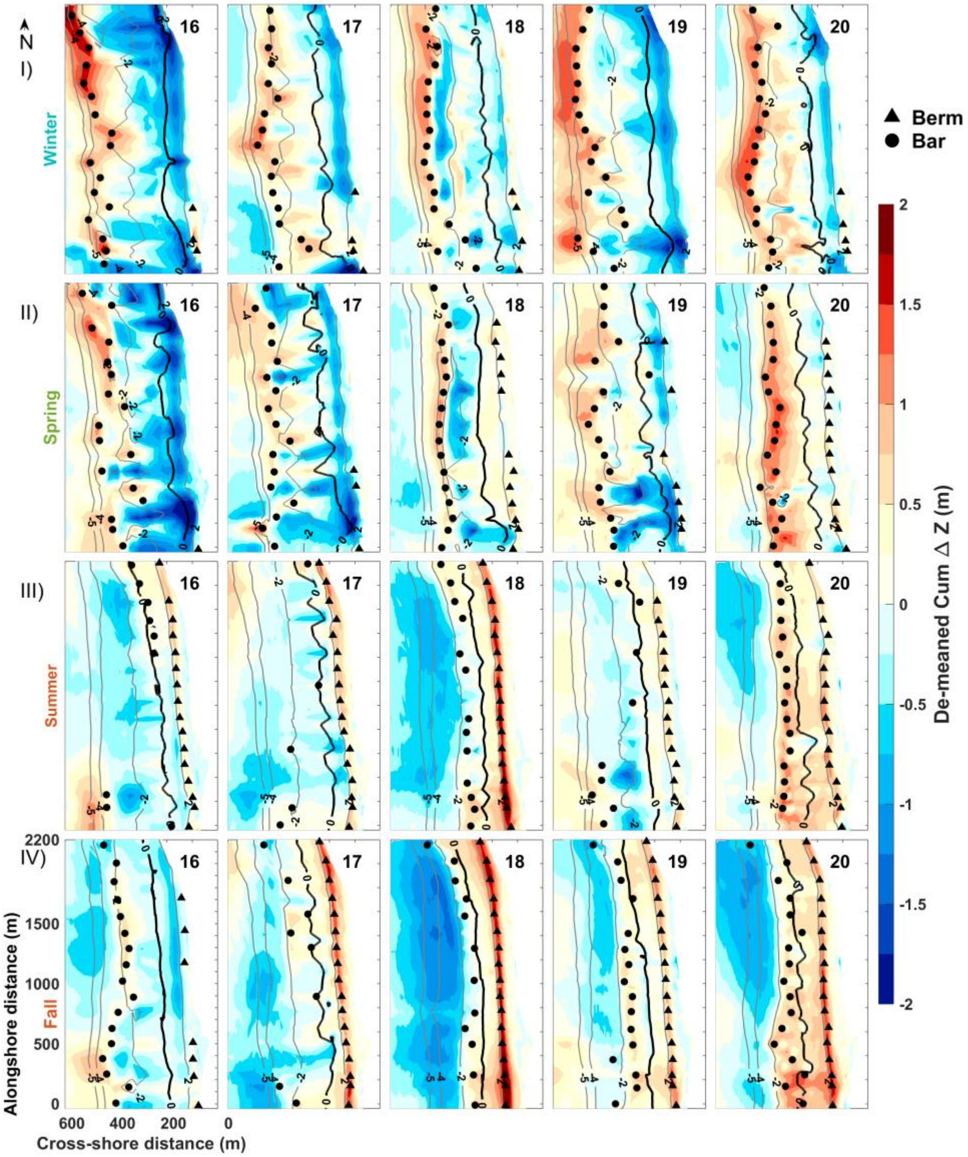

Figure 3.3.2.1 Sandbar (dots) and berm (triangle) crest locations overlaid with the winter (I; Jan-Feb), spring (II; May), summer (III; Aug) and fall (I; Nov) cumulative morphological changes from 2015-2016 to 2019-2020 (left to right columns). The thick black contourline correspond to the 0-m MLLT mark, demarcating the boundary between the subaerial and subtidal zones.

Figura 3.3.2.2 Ubicaciones de las crestas de las barras submareales (puntos) y de las bermas (triángulos) superpuestas con los cambios morfológicos acumulados de invierno (I; enero-febrero), primavera (II; mayo), verano (III; agosto) y otoño (I; noviembre) desde 2015-2016 hasta 2019-2020 (columnas de izquierda a derecha). La línea de contorno negra gruesa corresponde a la marca de 0 m MLLT, que delimita la frontera entre las zonas subaérea y submareal.

3.3.3. Berm cycle

The presence of a berm is generally indicative of the recovery of the subaerial beach (Komar, 1974; Morton et al., 1994; Phillips et al., 2019). Alongshore differences in the seasonal berm cycle over the 5-year study period were analyzed using representative beach profiles in the southern (TB16) and northern (TB3) beach (see Figure 3.3.5.1.). Typically, berms were evident during periods of low wave energy in summer and fall, situated at elevations exceeding 2.5 m, and mostly surpassing 3 m. These features experienced erosion during the winter months, and reformed during the spring and summer, reaching their peak height and volume in the fall (October; Figure 3.3.3.1).

The high-energy winter waves of 2015-2016 induced significant subaerial erosion along the beach (Figure 3.3.3.1I), resulting in the inability to completely reconstruct the berm along the beach during the subsequent low-energy period. While absent in the southern beach in May 2016 (green line in Figure 5I), the berm managed to regenerate in the north by August 2016 (red line Figure 3.3.3.1 I), but eroded rapidly thereafter and vanished by October 2016. Following the period of berm reconstruction, the crests were consistently situated at elevations of around 3 to 3.5 m along the beach by October (Figure 3.3.3.1 II to V). In specific instances, there were minor deviations in berm crest elevations, with the south experiencing slightly lower or higher levels (2.8 to 3.8 m) compared to the north (Figure 3.3.3.1 V).

The northern beach displayed berm width variations ranging from 40 to 60 m (N in Figure 3.3.3.1), whereas the southern section exhibited a broader range spanning 25 to 95 m (S in Figure 3.3.3.1). For instance, by October 2017 (Figure 3.3.3.1 III), the berm crest was positioned at the same elevation of 3 m and at a cross-shore distance of 60 m in both locations. Although both crests eroded by January 2018 and underwent reconstruction during the summer-fall period, the berm in the southern section expanded to a width of 90 m, while the one in the northern section maintained a consistent width of 60 m by October 2018 (Figure 3.3.3.1 III). Despite variations in subaerial beach erosion and berm widths between the northern and southern sections, both areas managed to restore the berm crest to a similar elevation over the course of different years (Figure 3.3.3.1).

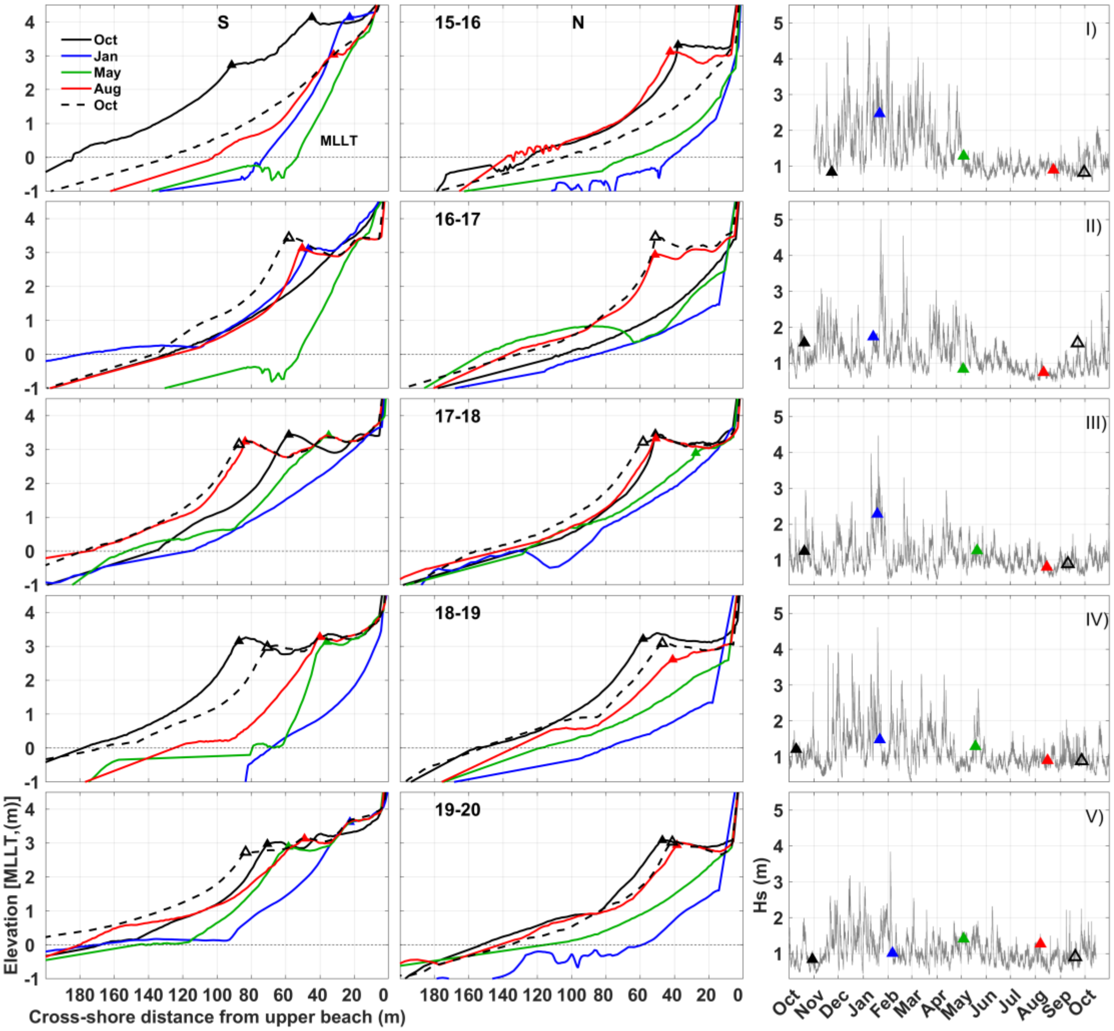

Figure 3.3.3.1 Berm evolution for representative profiles in the south (S, TB16, left column) and north (N, TB3, middle column) and the corresponding wave height (H_s) time-series (right column) for the 5-year study period: (I) from October 2015 to October 2016; (II) from October 2016 to October 2017; (III) from October 2017 to October 2018; (IV) from October 2018 to October 2019: and (V) from October 2019 to October 2020. Continuous and dashed black lines represent initial and final conditions each year in October, respectively. The cross-shore distance is calculated from Z=6 m in the upper beach for both profiles. Triangles in the right column indicate the exact day of morphological surveys.

Figura 3.3.3.1. Evolución de la berma para perfiles representativos en el sur (S, TB16, columna izquierda) y en el norte (N, TB3, columna central), y la serie temporal correspondiente de altura significativa del oleaje (Hs) (columna derecha) para el periodo de estudio de 5 años: (I) de octubre de 2015 a octubre de 2016; (II) de octubre de 2016 a octubre de 2017; (III) de octubre de 2017 a octubre de 2018; (IV) de octubre de 2018 a octubre de 2019; y (V) de octubre de 2019 a octubre de 2020. Las líneas negras continuas y discontinuas representan las condiciones iniciales y finales de cada año en octubre, respectivamente. La distancia transversal a la costa se calcula desde Z = 6 m en la parte alta de la playa para ambos perfiles. Los triángulos en la columna derecha indican el día exacto de los levantamientos morfológicos.

3.3.4. Sandbar cycle

Over the span of the 5-year study, there were notable variations in both the shape and placement of sandbars across and along the beach (Figure 3.3.4.1.). Most energetic winter conditions were induced by El Niño years (see H_s in Figure 3.3.4.1. I and IV). The incidence of a sequence of highly energetic storms with significant wave heights (H_s) exceeding 4.5 m (Figure 3.3.4.1. II) resulted in maximum seaward migrations of sandbars, positioning them at cross-shore distances of 350-400 m and depths of 3-3.5 m (green lines in Figure 3.3.4.1. II). In contrast, during winters of mild-to-low energy (Figure 3.3.4.1. III and V), sandbars were located at cross-shore distances of 270-330 m and depths of 2-3 m. In most cases, sandbars migrated towards the shore during low wave-energy conditions in spring and summer, eventually merging with the shoreline by the end of the summer season (Figure 3.3.4.1.).

A steep outer sandbar was formed as a result of highly energetic El Niño 2015-2016 winter waves (blue lines; Figure 3.3.4.1. I), and two additional inner sandbars were observed along the beach in spring (green line; Figure 3.3.4.1. I). Accretion was evident at the upper beach of both sides by summer (red lines; Figure 3.3.4.1. I), as the outer sandbar merged with the intertidal beach. Following the low-energy winter period in 2017, significant morphological differences occurred between the northern (N) and southern (S) sections (blue and green lines in Figure 3.3.4.1.II). During the subsequent summer, the outer sandbar merged with the intertidal beach in the north (became barless), whereas it remained stable at a depth of 2 m in the southern section (red lines; Figure 3.3.4.1. II).

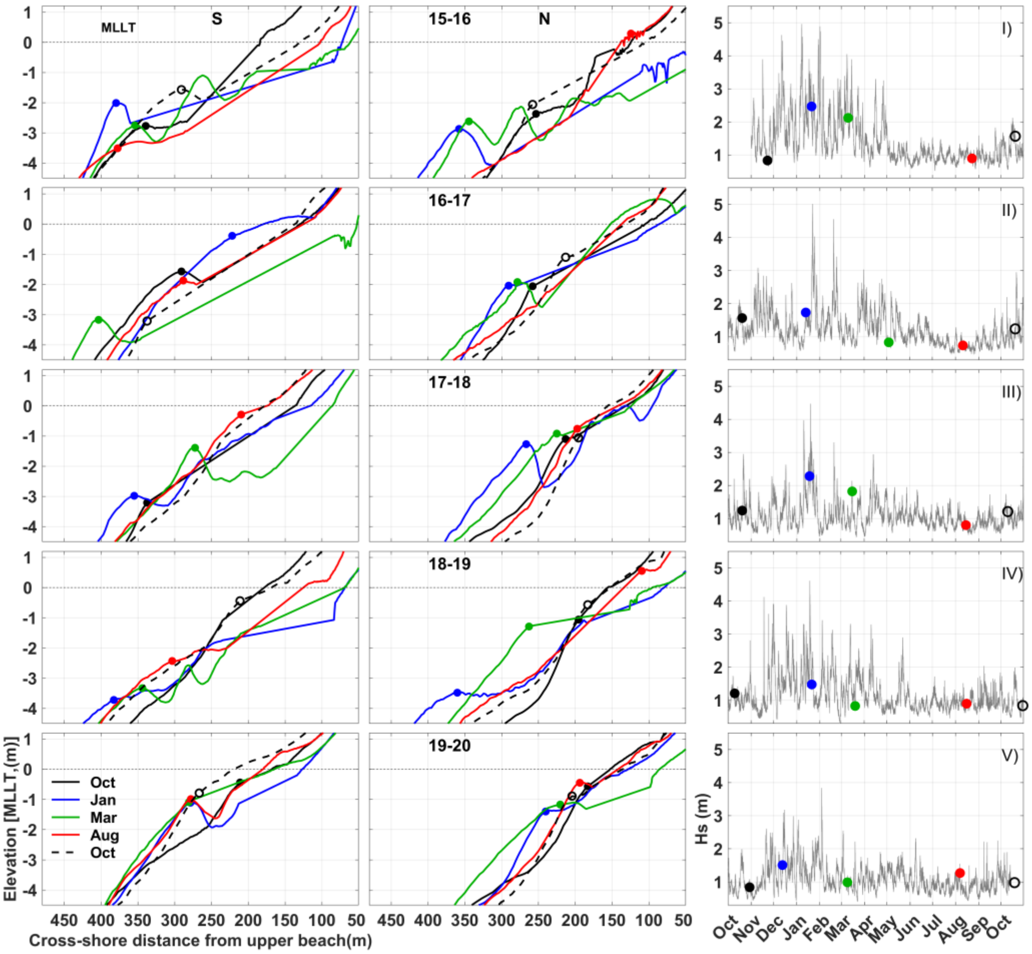

Figure 3.3.4.1 Sandbar evolution for representative profiles in the north (N; TB3) and south (S; TB16) and the corresponding wave height (H_s) time-series for the 5-year study period: (I) from October 2015 to October 2016; (II) from October 2016 to October 2017; (III) from October 2017 to October 2018; (IV) from October 2018 to October 2019: and (V) from October 2019 to October 2020. The cross-shore distance is calculated from Z=6 m in the upper beach for both profiles. The color scheme designates black to represent fall (Oct), blue for winter (Jan), green for spring (Mar), and red for summer (Aug).

Figura 3.3.4.1. Evolución de la barra submareal para perfiles representativos en el norte (N; TB3) y en el sur (S; TB16), junto con la serie temporal correspondiente de altura significativa del oleaje (Hs) para el periodo de estudio de 5 años: (I) de octubre de 2015 a octubre de 2016; (II) de octubre de 2016 a octubre de 2017; (III) de octubre de 2017 a octubre de 2018; (IV) de octubre de 2018 a octubre de 2019; y (V) de octubre de 2019 a octubre de 2020. La distancia transversal a la costa se calcula desde Z = 6 m en la parte alta de la playa para ambos perfiles. El esquema de colores asigna el negro para representar el otoño (octubre), azul para el invierno (enero), verde para la primavera (marzo) y rojo para el verano (agosto).

During the mid-energy winter conditions of 2017-2018, a shallow (1.3 m depth) and steep outer sandbar formed in the northern section, while a deeper (3 m) sandbar of lower-amplitude formed in the southern beach by January (blue lines in Figure 3.3.4.1. III). At both sites, sandbars migrated onshore during the low-energy period, approaching the shoreline by August (red lines in Figure 3.3.4.1. III).

Sandbars formed near the shoreline in October 2018, and underwent rapid offshore migration to depths reaching 3.5 m by January 2019 due to the energetic El Niño waves of 2018-2019 (blue lines in Figure 3.3.4.1. IV). In spring, a double-bar system prevailed in the south, while a steep single sandbar was observed in the north (green lines in Figure 3.3.4.1. IV). The sandbar welded the intertidal beach by August 2019 in the north, while a low-amplitude sandbar remained at a depth of 2.5 m in the south (red lines in Figure 3.3.4.1. IV).

During the period of lowest energy winter conditions in 2019-2020, sandbars exhibited relatively consistent and shallow positions, with depths reaching up to 2 m throughout the winter and spring months (blue and green lines in Figure 3.3.4.1. V). During the spring season, the sandbars remained situated offshore at both locations (green lines in Figure 3.3.4.1. V). Sandbar migrated onshore in summer, attaining depths of 0.5 m in the north, while maintaining a depth of 1 m in the southern section (red lines in Figure 3.3.4.1. V).

3.3.5. Alongshore variations

The migration cycles of sandbars and berms were examined for both the northern (in blue) and southern (in red) beach sections (Figure 3.3.5.1.) throughout the study period. The northern and southern zones were spatially delimited by aligning with the criteria of Ruiz de Alegría-Arzaburu et al. (2022), taking into consideration the similarity in shoreline and volume changes. In general, berms and sandbars exhibited distinct seasonality related to the incoming wave energy, but displayed significant alongshore variations within their cycles (Figure 3.3.5.1.). Furthermore, the proximity of the sandbar to the shoreline was found to be linked to the intertidal beach slope (Figure 3.3.5.1.b). Specifically, when intertidal slopes were steep, the sandbar remains offshore, but when slopes were gentler, it promoted the welding of the sandbar to the shoreline, consequently contributing to the recovery of the subaerial beach (Figure 3.3.5.1. b,c,d).

In the northern section, sandbars exhibited seasonal cycles; they migrated seaward during high-energy conditions (≥ 20 kWm^{-1}) reaching depths of up to 3.5-4 m (Figure 3.3.5.1. a,c). Conversely, sandbars displaced landwards during periods of low-energy (< 10 kWm^{-1}) to depths less than 1 m, eventually welding with the shoreline (Figure 3.3.5.1. a,c). On the other hand, sandbar migrations in the southern beach were less related with the amount of incoming wave energy, resulting in these features staying offshore for more extended durations at depths exceeding 2 m (Figure 3.3.5.1. a,d).

Berms disappeared faster in the north during high-energy conditions ($\geq$ 20 kWm^{-1}) (Figure 3.3.5.1. a,c) than in the south, where these features persisted a few months longer (Figure 3.3.5.1.d). The berm rebuilding process in the north was seasonal and depended on the proximity of the sandbar to the shoreline; it occurred when sandbars were located at depths < 1.5 m (Figure 3.3.5.1.c). In contrast, berms and sandbars co-existed in the south (Figure 3.3.5.1.d), and the reconstruction of the berm was less dependent of the sandbar proximity to the shoreline and rather reworked with existing intertidal sediment. In conclusion, berms lacked of seasonality and were quasi-permanent in the south (Figure 3.3.5.1.d).

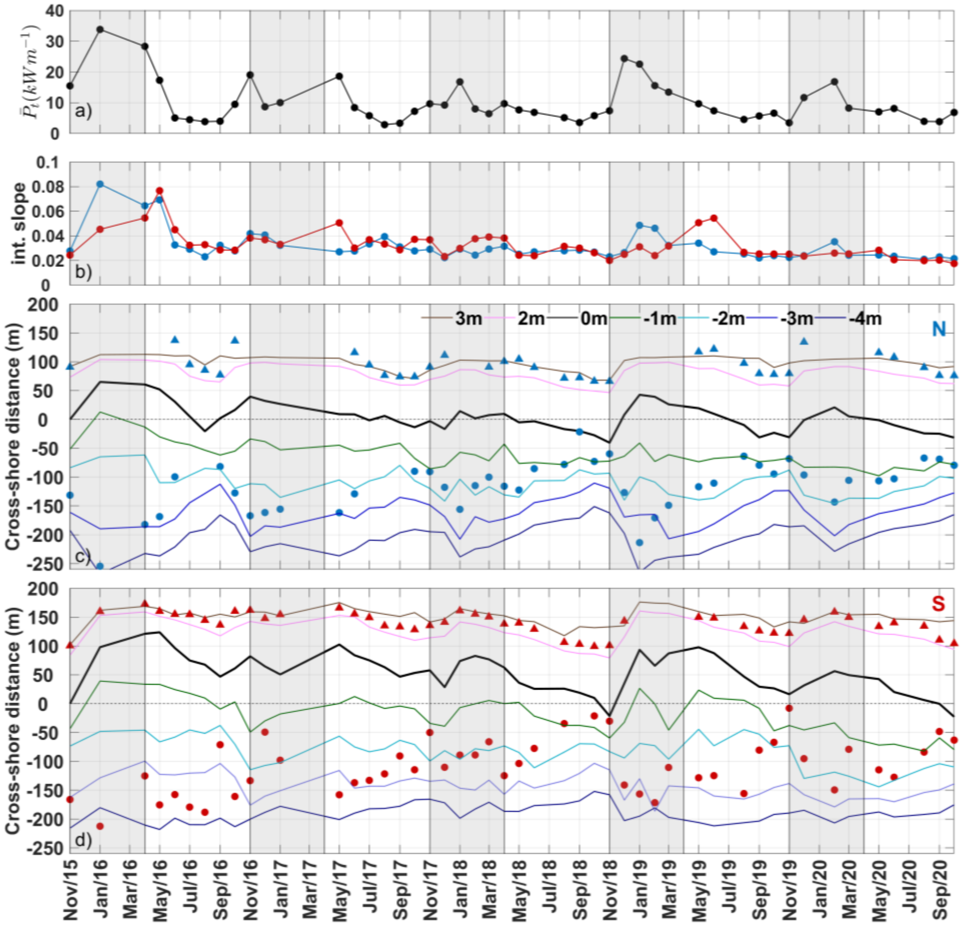

Figure 3.3.5.1. Time series from November 2015 to October 2020 of: (a) total wave power averaged over each survey period; (b) alongshore-averaged intertidal slope for the northern (blue line) and southern (red line) sections. Zone-averaged positions of the outer sandbar (dots) and berm (triangles) for the north (N) and south (S) are shown in blue (c) and red (d), respectively. The colored lines in (c) and (d) denote the mean topo-bathymetric contour lines. Cross-shore distances are referenced to the 0-m contour line (thick black line) from November 2015. The subaerial beach corresponds to the area above the 0-m isobath (positive distances), and the subtidal beach to the area below the 0-m isobath (negative distances). Increasing positive and negative cross-shore distances represent onshore berm/shoreline positions and offshore/deeper sandbar positions, respectively. Shaded boxes indicate periods of high-energy wave conditions.

Figura 3.3.5.1. Serie temporal de noviembre de 2015 a octubre de 2020 de: (a) potencia total del oleaje promediada para cada periodo de levantamiento; (b) pendiente intermareal promediada a lo largo de la costa para las secciones norte (línea azul) y sur (línea roja). Las posiciones promediadas por zona de la barra exterior (puntos) y la berma (triángulos) para el norte (N) y el sur (S) se muestran en azul (c) y rojo (d), respectivamente. Las líneas de colores en (c) y (d) representan las curvas de nivel topo-batimétricas medias. Las distancias en la dirección transversal a la costa están referidas a la curva de nivel de 0 m (línea negra gruesa) de noviembre de 2015. La playa subaérea corresponde al área por encima de la isóbata de 0 m (distancias positivas) y la playa submareal al área por debajo de dicha isóbata (distancias negativas). Distancias transversales positivas y negativas crecientes representan posiciones hacia tierra y a mar adentro, respectivamente. Las áreas sombreadas indican periodos de alta energía del oleaje.

3.3.6. Near-surfzone wave and flow variations along the beach

We used sixteen days of wave and flow measurements collected between September and October to represent both low-energy and mid-to-high energy conditions on the beach. September was chosen as it is typically a low-energy month, ideal for safely installing nearshore instrumentation. Fortunately, during the period from late September to October, we experienced higher-energy conditions, allowing us to assess alongshore flow variations for both low-energy (H_s < 1m) conditions, characteristic of summer and fall, and mid-to-high energy (H_s 1 to 2.3 m) conditions, typical of spring and mild winters (see Figure 3.3.1.1.). The time-series data for near-surfzone measurements was constrained by the capacity of the batteries, and both instruments were situated at alongshore locations that exhibited different morphological variations over time (Figure 3.3.2.1.).

The southern beach experienced higher-energy incident waves from a quasi-normal direction, in contrast to the northern beach (Figure 3.3.6.1. a and b). During energetic wave conditions (H_s > 1.5 m), the southern beach (S) exhibited relatively stronger net offshore flows, reaching speeds of up to -0.2 ms^{-1}, with offshore flows prevailing over onshore flows in general (Figures 3.3.6.1. c). Conversely, the northern beach (N) presented stronger net onshore flows, reaching 0.1 ms^{-1}, particularly during specific lower-energy periods (H_s < 1.2 m) characterized by oblique wave incidence (Figure 3.3.6.1. b and d). Alongshore flows exhibited semi-diurnal directional changes, shifting upcoast (northward) and downcoast (southward), except during higher-energy periods when flows were persistently downcoast and offshore. Notably, these downcoast and offshore (southwesterly) flows were stronger in the southern beach compared to the north, reaching speeds of up to -0.4 ms^{-1} and -0.2 ms^{-1}, respectively (Figure 3.3.6.1. e and f).

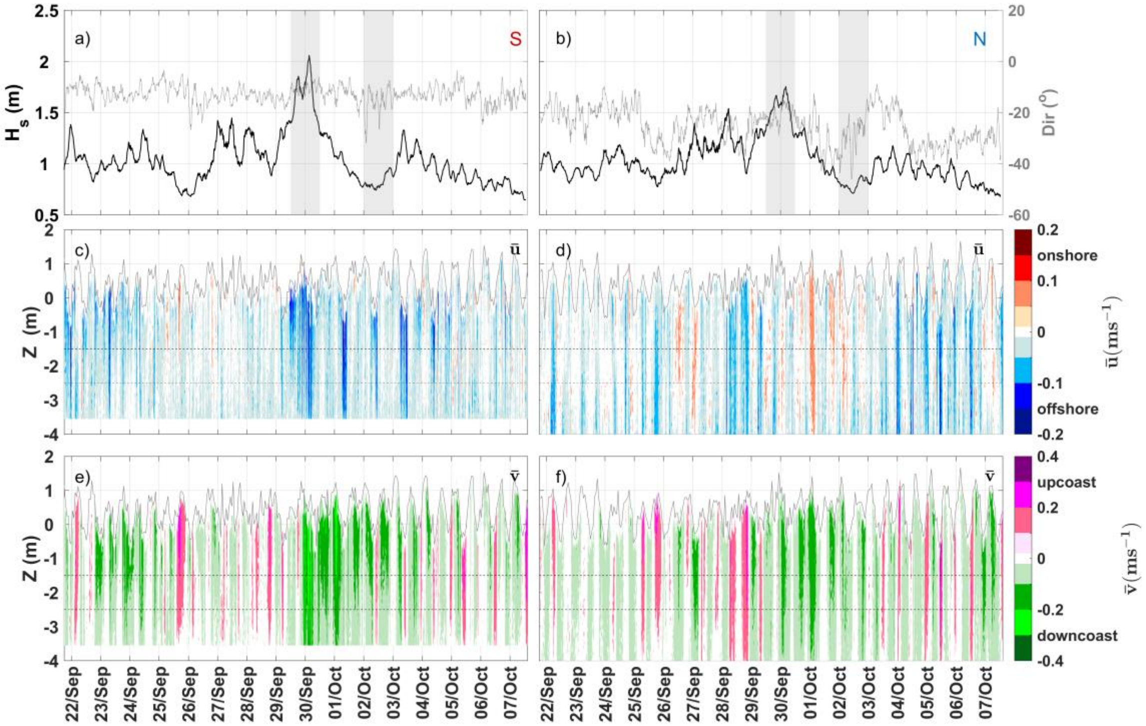

Figure 3.3.6.1 Time-series of: (a, b) significant wave height (H_s) and wave direction (Dir); (c, d) cross-shore and (e, f) alongshore bin-averaged flows over 17 min (1024 s) for the south and north (S and N), respectively. The shadowed sections highlight high-energy and low-energy periods in (a) and (b), and the horizontal dashed lines in (c, d, e, f) denote the mid water column layer where wave velocity skewness was computed. The upcoast and downcoast flow directions align roughly with northward and southward orientations.

Figura 3.3.6.2 Serie temporal de: (a, b) altura significativa del oleaje (Hs) y dirección del oleaje (Dir); (c, d) componentes de corriente promedio por bin en la dirección transversal a la costa (cross-shore) y (e, f) en la dirección paralela a la costa (alongshore), promediadas en intervalos de 17 minutos (1024 s) para las zonas sur y norte (S y N), respectivamente. Las secciones sombreadas en (a) y (b) indican los periodos de alta y baja energía, y las líneas horizontales punteadas en (c, d, e, f) marcan la capa media de la columna de agua donde se calculó la asimetría de la velocidad del oleaje (wave velocity skewness). Las direcciones de flujo hacia arriba y hacia abajo de la costa se alinean aproximadamente con orientaciones hacia el norte y hacia el sur, respectivamente.

We selected a middle layer situated at depths ranging from 1.5 and 2.5 m (see horizontal dashed lines in Figure 3.3.6.1.c, d, e, f) for the computation of wave velocity skewness (Sk) variations, and the assessment of net cross-shore flows over the time (Figure 3.3.6.2.). This specific layer was chosen to capture the maximum offshore flow and enable the comparison of the counteracting skewness at this same depth level. Skewness calculations were performed for both the cross-shore (Figure 3.3.6.2.f) and alongshore (Figure 3.3.6.2.g) components to comprehensively evaluate their effect under oblique wave conditions. The northern beach presented significantly higher total Sk values compared to the southern beach (Figure 3.3.6.2.f, g). Cross-shore Sk was slightly larger in the southern beach compared to the north. In contrast, the alongshore Sk was much larger in the north, particularly during periods of mid-energy waves ($1 < H_s < 1.5$ m) characterized by incident angles of up to 30 degrees (Figure 3.3.6.2.).

In general, net offshore flows were more intense in the southern beach, reaching speeds of up to -0.2 ms^{-1}, whereas in the northern beach, they reached a maximum of -0.1 ms^{-1} (see shadowed zone for 30/Sep in Figure 3.3.6.2.d,e). The highest-intensity net offshore flows were observed in conjunction with the largest waves ($H_s > 1.5$ m; see shadowed areas for 30/Sep in Figure 3.3.6.2.) aligning with theoretical undertow calculations (see black lines in Figure 3.3.6.2.d,e), as per the Masselink and Black (1995) formula (Eq. 5). However, instances of intense offshore flows were also identified during low-tide and low-energy wave conditions

(H_s < 1 m) [1] (see shadowed zone for 02/Oct in Figure 3.3.6.2.d,e), particularly in the south, and possibly associated with the presence of rip-currents.

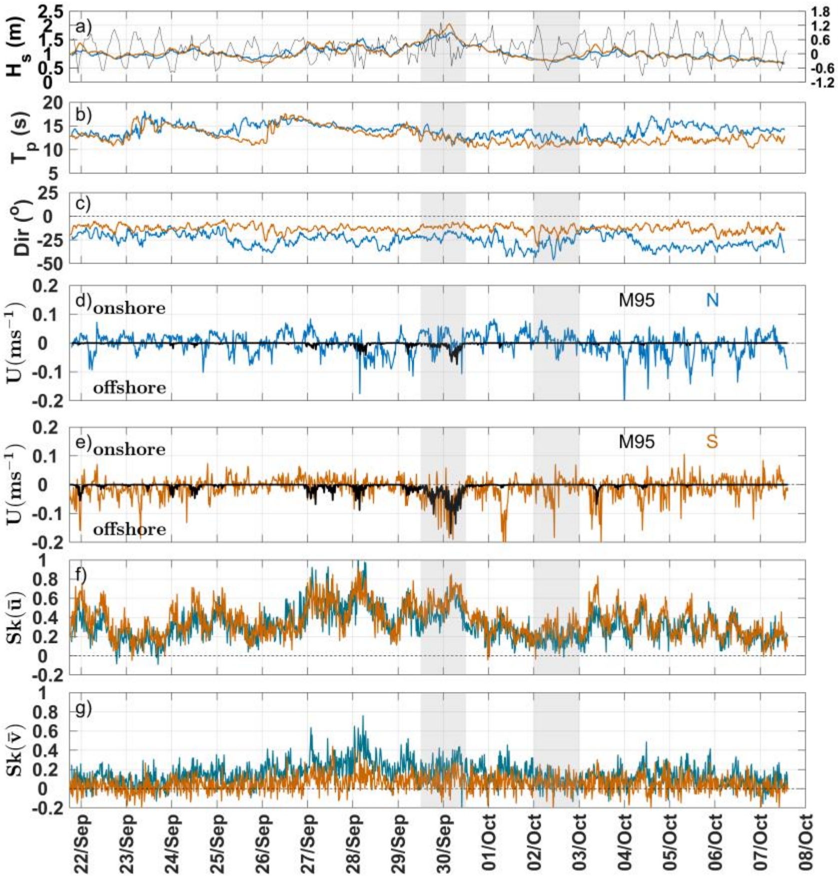

Figure 3.3.6.3 Time-series from 21st September to 7th October 2021 of two-hourly for N (blue) and S (orange): (a) significant wave height, H_s, and water-level (b) spectral peak wave period, T_p; and (c) wave direction relative to shoreline position (Dir) for the north (blue) and south (orange). Panels (d) and (e) present depth-averaged and time-averaged (17-min bursts) cross-shore flows for the middle layer for N and S, and compared to theoretical undertow calculations (black line; MB 95 formula). Cross-shore and alongshore wave velocity skewness components, Sk(u) and Sk(v) are presented in the bottom panels (f) and (g) respectively. The shadowed sections highlight a period of high-energy in 30/Sep and of low-energy in 02/Oct.

Figura 3.3.6.2. Series temporales desde el 21 de septiembre hasta el 7 de octubre de 2021 con datos cada dos horas para el norte (azul) y sur (naranja): (a) altura significativa del oleaje, Hs, y nivel del agua; (b) período pico espectral del oleaje, Tp; y (c) dirección del oleaje relativa a la posición de la línea de costa (Dir) para el norte (azul) y sur (naranja). Los paneles (d) y (e) muestran los flujos transversales promediados en profundidad y en el tiempo (ráfagas de 17 min) para la capa media en el norte y sur, comparados con los cálculos teóricos de resaca (línea negra; fórmula MB 95). Los componentes de asimetría de la velocidad del oleaje en dirección transversal y longitudinal, Sk(u) y Sk(v), se muestran en los paneles inferiores (f) y (g), respectivamente. Las secciones sombreadas destacan un período de alta energía el 30 de septiembre y de baja energía el 2 de octubre.

3.4. Discussion

This study presents new insights into the morphodynamics of sandbar and berm cross-shore cycles, with a focus on their alongshore variability in relation to incident wave characteristic and near-surfzone flow fluctuations. At La Misión beach, sandbars migrated onshore during low-energy waves, merging with the shoreline and becoming intertidal sandbars, thereby contributing to the berm rebuilding process, as observed in other sites (Komar, 1974; Jensen et al., 2009; Vidal-Ruiz and Ruiz de Alegría-Arzaburu, 2020). While morphological variations at the field site were previously attributed to seasonal wave changes (Ruiz de Alegría-Arzaburu et al., 2022), there remained a need for a better understanding of alongshore shoreface and foreshore sand exchanges.

Our study revealed that morphological variations in the southern beach exhibited larger shoreline retreats (100-130 m) and longer recovery periods, lasting for several years, in contrast to the northern beach (50-80 m with seasonal recoveries) (see black contour lines in Figure 3.3.5.1. c,d). These disparities were primarily linked to the delayed onshore migration of sandbars in the south, which could only merge with the shoreline during extended periods of low-energy waves. This reluctance to migrate onshore was attributed to the prevalence of more intense net near-surfzone offshore flows (up to -0.2 ms^{-1}) in the south, as opposed to the north, where larger skewness, weaker offshore flows (up to -0.1 ms^{-1}) and more oblique wave incidence prevailed. Consequently, variations in incident wave angles were identified as a critical factor influencing flow characteristics, sediment transport, and sandbar migration patterns (Price et al., 2014). At La Misión, the most energetic net offshore flows occurred during largest waves (H_s > 1.5 m), aligning with theoretical undertow current calculations (Masselink and Black, 1995). Nevertheless, we also observed robust offshore flows during low-tide and lower-energy conditions (Hs < 1 m), indicating their potential association with rip currents (Castelle et al., 2016).

High near-bed wave velocity skewness values are typically linked to the prevalence of net onshore sediment transport and quicker subaerial beach recovery capabilities (Hsu et al., 2006; Ruessink et al., 2007; Fernández-Mora et al., 2015; Grossmann et al., 2023). The measured near-bed wave velocity skewness values were greater in the north (1.3) compared to the south (0.9), indicating relatively larger onshore sediment transport in the northern beach. These findings align with previously reported values of up to 1.5 for Duck, USA (Elgar et al., 2001), 1.2 for Terschelling and Egmond aan Zee, The Netherlands (Elfrink et al., 2006) and 0.8 for different beaches in southwestern UK (Mariño-Tapia et al., 2007). Furthermore, net flows in the northern beach were predominantly onshore, except for high-energy waves (H_s > 1.5 m) and specific low-energy conditions during low-tide. Therefore, the dominant net onshore flows affected by the higher wave velocity skewness values contributed to the seasonal migration of sandbars towards the shore and the beach recovery processes (Mariño-Tapia et al., 2007; Grossmann et al., 2023). In the north, prevalence of landward-skewed flows during the spring led to the merging of sandbars with the shoreline, resulting in a typically barless beach during the summer months.

At La Misión, the primary mechanism driving berm development, as described by Hine in 1979, was the landward migration and merging of sandbars with the beach face. Significant variations were observed along the shoreline in terms of berm erosion and rebuilding processes. In the northern beach, the berm underwent a seasonal cycle of erosion and rebuilding closely tied to incoming wave energy and the cross-shore sediment transport facilitated by sandbar displacements (e.g. Weir et al., 2006). It completely eroded during the winter months, and gradually rebuilt during periods of low-energy conditions between summer and fall, mirroring a process similar to that observed at Avoca Beach (Weir et al., 2006) and Narrabeen Beach (Phillips et al., 2019) in Australia. In contrast, in the southern beach, the berm rebuilding process displayed less reliance on incoming wave conditions. The berms tended to persist over the years, experiencing partial erosion during mid-energy winters and subsequent rebuilding, particularly when sandbars were present.

During the berm rebuilding process, the beach face exhibited distinct patterns, it prograded (grew seaward) more in the southern beach than in the north (see an example in Figure 3.3.3.1. III). These variations, as documented by Dubois (1988), were primarily influenced by the beach face slope, resulting in differences in swash exceedance relative to the berm crest elevation (Katoh and

Yanagishima, 1992; Weir et al., 2006; Austin and Masselink, 2006; Baldock et al., 2008). Berm crest positions displayed relative stability, with positions ranging from 40 to 60 m in the north and 25 to 95 m in the south. Overall, the northern and southern beach featured similar averaged mild intertidal slopes ($\tan\beta$ = 0.03). However, as the slopes became steeper, it caused the sandbar to remain offshore. Conversely, when the slopes were gentler, it facilitated the welding of the sandbar to the shoreline, thereby contributing to the berm recovery, as observed by Jensen et al., (2009). Moreover, more extended swash zone or wider intertidal beach is suggested to contribute to the stability of the berm in the south, related to the higher sediment availability.

The findings of this study suggest that, despite significant seasonal fluctuations, the beach typically reverts to its initial state in late summer or early fall, except during El Niño years. Additionally, the observed morphological variations along the beach can be attributed to the morphodynamic feedback with sandbars affecting hydrodynamics, particularly in terms of near-bed wave skewness and near-surfzone flow variations. These hydrodynamic variations, in turn, influence sediment transport and the morphological evolution of the beach.

3.5. Conclusions

This study analyzed alongshore differences in sandbar and berm migration cycles at La Misión beach, Baja California, based on morphological and hydrodynamic measurements collected over a 5-year period (2015-2020). We obtained the following conclusions:

- The movement and merging of nearshore sandbars with the shoreline during low-energy wave conditions, and their contribution to the rebuilding of the berm, are significantly affected by the wave skewness and near-surfzone flow variations, which differ between the northern and southern sections of the beach.
- In the north, larger near-bed wave velocity skewness and predominantly onshore net flows resulted in smaller shoreline retreats and allowed for seasonal recoveries through the welding of outer sandbars to the intertidal beach over the spring and summer.
- In the south, comparatively smaller near-bed wave skewness and relatively more intense net offshore flows induced larger shoreline retreats and longer recovery times, as outer sandbars were unable to weld the intertidal beach over the spring and summer and remained offshore most of the time.
- The erosion and rebuilding of the berm differed alongshore and were determined by wave energy and sandbar location relative to the shoreline and intertidal beach slope. The berm in the north underwent seasonal erosion and vertical growth with milder intertidal slopes while the southern berm was more persistent with steeper intertidal slopes and a seaward growth pattern that was less dependent on wave energy.

Further research is necessary to deepen our knowledge of sandbar and berm cycles on these types of beaches, particularly in light of potential disruptions caused by climate change and sea-level rise. It is essential to continue investigating how these environmental factors will affect the behavior of nearshore sandbars, as well as the erosion and rebuilding processes of the berm. Understanding these changes will be critical in developing effective management strategies for these coastal areas and ensuring their long-term sustainability.

References

Anthony, E. J., & Aagaard, T. (2020). The lower shoreface: Morphodynamics and sediment connectivity with the upper shoreface and beach. Earth-Science Reviews, 210, 103334. https://doi.org/https://doi.org/10.1016/j.earscirev.2020.103334

Austin, M. J., & Masselink, G. (2006). Observations of morphological change and sediment transport on a steep gravel beach. Marine Geology, 229(1), 59–77. https://doi.org/https://doi.org/10.1016/j.margeo.2006.02.003

Baldock, T. E., Weir, F., & Hughes, M. G. (2008). Morphodynamic evolution of a coastal lagoon entrance during swash overwash. Geomorphology, 95(3), 398–411. https://doi.org/https://doi.org/10.1016/j.geomorph.2007.07.001

Castelle, B., Scott, T., Brander, R. W., & McCarroll, R. J. (2016). Rip current types, circulation and hazard. Earth-Science Reviews, 163, 1–21. https://doi.org/https://doi.org/10.1016/j.earscirev.2016.09.008

Dubois, R. N. (1988). Seasonal changes in beach topography and beach volume in Delaware. Marine Geology, 81(1), 79–96. https://doi.org/https://doi.org/10.1016/0025-3227(88)90019-9

Elfrink, B., Hanes, D. M., & Ruessink, B. G. (2006). Parameterization and simulation of near bed orbital velocities under irregular waves in shallow water. Coastal Engineering, 53(11), 915–927. https://doi.org/10.1016/j.coastaleng.2006.06.002

Elgar, S., Gallagher, E. L., & Guza, R. T. (2001). Nearshore sandbar migration. Journal of Geophysical Research: Oceans, 106(C6), 11623–11627. https://doi.org/10.1029/2000jc000389

Fernández-Mora, A., Calvete, D., Falqués, A., & de Swart, H. E. (2015). Onshore sandbar migration in the surf zone: New insights into the wave-induced sediment transport mechanisms. Geophysical Research Letters, 42(8), 2869–2877. https://doi.org/https://doi.org/10.1002/2014GL063004

Grossmann, F., Hurther, D., van der Zanden, J., Sánchez-Arcilla, A., & Alsina, J. M. (2023). Near-Bed Sediment Transport Processes During Onshore Bar Migration in Large-Scale Experiments: Comparison With Offshore Bar Migration. Journal of Geophysical Research: Oceans, 128(3), e2022JC018998. https://doi.org/https://doi.org/10.1029/2022JC018998

Hine, A. C. (1979). Mechanisms of berm development and resulting beach growth along a barrier spit complex. Sedimentology, 26(3), 333–351. https://doi.org/https://doi.org/10.1111/j.1365-3091.1979.tb00913.x

Hsu, T.-W., Tseng, I.-F., & Lee, C.-P. (2006). A New Shape Function for Bar-Type Beach Profiles. Journal of Coastal Research, 22(3 (223)), 728–736. https://doi.org/10.2112/04-0340.1

Jensen, S. G., Aagaard, T., Baldock, T. E., Kroon, A., & Hughes, M. (2009). Berm formation and dynamics on a gently sloping beach; the effect of water level and swash overtopping. Earth Surface Processes and Landforms, 34(11), 1533–1546. https://doi.org/https://doi.org/10.1002/esp.1845

Katoh, K., & Yanagishima, S. (1992). Berm Formation and Berm Erosion. In Coastal Engineering (pp. 2136–2149). https://doi.org/10.1061/9780872629332.163

King, C. A. M. (1959). Beaches and coasts: London. Edward Arnold Ltd, 403pp.

Komar, P.D., (1974). Beach Processes and Sedimentation (429 pp). Prentice-Hall, Englewood Cliffs, NJ.

Mariño-Tapia, I., Russell, P. E., O’Hare, T. J., Davidson, M. A., & Huntley, D. A. (2007). Cross-shore sediment transport on natural beaches and its relation to sandbar migration patterns: 1. Field observations and derivation of a transport parameterization. Journal of Geophysical Research: Oceans, 112(C3). https://doi.org/https://doi.org/10.1029/2005JC002893

Mariño-Tapia, I., Russell, P.E., O'Hare, T.J., Davidson, M.A., Saulter, A.N., Miles, J.M., and Huntley, D.A. (2001). Relationship between vertical wave asymmetry and the fourth velocity moment in the surf zone: implications for sediment transport, In: B.L. Edge and J.M. Hemsley (eds), Proceedings of the Fourth International Symposium Waves 2001 (San Francisco), American Society of Civil Engineers, Virginia, USA, 1295-1305.

Masselink, G., & Black, K. P. (1995). Magnitude and cross-shore distribution of bed return flow measured on natural beaches. Coastal Engineering, 25(3), 165–190. https://doi.org/https://doi.org/10.1016/0378-3839(95)00002-S

Masselink, G., & Hughes, M. G. (2003). Introduction to coastal processes and geomorphology (1st ed.). London, UK: Hodder Arnold.

Morton, R. A., Paine, J. G., & Gibeaut, J. C. (1994). Stages and durations of post-storm beach recovery, southeastern Texas Coast, U.S.A. Journal of Coastal Research, 10(4), 884– 908. https://doi.org/10.2307/4298283

Pedersen, T., Lohrmann, A., Krogstad, H.E. (2005). Wave measurements from a subsurface platform. Proceedings WAVES 2005, Madrid, Spain.

Phillips, M. S., Blenkinsopp, C. E., Splinter, K. D., Harley, M. D., & Turner, I. L. (2019). Modes of Berm and Beachface Recovery Following Storm Reset: Observations Using a Continuously Scanning Lidar. Journal of Geophysical Research: Earth Surface, 124(3), 720–736. https://doi.org/https://doi.org/10.1029/2018JF004895

Price, T. D., Ruessink, B. G., & Castelle, B. (2014). Morphological coupling in multiple sandbar systems – a review. Earth Surface Dynamics, 2(1), 309–321. https://doi.org/10.5194/esurf-2-309-2014

Puleo, J. A., & Torres-Freyermuth, A. (2016). The second international workshop on swash-zone processes. Coastal Engineering, 115, 1–7. https://doi.org/https://doi.org/10.1016/j.coastaleng.2015.09.007

Ruessink, B. G., Kuriyama, Y., Reniers, A. J. H. M., Roelvink, J. A., & Walstra, D. J. R. (2007). Modeling cross-shore sandbar behavior on the timescale of weeks. Journal of Geophysical Research: Earth Surface, 112(F3). https://doi.org/https://doi.org/10.1029/2006JF000730

Ruiz de Alegría-Arzaburu, A., Gracia-Barrera, A. D., Kono-Martínez, T., & Coco, G. (2022). Subaerial and upper-shoreface morphodynamics of a highly-dynamic enclosed beach in NW Baja California. Geomorphology, 413, 108336. https://doi.org/https://doi.org/10.1016/j.geomorph.2022.108336

Ruiz de Alegría-Arzaburu, A., Vidal-Ruiz, J. A., García-Nava, H., & Romero-Arteaga, A. (2017). Seasonal morphodynamics of the subaerial and subtidal sections of an intermediate and mesotidal beach. Geomorphology, 295, 383–392. https://doi.org/https://doi.org/10.1016/j.geomorph.2017.07.021

Russell, P. E., Masselink, G., Blenkinsopp, C., & Turner, I. L. (2009). A Comparison of Berm Accretion in the Swash Zone on Sand and Gravel Beaches at the Timescale of Individual Waves. Journal of Coastal Research, 1791–1795. http://www.jstor.org/stable/25738098

Shepard, F.P. (1950). Beach cycles in southern California. In: Beach Erosion Board (Technical Memo 20). US Army Corps of Engineering, Washington DC.

Sunamura, T. (1989). Chapter 6 Sandy Beach Geomorphology Elucidated by Laboratory Modeling. In V. C. Lakhan & A. S. Trenhaile (Eds.), Elsevier Oceanography Series (Vol. 49, pp. 159–213). Elsevier. https://doi.org/https://doi.org/10.1016/S0422-9894(08)70126-0

Vidal-Ruiz, J. A., & Ruiz de Alegría-Arzaburu, A. (2019). Variability of sandbar morphometrics over three seasonal cycles on a single-barred beach.

Geomorphology, 333, 61–72. https://doi.org/10.1016/j.geomorph.2019.02.034

Vidal-Ruiz, J. A., & Ruiz de Alegría-Arzaburu, A. (2020). Modes of onshore sandbar migration at a single-barred and swell-dominated beach. Marine Geology, 426(November 2019), 106222. https://doi.org/10.1016/j.margeo.2020.106222

Weir, F. M., Hughes, M. G., & Baldock, T. E. (2006). Beach face and berm morphodynamics fronting a coastal lagoon. Geomorphology, 82(3), 331–346. https://doi.org/https://doi.org/10.1016/j.geomorph.2006.05.015

CHAPTER 4. Characterizing nearshore circulation on a highly dynamic beach under varying morphological configurations

Abstract

This chapter examines circulation patterns at La Misión Beach using the XBeach model in Surfbeat mode, to assess how alongshore morphological differences influence nearshore currents. Model validation using near-surf zone measurements led to key adjustments, including a 1.5% reduction in the tidal signal and the implementation of a spatially varying directional wave spectrum. These adjustments improved the simulation of nearshore currents and wave directionality. Wave directionality was a key factor of mean flow patterns in the surfzone. Southwesterly waves generated northward (upcoast) flows, with peak velocities up to 1 m/s observed in the southern beach, where a deflected rip current developed. In contrast, northwesterly waves induced southward (downcoast) flows, also reaching up to 1 m/s in the northern section. Westerly shore-normal waves primarily drove offshore-directed flows, strongest in the south at around 0.6 m/s. Seasonal nearshore circulation patterns were primarily defined by incoming wave characteristics and the configuration of nearshore morphology. During summer and fall, alongshore-uniform northward mean flows of up to 0.4 m/s in the surf zone prevailed, with peak velocities (0.8 m/s) near the southern and northern rocky outcrops. In winter, prominent sandbars located at 2 to 3 m depth induced offshore-directed mean currents extending to 4 m depth, disrupting alongshore flows. In spring, channels cut through sandbars produced mean rip currents of up to 0.4 m/s, with the strongest flows again near the southern and northern boundaries. These results suggest dynamic interactions between alongshore currents across the beach, with flow direction shifting between northward and southward in response to a combination of offshore wave approach angles, tidal forcing, and cross-shore flows beyond the surf zone. Alongshore variations in cross-shore velocity skewness revealed negative trends in the southern section and positive trends in the central and northern sections. In spring, sandbar gaps significantly influence alongshore velocity skewness variations, reflecting the role of cross-shore flows through these features. These findings highlight the critical role of nearshore morphology in driving variations in alongshore flows at La Misión beach.

Este capítulo examina los patrones de circulación en la playa La Misión utilizando el modelo XBeach en modo *Surfbeat*, para evaluar cómo las diferencias morfológicas a lo largo de la costa influyen en las corrientes cercanas a la orilla. La validación del modelo con mediciones cercana a la rompiente condujo a ajustes clave, incluyendo una reducción del 1.5 % en la señal de marea y la implementación de un espectro direccional de oleaje con variación espacial. Estos ajustes mejoraron la simulación de las corrientes cercanas a la orilla y la direccionalidad del oleaje. La direccionalidad del oleaje fue un factor clave en los patrones de flujo medio en la zona de rompiente. El oleaje proveniente del suroeste generaró flujos hacia el norte (contracorriente), con velocidades máximas de hasta 1 m/s observadas en la playa sur, donde se desarrolló una corriente de retorno desviada. En contraste, el oleaje del noroeste indujo flujos hacia el sur (a favor de la costa), también alcanzando hasta 1 m/s en la sección norte. El oleaje perpendicular a la costa proveniente del oeste impulsó principalmente flujos dirigidos hacia mar adentro, siendo más intensos en el sur, aproximadamente 0.6 m/s. La circulación estacional cercana a la costa se define principalmente por las características del oleaje entrante y la configuración morfológica cercana a la orilla. En verano y otoño, prevalecieron flujos medios uniformes hacia el norte de hasta 0.4 m/s en la zona de rompiente, con velocidades máximas (0.8 m/s) cerca de los afloramientos rocosos del sur y norte. En invierno, barras de arena a profundidades de 2 a 3 m indujeron corrientes medias dirigidas hacia mar adentro, que se extendieron hasta 4 m de profundidad, interrumpiendo los flujos a lo largo de la costa. En primavera, los canales cortados a través de las barras de arena produjeron corrientes medias de resaca de hasta 0.4 m/s, con los flujos más intensos cerca de los límites sur y norte. Estos resultados sugieren interacciones dinámicas entre las corrientes a lo largo de la costa, con cambios en la dirección del flujo entre norte y sur en respuesta a una combinación de ángulos de aproximación del oleaje, forzamiento mareal y flujos transversales más allá de la zona de rompiente. Las variaciones a lo largo de la costa en la asimetría de la velocidad transversal revelaron tendencias negativas en la sección sur y positivas en las secciones central y norte. En primavera, las brechas en las barras de arena influyen significativamente en las variaciones de la asimetría de la velocidad a lo largo de la costa, reflejando el papel de los flujos transversales. Se resalta el papel crítico de la morfología cercana a la orilla en las variaciones de los flujos a lo largo de la costa en la playa La Misión.

4.1. Introduction

Nearshore circulation patterns are strongly influenced by seasonal variations in beach morphology and wave energy incidence. Under high-energy wave conditions ($H_s > 2.5$ m), beaches typically exhibit dissipative states, characterized by wide surf zones and multiple wave-breaking points (Wright and Short, 1984). Strong wave action promotes offshore-directed flows, enhances sediment suspension, and increases seaward sediment transport, leading to the formation of offshore sandbars (Vidal-Ruiz and Ruiz de Alegria-Arzaburu et al., 2020) due to intense undertows (Masselink and Black, 1995; Kono-Martínez., et al 2023). As wave energy decreases, beaches transition to intermediate states, characterized by rhythmic sandbars and the formation of feeder currents that generate rip channels or rip cells (Wright et al., 1979; Aagaard et al., 1997).

When wave energy decreases ($H_s < 1$ m), beaches typically transition to a reflective state, characterized by steep foreshore gradients and narrow wave-breaking zones. In reflective states, nearshore circulation is primarily driven by wave swash and alongshore currents (Wright and Short, 1984), and rip currents become less frequent and weaker, allowing sediment to be transported back onshore, enhancing beach accretion and berm formation (Brander and Short, 2001). During transitional periods of moderate wave energy conditions (Hs = 1–2.5 m), typically in spring and fall, intermediate morphodynamic states emerge. These conditions often lead to the coexistence of berms and sandbars (Kono-Martínez et al., 2023), with nearshore circulation characterized by a combination of alongshore and cross-shore flows. The presence of both onshore-directed swash flows and weaker rip currents contribute to complex sediment redistribution patterns (Castelle et al., 2007).

Alongshore variations in wave energy and sediment transport play a critical role in shaping coastal morphology. These variations are primarily controlled by spatial differences in wave energy dissipation, wave breaking patterns, and offshore flow dynamics. Beach rotation events, for instance, result from shifts in the wave incidence angle, leading to differential sediment transport along the shore (Bryan et al., 2009; Yates et al., 2009). Another mechanism influencing alongshore variation is the presence of differential offshore-directed flows (e.g., undertow and rip currents), particularly in areas with discontinuous sandbars (Dudkowska et al., 2020).

On embayed beaches, nearshore circulation is further modulated by the interaction between wave forcing and the geometric confinement imposed by headlands (Mouragues et al., 2021). The size of the headland and the length of the embayment significantly affect wave energy distribution along the shore, influencing sediment transport pathways (Short and Masselink, 1999). Higher wave energy is typically observed near headlands, leading to spatial variability in alongshore transport processes that follow the dominant wave direction (Ojeda and Guillen, 2008; Castelle and Coco, 2012; Turki et al., 2013; Daly et al., 2014). The resulting hydrodynamic asymmetry often drives alongshore morphological changes through differential cross-shore processes. Additionally, variations in wave angle incidence can occur, which may be positive or negative relative to the shoreline. This variation, depending on the shape and size of the headland, contributes to the development of shadow zones (Mouragues et al., 2021) and influences variations in alongshore currents, ultimately leading to alongshore morphological changes.

Field measurements are essential for understanding the spatiotemporal variability of nearshore circulation and alongshore morphology in embayed beaches. However, obtaining high-resolution data across multiple hydrodynamic and morphological conditions remains a challenge. As a result, numerical models are often employed to complement field observations and analyze complex nearshore processes. The XBeach 2DH process-based model has been widely used for coastal studies, including storm-induced erosion assessments and harbor design (McCall et al., 2014). XBeach resolves hydrodynamic and morphodynamic processes within the shoaling and surf zones, reproducing mechanisms that govern beach dynamics at specific spatial scales (Kombiadou et al., 2021). Among other studies, Vousdoukas et al., (2011) analyzed alongshore morphological variations using XBeach to estimate offshore sandbar positions. Cohn and Ruggiero (2016) applied the XBeach model to investigate variations in alongshore runup and infragravity energy due to interannual morphological changes.

To better understand the differences in alongshore hydrodynamics between the southern and northern sections of La Misión beach, this chapter characterizes nearshore circulation under varying morphodynamic states using the XBeach model in Surfbeat mode, validated with in-situ measurements. Observations indicate that the southern beach tends to retain its offshore sandbar longer than the northern section, delaying subaerial beach recovery. This asymmetry has been attributed to stronger offshore-directed flows in the south; however, previous analyses were based on flow measurements collected over only a short, two-week period. To further investigate this phenomenon, this chapter examines the interplay between alongshore variations in wave forcing and current patterns across different wave energy conditions and beach morphological state. The objective is to identify the physical processes responsible for the contrasting patterns of sandbar migration and berm reconstruction observed in the southern and northern sections of the beach.

4.2. Methods

4.2.1. Model set-up

The surfbeat version of the XBeach process-based numerical model was applied to analyze nearshore circulation patterns under varying morphological and wave conditions at La Misión beach. Numerical simulations were performed on a grid spanning 3 km alongshore and 2 km cross-shore (Figure 2.4.1), with a resolution of 16 m in both alongshore and cross-shore directions for depths greater than 10 m. For shallower depths, the resolution was refined to 16 m alongshore and 4 m cross-shore. The model bathymetry was generated combining measured topographic and bathymetric data up to depths of 20 m. Bathymetry for deeper waters than 20 m was obtained from the GEBCO dataset (https://www.gebco.net/data_and_products/). The offshore boundary, positioned at a depth of 40 m, was initialized using wave measurements from an ADCP located at a depth of 20 m, adjusted to a JONSWAP spectrum (see Table II). Tidal forcing was applied using measured tidal data (Figure 4.2.2.1-4.2.2.3). Lateral boundaries were set as Neumann, while the offshore and landward boundaries were configured as 2D absorption conditions to minimize reflective wave effects. Each simulation ran for a period of 10 days, using a time step of 0.11 s, with a 12-hour spin-up period to allow the model to stabilize. Model outputs were recorded at 1 Hz at the nearshore ADCP location to carry out the model sensitivity analysis. Further details on the numerical approach and model configurations are available in Appendix A.

Table II. JONSWAP spectrum wave parameters used for simulations.

Tabla III. Parámetros de espectro de oleaje tipo JONSWAP usados para las simulaciones.

Parameter	Description	Unit	Values
Hm0	Spectral significant wave height	m	ADCP
Tp	Peak period	s	ADCP
mainang	Wave direction	degrees	ADCP
gammajsp	Peak enhancement factor of JONSWAP spectrum	-	3.3 (Default)
s	Wave spreading	degrees	ADCP
Duration	Duration of each condition	s	3600
dt	Time step	s	0.5 (Default)

4.2.2. Modeling scenarios

To investigate seasonal variations in circulation patterns, three morphological configurations were considered:

Reflective beach (summer-fall): The beach represents a welded sandbar and a partially developed berm (Figure 4.2.2.1 A and B). The bathymetry was measured on September 2021, and wave and tide boundary conditions span from September 21 to October 1, 2021 (Figure 4.2.2.1 D,E,F,G and H). During this period, H_s ranged between 1 and 1.7 m, with T_p varying from 12 to 16 s, with predominant southwesterly waves with occasional shore-normal incidence.

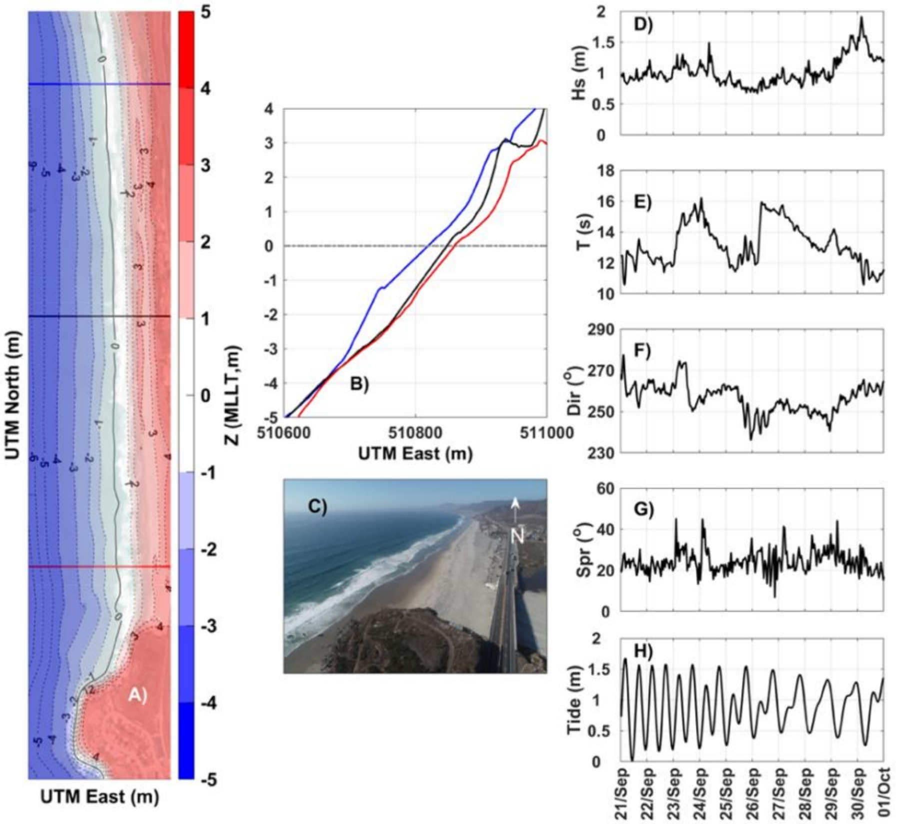

Figure 4.2.2.1. Digital elevation model for the summer-fall (September 2021; A). (B) Beach profiles for northern (blue), central (black) and southern (red) section. (C) Aerial view from southern section (September 21st,2021). Offshore boundary time series conditions include: (D) Significant wave height (Hs), (E) Wave period, (F) Wave direction, (G) Directional spreading and (H) Tide elevation (MLLT,m).

Figura 4.2.2.1 Modelo digital de elevación para verano-otoño (septiembre 2021; A). (B) Perfiles de playa para las secciones norte (azul), central (negro) y sur (rojo). (C) Vista aérea de la sección sur (21 de septiembre de 2021). Las series temporales de las condiciones en la frontera en mar abierto incluyen: (D) Altura significativa de ola (Hs), (E) Período de ola, (F) Dirección del oleaje, (G) Dispersión direccional y (H) Elevación de marea (MLLT, m).

Dissipative beach (winter): The beach presents an offshore sandbar at 2 m depth, in the absence of a berm (Figure 4.2.2.2 A and B). The bathymetry was measured in January 2018, and wave and tide data were from from January 14 to 24, 2018 (Figure 4.2.2.2 D,E,F,G and H). During this period, H_s ranged from 3 to 5 m with T_p varying between 10 and 18 s, predominantly from the southwest.

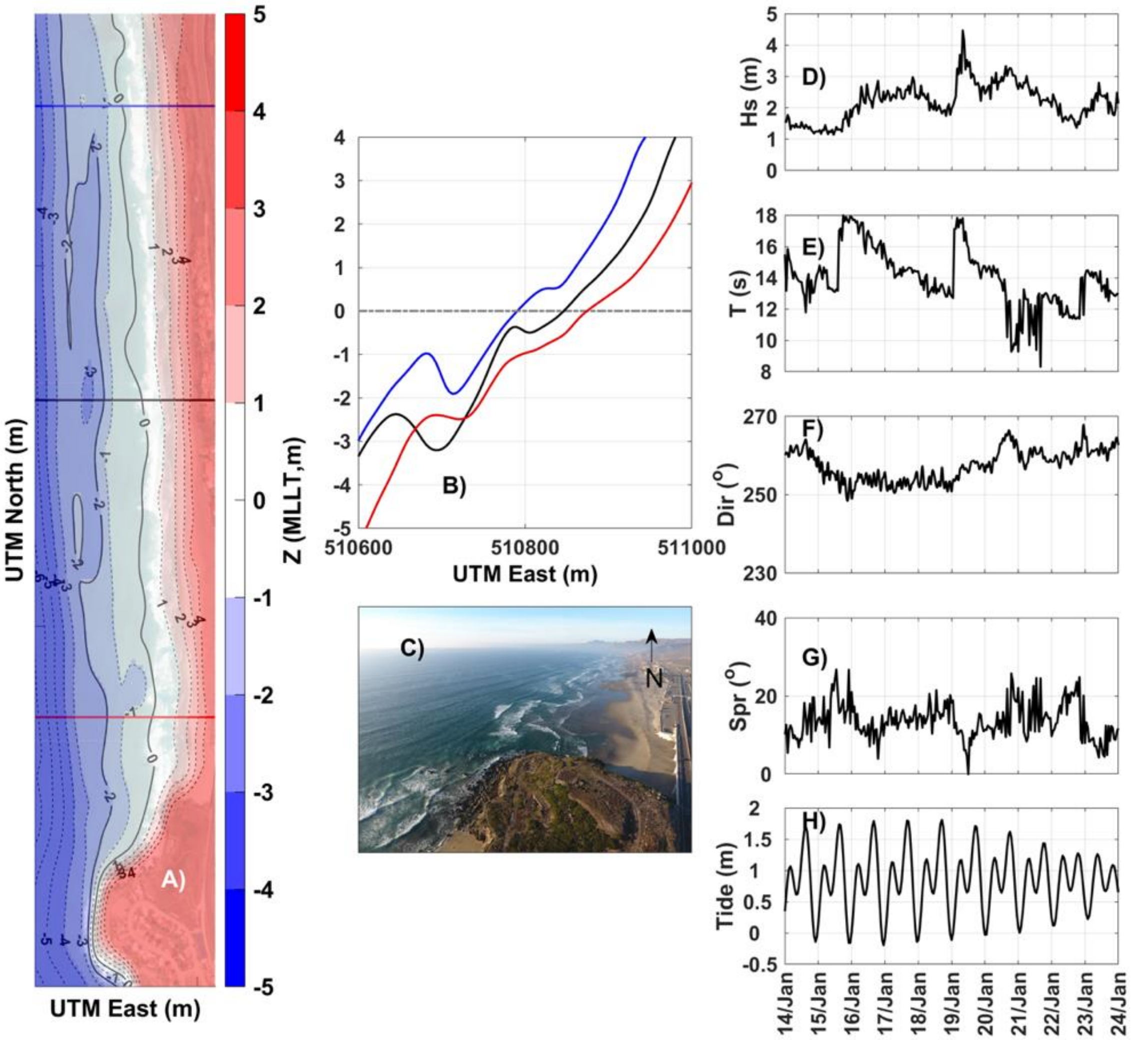

Figure 4.2.2.2 Digital elevation model for the winter (january 2018; A). (B) Beach profiles for northern (blue), central (black) and southern (red) section. (C) Aerial view from southern section (february 01st,2018). Offshore boundary time series conditions include: (D) Significant wave height (Hs), (E) Wave period, (F) Wave direction, (G) Directional spreading and (H) Tide elevation (MLLT,m).

Figura 4.2.2.2. Modelo digital de elevación para el invierno (enero 2018; A). (B) Perfiles de playa para las secciones norte (azul), central (negro) y sur (rojo). (C) Vista aérea de la sección sur (1 de febrero de 2018). Las series temporales de las condiciones en la frontera en mar abierto incluyen: (D) Altura significativa de ola (Hs), (E) Período de ola, (F) Dirección del oleaje, (G) Dispersión direccional y (H) Elevación de marea (MLLT, m).

Intermediate beach (spring): The beach features a sandbar at 2 m depth in the southern and central section, while it was absent in the north. The berm is partially developed in the central and northern beach, and absent in the south (Figure 4.2.2.3 A and B). Bathymetric data correspond to May 2018, and wave and tide conditions span from May 21 to 31, 2018 (Figure 4.2.2.3 D, E,F,G and H). During this period, H_s ranged from 1 to 2 m, T_p from 6 to 18 s, and waves were mostly shore-normal, with some influence from the southwest.

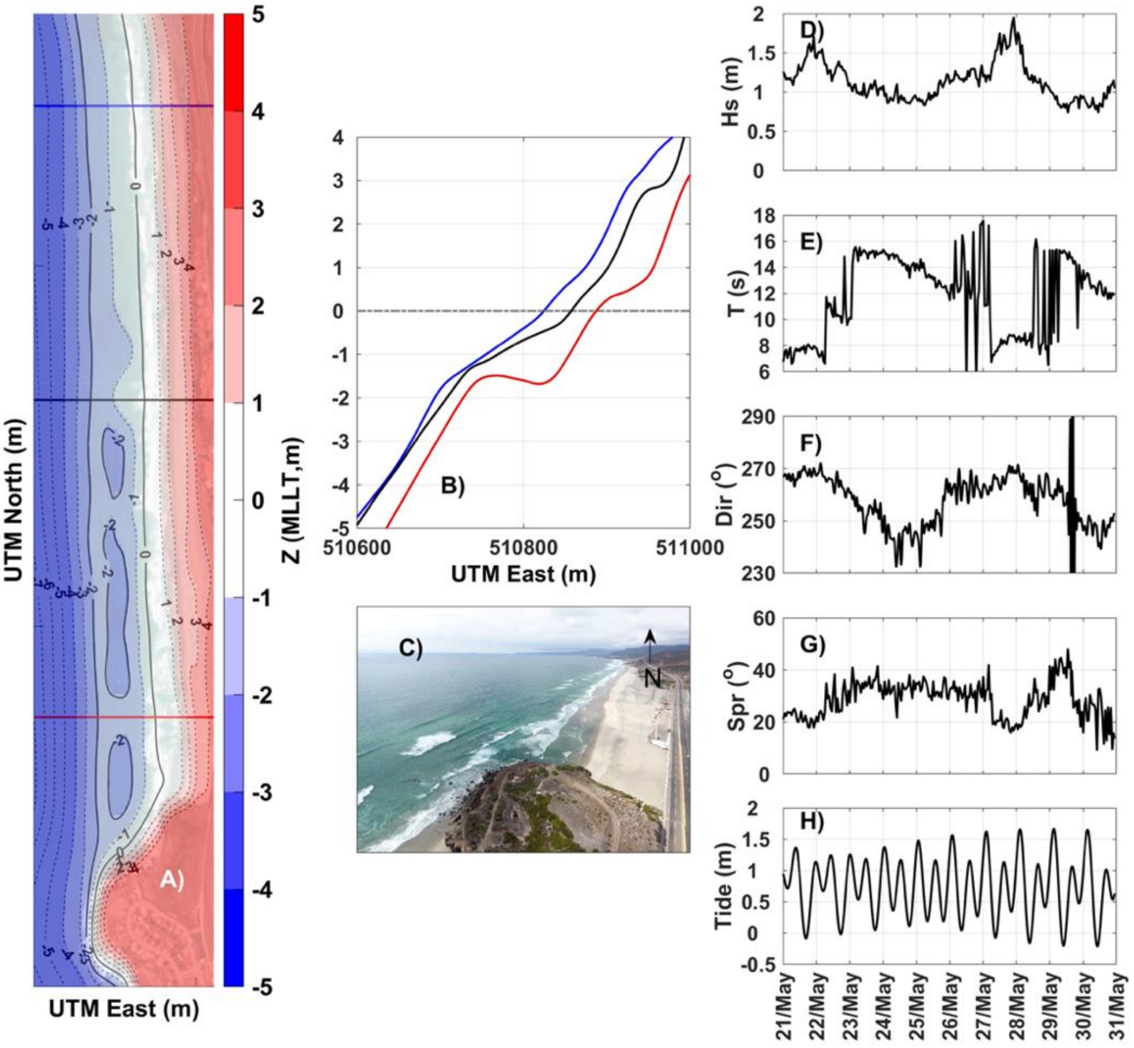

Figure 4.2.2.3. Digital elevation model for the spring (may 2018; A). (B) Beach profiles for northern (blue), central (black) and southern (red) section. (C) Aerial view from southern section (may 24th,2018). Offshore boundary time series conditions include: (D) Significant wave height (Hs), (E) Wave period, (F) Wave direction, (G) Directional spreading and (H) Tide elevation (MLLT,m).

Figura 4.2.2.3. Modelo digital de elevación para la primavera (mayo 2018; A). (B) Perfiles de playa para las secciones norte (azul), central (negro) y sur (rojo). (C) Vista aérea de la sección sur (24 de mayo de 2018). Las series temporales de las condiciones en la frontera en mar abierto incluyen: (D) Altura significativa de ola (Hs), (E) Período de ola, (F) Dirección del oleaje, (G) Dispersión direccional y (H) Elevación de marea (MLLT, m).

4.2.3. Model validation and sensitivity analysis

The XBeach model was validated using near-surf zone flow measurements collected from 21 September to 2 October, 2021. Topo-bathymetric surveys were conducted before and after the deployments (see Chapter 2 for additional details). Model outputs, including integral wave parameters (H_s, T_p, wave direction) and current components (east-west and north-south), were compared with measurements at the 4-m isobath. The model accuracy was evaluated with the Root Mean Square Error (RMSE), Bias and Cross Correlation Coefficient (R) (Eq. 8, 9 and 10).

$$RMSE = \sqrt{\frac{1}{n}\sum_{i=1}^{N}(x_{i\,XBeach} - x_{i\,observed})^2} \tag{8}$$

$$Bias = \frac{1}{n}\sum_{i=1}^{n}(XBeach_i - observed_i) \tag{9}$$

$$R_{XY} = \frac{1}{N}\sum_{I=1}^{N-\tau}(observed(i) - \overline{observed})(XBeach(i+\tau) - \overline{modeled}) \tag{10}$$

Sensitivity analyses were conducted with two primary tests (Table III):

1. *Alongshore Currents:* Evaluation of the model's ability to simulate alongshore current variations at different tidal stages. The parameter *tideloc* was modified from 2 to 4, to improve the reproduction of alongshore flows relative to the tidal stage. In addition, reductions to the tidal signal (by 5%, 2% and 1.5%) were tested in order to better represent the magnitude of flows.
2. *Wave Refraction*: Wave directionality changes were analyzed at the southern, central, and northern sections of the beach. The offshore

boundary *Nspectrumloc* parameter was adjusted to ensure modelling outputs were similar to measurements. Additionally, the surf zone for each simulation was determined by the equation of Battjes and Jansen (1978) (eq. 11):

$$H_{br} = \gamma * d \qquad (11)$$

where H_{br} is the height of breaking waves, γ is the breaking index (default value 0.78) and d is the local depth. The surfzone is defined as the region where the H_s reaches up to H_{br} in the cross-shore

Table IV. Test parameters modified for sensitivity analysis.

Tabla V. Parametros modificados para el análisis de sensibilidad.

Test/Parameter	**Description**	**Default**	**Modified**
tideloc	Tidal variation at boundary (1=offshore; 2 = offshore and land; 3 and 4 = all boundaries)	2	2,**4**
tidal signal	Time series of tidal elevation	-	5%,2%,**1.5%**
Nspectrumloc	Number of directional JONSWAP spectrum at boundary	1	1,6,**16**

4.3. Results

4.3.1. Sensitivity analysis

Modelled wave and flow results showed significant variations depending on the model setup. Initial simulations with default parameters showed moderate agreement (R > 0.4) with measured H_s and T_p in the southern and central beach sections, and poor (R < 0.4) in the northern beach, particularly in wave directionality and alongshore currents (Apendix C). To improve the representation of tidal currents, the tideloc parameter was adjusted from 2 to 4 based on Roelvink et al., (2010), but it did not enhance model accuracy (Appendix C). Instead, the reduction of the tidal signal (of 5%, %2 and 1.5%,) at the northern boundary yielded better results. Best model performance corresponded to a reduction of 1.5%, which enhanced alongshore current accuracy (R > 0.4). Then, the offshore boundary was divided into multiple segments, which significantly improved wave directionality results. The optimal configuration consisted of 16 segments, and the directional spectrum in the northern half was adjusted by subtracting 50 deg from the original offshore wave spectrum, while the southern half remained as the offshore wave spectrum. This setup resulted in the best agreement with observations based on RMSE, Bias, and cross correlation (R), making it the optimal model setup (Table IV and Figure 4.3.1.1 and 4.3.1.2).

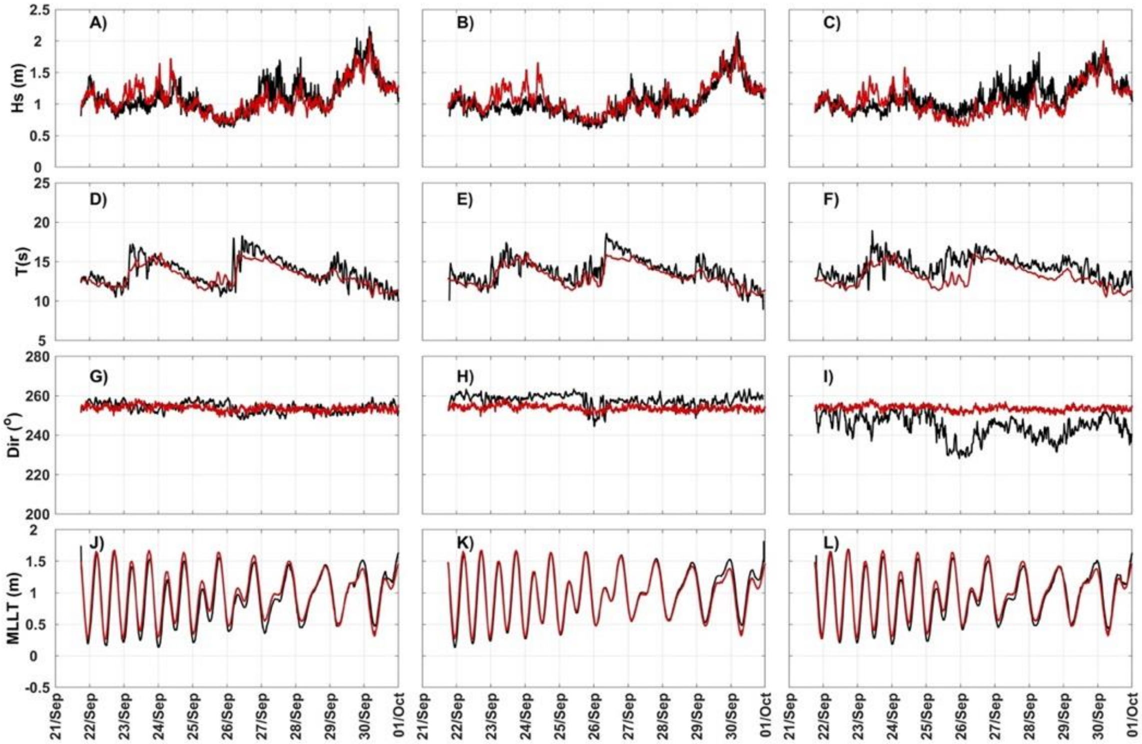

Figure 4.3.1.1. Modeled (red lines) vs measured (black lines) H_s, T_p, Dir and Tidal level (top to bottom) for the near-surfzone ADCPs in the South (A, D, G, J), Center (B, E, H, K) and North (C, F, I, L) using tideloc=4, 1.5% tidal reduction and nspectrum=: 16 (red) at the offshore boundary.

Figura 4.3.1.1. Modelado (líneas rojas) vs medido (líneas negras) de Hs, Tp, Dir y nivel de marea (de arriba hacia abajo) para los ADCPs de la zona cercana a la rompiente en el Sur (A, D, G, J), Centro (B, E, H, K) y Norte (C, F, I, L) usando tideloc=4, reducción de marea del 1.5% y nspectrum=16 (rojo) en la frontera mar adentro.

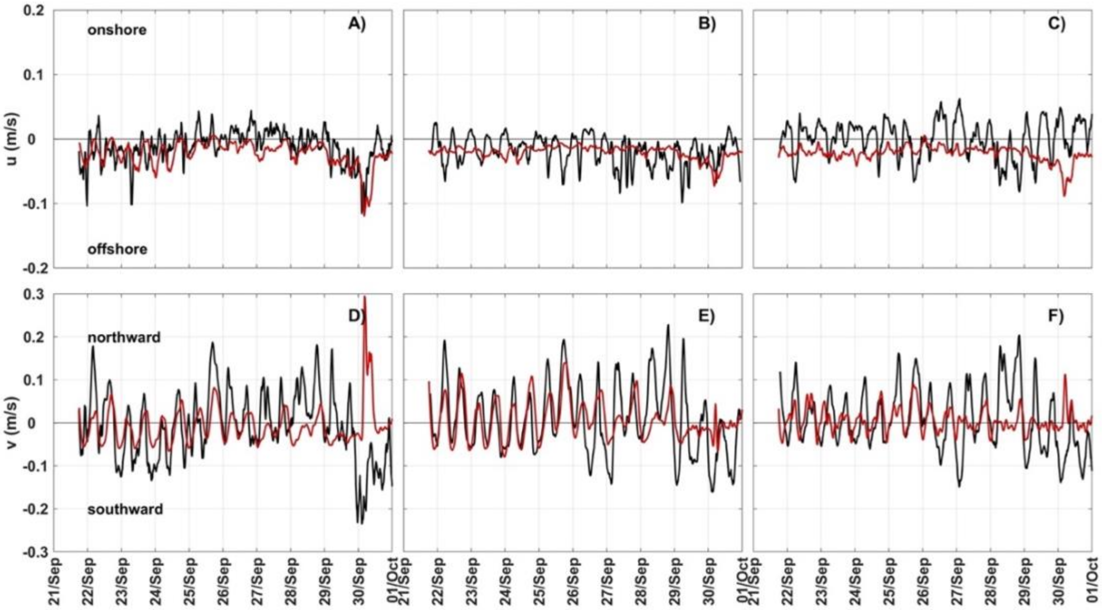

Figure 4.3.1.2. Modeled (red lines) vs measured (black lines) cross-shore (U) and alongshore (V) flow components for: (A and D) the southern, (B and E) central and northern (C, F) near-surfzone ADCP locations, using nspectrum= 16 (red) at the offshore boundary.

Figura 4.3.1.2. Modelado (líneas rojas) vs medido (líneas negras) de los componentes de flujo transversal (U) y longitudinal (V) para: (A y D) la sección sur, (B y E) central y (C, F) las ubicaciones de los ADCP cercanos a la rompiente en el norte, usando nspectrum=16 (rojo) en la frontera mar adentro.

Table VI. Statistical results for tideloc = 4 and tidal signal reduced 1.5% at northern boundary and offshore boundary segmented on 16.

Tabla VII. Resultados estadísticos para parámetro tideloc = 4 y reducción de la señal de la marea de un1.5% en la frontera norte y la frontera mar adentro está dividida en 16 segmentos.

Nspectrum = 16									
STATISTIC TEST	**RSME**			**Bias**			**R**		
Variable/Site	**S**	**C**	**N**	**S**	**C**	**N**	**S**	**C**	**N**
Hs (m)	0.2	0.2	0.2	0.1	0.1	0.0	0.8	0.8	0.7
Tp (s)	0.4	0.6	1.1	-0.1	-0.1	-0.1	0.6	0.6	0.4
Dir (o)	4.0	6.3	12.6	-2.2	-2.1	-2.3	0.6	0.6	0.6
u (m/s)	0.0	0.0	0.0	0.0	0.0	0.0	0.4	0.3	0.3
v (m/s)	0.1	0.1	0.1	0.0	0.0	0.0	0.4	0.6	0.4

4.3.2. Effects of wave directionality on nearshore circulation

Each model simulation lasted 9 days, encompassing both spring and neap tides. Model results represent an 8-day average, excluding the first day allocated for spin-up (Figures 4.3.2.1, 4.3.2.2 and 4.3.2.3 E).

Summer – Reflective beach state

Southwesterly waves (220°) during summer produced mean northward (upcoast) flows in the surf zone. The strongest flows (~ 1 m/s) occurred near the southern headland, extending beyond the surfzone to depth of up to 5 m, with speeds exceeding 1 m/s at depths of up to 8 m. Flows were relatively alongshore-uniform, with the northward-directed flow largely confined to the surf zone, averaging 1.4 m/s (Figure 4.3.2.1 B). A deflected rip current was observed in the central and northern sections, producing offshore flows (<0.2 m/s) at depths of 4 m. Shore-normal waves (270°) generated the strongest flows (~ 0.5 m/s) within the surf and swash zone, particularly at both beach ends. A landward flow was observed near the northern boundary, while the mean flow at the southern boundary was directed offshore. The central section featured offshore-directed rip cells with velocities around 0.8 m/s (Figure 4.3.2.1 C). Northwesterly waves (320°) induced southward-directed (downcoast) flows, with the strongest velocities (1 m/s) occurring in the northern section and extending up to depths of 8 m. The alongshore mean flow was predominantly southward, with maximum speeds of 1 m/s, all confined within the surf zone (Figure 4.3.2.1 D).

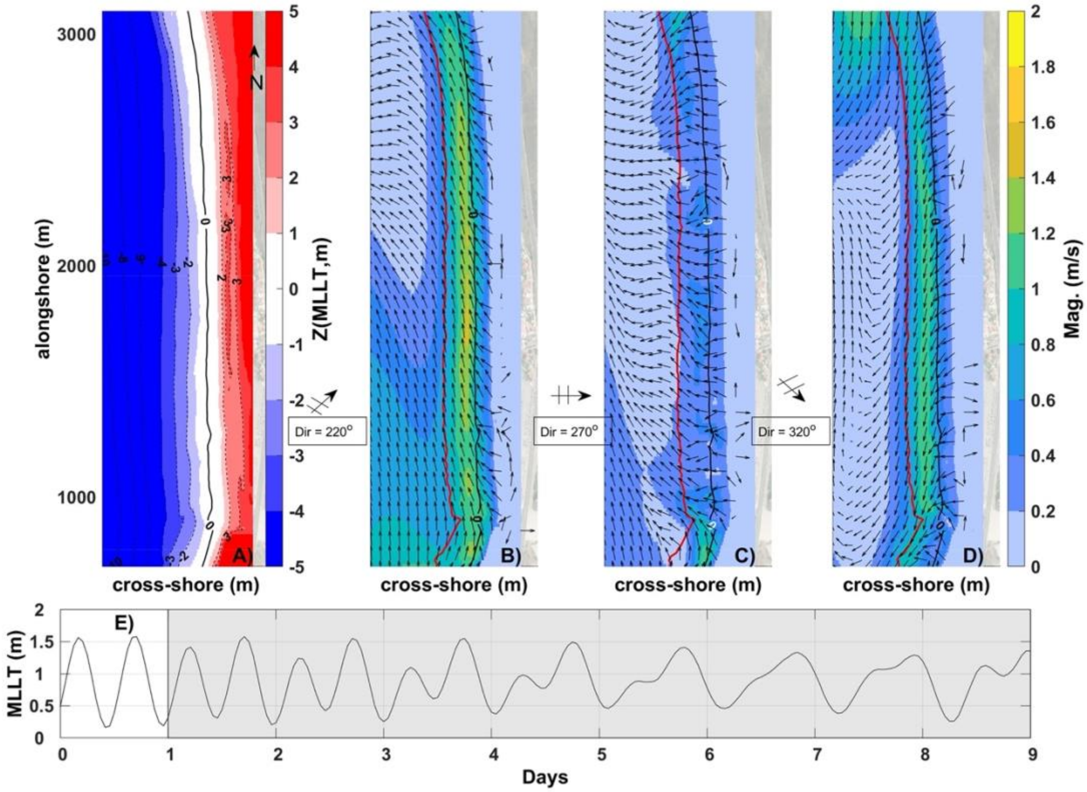

Figure 4.3.2.1 A) Digital Elevation Model (DEM) representing the summer-fall topobathymetric configuration of La Misión Beach. The red line marks the outer edge of the surf zone. Mean 8-day circulation pattern is shown. (B-D) Mean circulation patterns under different offshore wave directions: (B) southwest (SW), (C) west (W), and (D) northwest (NW). (E) Tidal level time series highlighting the period used to compute the mean circulation. The red line in all panels represents the mean outer limit of the surf zone.

Figura 4.3.2.1. A) Modelo Digital de Elevación (DEM) que representa la configuración topobatimétrica de verano-otoño de la playa La Misión. La línea roja marca el borde exterior de la zona de rompiente. Se muestra el patrón de circulación promedio de 8 días. (B-D) Patrones de circulación promedio bajo diferentes direcciones de oleaje mar adentro: (B) suroeste (SW), (C) oeste (W) y (D) noroeste (NW). (E) Serie temporal del nivel de marea que destaca el período usado para calcular la circulación promedio. La línea roja en todos los paneles representa el límite exterior promedio de la zona de rompiente.

Winter - Dissipative beach state

Southwesterly waves (220°) during winter generated a mean northward (upcoast) flow. The strongest currents (>1 m/s) occurred near the southern headland, extending to greater depths (up to 8 m) than in summer (Figure 4.3.2.1 and 4.3.2.2

B). Alongshore flows exhibited slight spatial variation. In central and northern sections, flow intensification (>1 m/s) was observed at depths of 2–3 m. At greater depths (4–8 m), circulation patterns varied alongshore: in the south, currents remained northward-directed, while in the central and northern beach, they shifted offshore with minimal velocities (<0.2 m/s) (Figure 4.3.2.2 B).

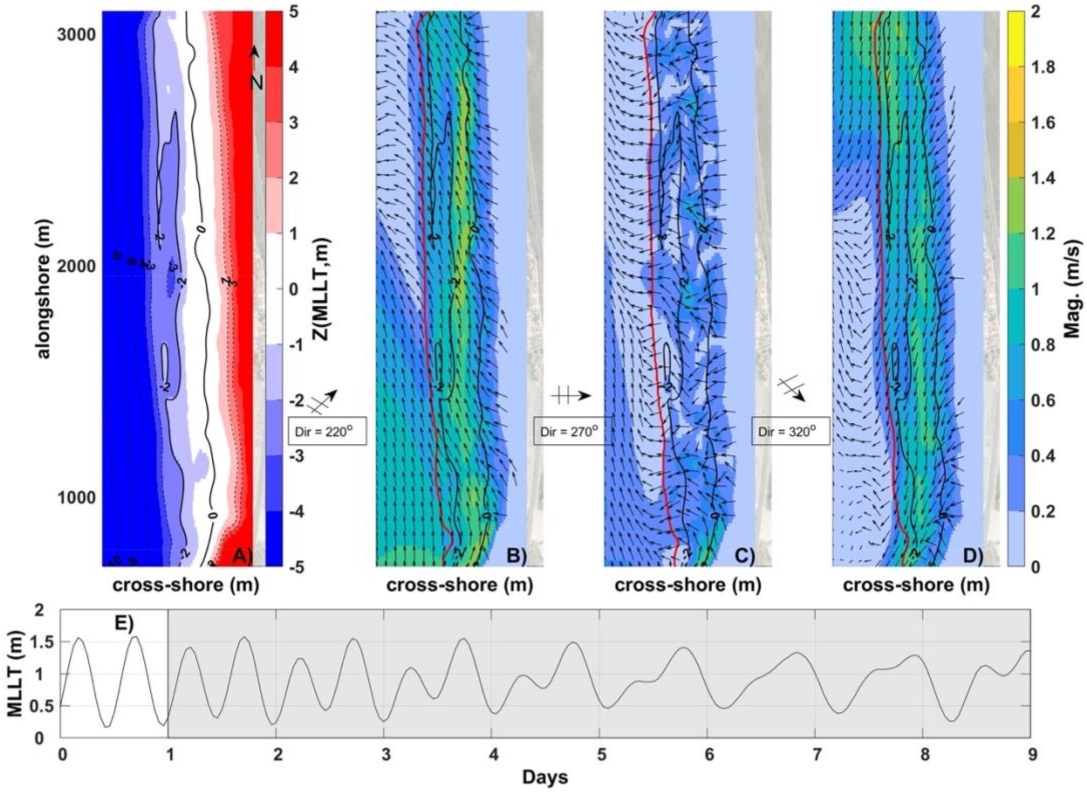

Figure 4.3.2.2 A) Digital Elevation Model (DEM) representing the winter topobathymetric configuration of La Misión Beach. The red line marks the outer edge of the surf zone. Mean 8-day circulation pattern is shown. (B-D) Mean circulation patterns under different offshore wave directions: (B) southwest (SW), (C) west (W), and (D) northwest (NW). (E) Tidal level time series highlighting the period used to compute the mean circulation. The red line in all panels represents the mean outer limit of the surf zone.

Figura 4.3.2.2. A) Modelo Digital de Elevación (DEM) que representa la configuración topobatimétrica de invierno de la playa La Misión. La línea roja marca el borde exterior de la zona de rompiente. Se muestra el patrón de circulación promedio de 8 días. (B-D) Patrones de circulación promedio bajo diferentes direcciones de oleaje mar adentro: (B) suroeste (SW), (C) oeste (W) y (D) noroeste (NW). (E) Serie temporal del nivel de marea que destaca el período usado para calcular la circulación promedio. La línea roja en todos los paneles representa el límite exterior promedio de la zona de rompiente.

Westerly waves (270°) generated the strongest flows (~1 m/s) near the southern headland and northern rocky reef. Rip currents were present along the entire beach, with peak speeds up to 0.8 m/s. These rip currents were more frequent in the central and northern beach. The strongest flows occurred in the surf zone, while deeper zones exhibited minimal velocities (Figure 4.3.2.2 C). Northwesterly waves (320°) induced southward-directed flows, with maximum velocities (>1 m/s) reaching depths of up to 6 m in the northern section. Flows intensified to 1 m/s along the beach, particularly in constricted areas at depths of 2–3 m. In the southern section, strong currents were observed in both the surf zone and greater depths than 6 m. A southward flow with mean velocities of 0.5 m/s was observed in the north, while in the central and southern sections, flow shifted offshore with weaker velocities (< 0.2 m/s) (Figure 4.3.2.2 D).

Spring – Intermediate beach state

Southwesterly waves (220°) generated northward mean currents, with the strongest velocities near the southern headland, extending to depths of up to 8 m, similar to winter conditions (Figure 4.3.2.2 and 4.3.2.1 A). A strong current developed in the gap between the sandbar and the headland, then diverted into the southern section where the sandbar was segmented. The strongest flows (>1 m/s) occurred in the surfzone, while weaker northward currents (~1 m/s) extended into deeper waters beyond 4 m. In the northern section, alongshore flows intensified to 1.5 m/s in the surf zone but remained weak (< 0.2 m/s) in deeper areas. Flows along the sandbar in the southern section were weaker than those at the northern or southern beach ends (Figure 4.3.2.3 B). Westerly shore-normal waves (270°) generated the strongest flows (~1 m/s) at both beach ends, and rip currents developed. The strongest offshore flows (~0.8 m/s) occurred in the gaps along the sandbar. At the southern headland, a divergent current emerged, with northward flow in shallower areas and offshore flow through the sandbar channel (~0.8 m/s). The surfzone is the most dynamic area (Figure 4.3.2.3 C).

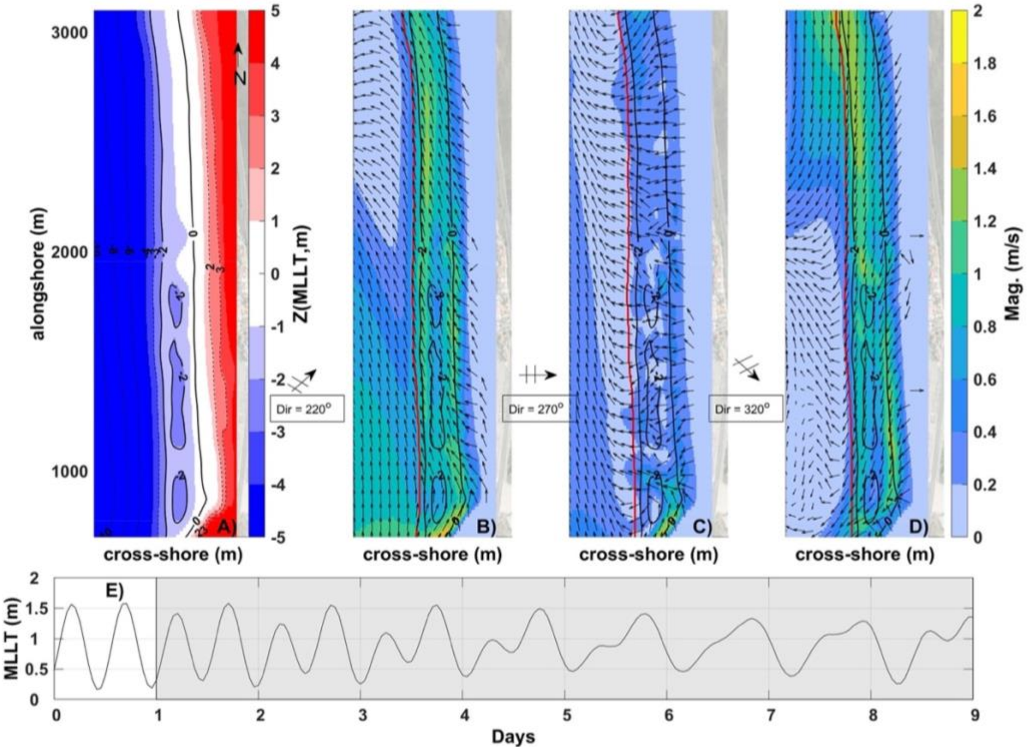

Figure 4.3.2.3. A) Digital Elevation Model (DEM) representing the spring topobathymetric configuration of La Misión Beach. The red line marks the outer edge of the surf zone. Mean 8-day circulation pattern is shown. (B-D) Mean circulation patterns under different offshore wave directions: (B) southwest (SW), (C) west (W), and (D) northwest (NW). (E) Tidal level time series highlighting the period used to compute the mean circulation. The red line in all panels represents the mean outer limit of the surf zone.

Figura 4.3.2.3. A) Modelo Digital de Elevación (DEM) que representa la configuración topobatimétrica de primavera de la playa La Misión. La línea roja marca el borde exterior de la zona de rompiente. Se muestra el patrón de circulación promedio de 8 días. (B-D) Patrones de circulación promedio bajo diferentes direcciones de oleaje mar adentro: (B) suroeste (SW), (C) oeste (W) y (D) noroeste (NW). (E) Serie temporal del nivel de marea que destaca el período usado para calcular la circulación promedio. La línea roja en todos los paneles representa el límite exterior promedio de la zona de rompiente.

Northwesterly waves (320°) generated southward flows, with the strongest velocities (>1 m/s) reaching depths of up to 6 m in the north. Flows intensified to 1 m/s near the shoreline, particularly in constricted areas at depths of 2–3 m. In the southern section, the strongest flows were confined to the surfzone. Southward flows (~0.5 m/s) were also observed in the north at depths greater than 6 m, while in central and southern beach, flows turned offshore with velocities below 0.2 m/s. At the southern headland, a divergent current pattern formed across the sandbar gap, with northward flows in shallower waters (Figure 4.3.2.3 D).

4.3.3. Seasonal circulation

Seasonal flow patterns were analyzed using representative morphological and wave conditions for each season (Figures 4.2.2.1, 4.2.2.2 and 4.2.2.3).

Summer-Fall: Flows were predominantly upcoast and confined to the surf zone. A cyclonic eddy with speeds up to 1 m/s developed at the southern end during peak wave conditions ($\overline{H_s}$~1.5 m). In the north, where waves were smaller ($\overline{H_s}$~1.2 m), offshore flows (~0.6 m/s) extended down to 4 m depth. Alongshore flows were stronger in the central (0.8 m/s) and northern (0.4 m/s) beach, while offshore velocities remained weaker (< 0.2m/s) (Figures 4.3.3.1 A and 4.3.3.2 A).

Winter: The wave height was similar along the beach ($\overline{H_s}$~2.2 m) where current measurements were collected. Cross-shore flows dominated over the alongshore and exhibited significant spatial variability. Strong offshore currents beyond the surf zone (up to 0.5 m/s) were associated with sandbar gaps. Deflected rip currents were observed in the south, while an anticyclonic eddy developed in the northern end, generating offshore flows. Weak offshore currents (<0.2 m/s) persisted beyond 4 m depth, and northward flows of up to 0.5m/s were observed near the southern headland (Figures 4.3.3.1 B and 4.3.3.2 B).

Spring: Weak northward flows occurred beyond 4 m depth. Wave heights were relatively uniform along the beach ($\overline{H_s}$~1.3 m), except in the south, where the presence of a sandbar induced alongshore variability. Offshore flows (~0.5 m/s) dominated in gaps between sandbars in the central and southern beach. In the north, offshore flows also prevailed despite the lack of sandbars. Cyclonic eddy circulation (up to 0.9 m/s) was observed in the south, while anticyclonic circulation (up to 0.5 m/s) occurred at the northern end (Figures 4.3.3.1 C, 4.3.3.2 C).

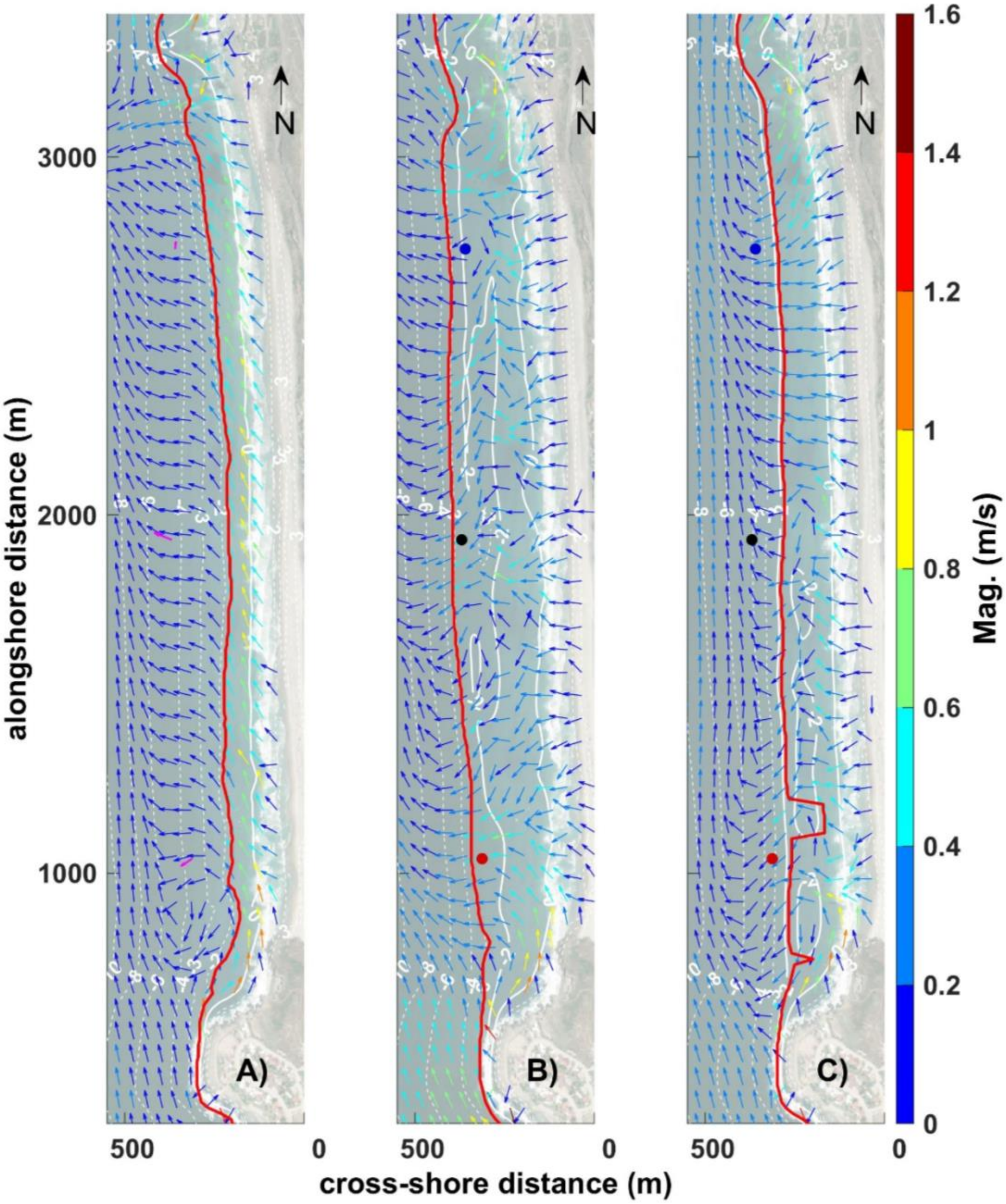

Figure 4.3.3.1 Mean nearshore circulation for: (A) summer-fall; (B) winter; and (C) spring. Red line denotes the mean surf zone outer limit. The virtual ADCP are denoted by the dots (red-southern; black-central and blue-northern).

Figura 4.3.3.1. Circulación promedio en la zona cercana a la costa para: (A) verano-otoño; (B) invierno; y (C) primavera. La línea roja indica el límite exterior promedio de la zona de rompiente. Los ADCP virtuales están representados por los puntos (rojo-sur; negro-centro y azul-norte).

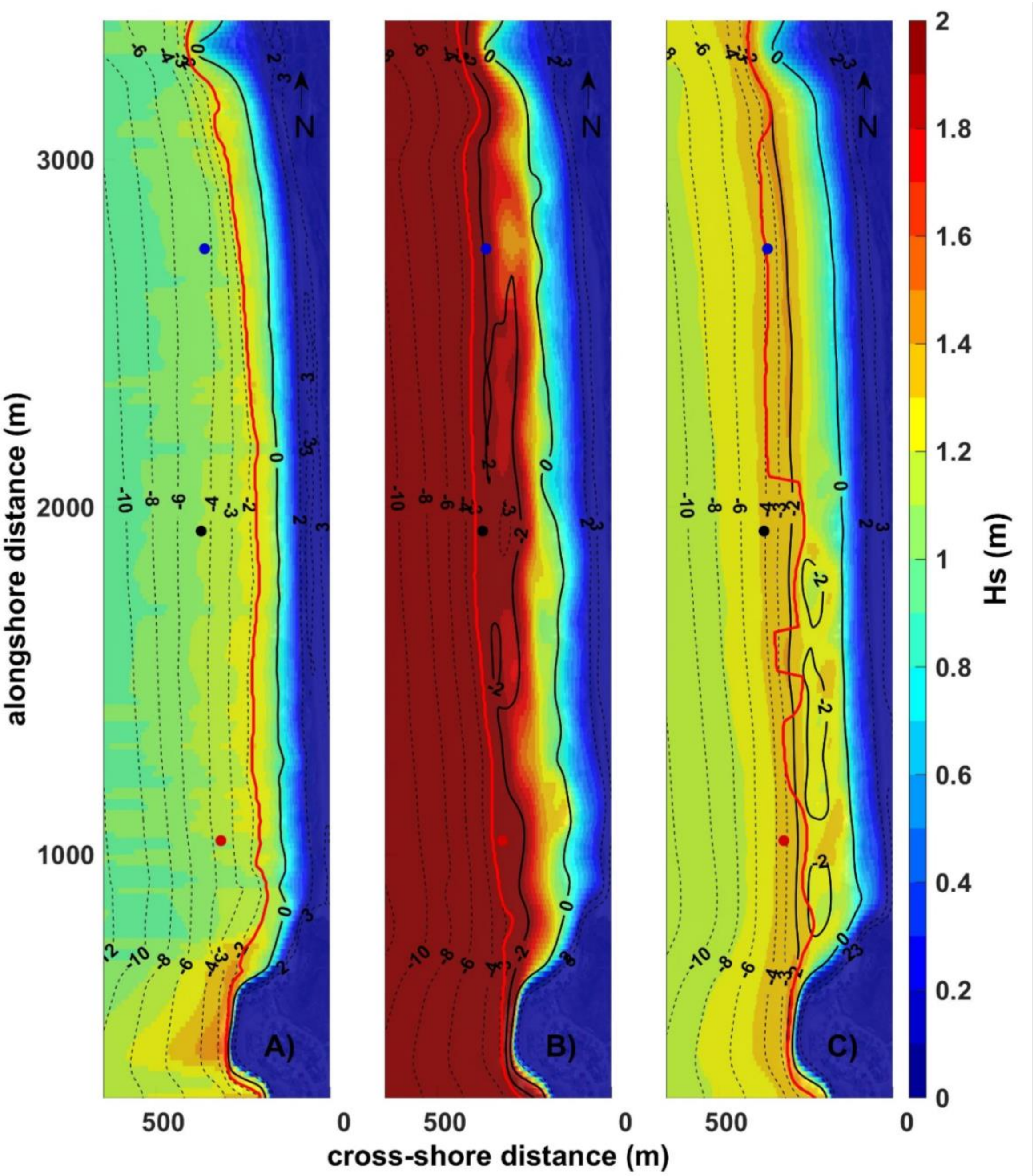

Figure 4.3.3.2. Mean Hs for: (A) summer-fall; (B) winter; and (C) spring. Red line denotes the mean surf zone outer limit, The virtual ADCP are denoted by the dots (red-southern; black-central and blue-northern).

Figura 4.3.3.2. Altura significativa promedio (Hs) para: (A) verano-otoño; (B) invierno; y (C) primavera. La línea roja indica el límite exterior promedio de la zona de rompiente. Los ADCP virtuales están representados por los puntos (rojo-sur; negro-centro y azul-norte).

4.3.3.1. Summer- fall

Under low-energy wave conditions (Hs ~ 1 m), alongshore flows outside the surf zone were weak (<0.2 m/s) and primarily influenced by tidal elevation. Although generally weak, the alongshore flow exhibited upcoast trend. The cross-shore component was also weak, with velocities below 0.1m/s. In contrast, stronger alongshore flows (up to 0.5 m/s) dominated withing the surf zone. Maximum velocities were observed near the southern headland (0.8 m/s), while the northern rocky outcrop showed velocities of up to 0.4 m/s (Figure 4.3.3.1.1A).

Wave direction varied alongshore: in the central and northern sections, dominant waves approached from the southwest, whereas in the southern section, waves came from the west (Figures 4.3.3.1.1B, C, and D). Simulated circulation patterns aligned well with field observations. During a flood tide, flow was directed upcoast, and the cross-shore velocity was near zero, indicating a neutral cross-shore component (Figures 4.3.3.1.1 F and G).

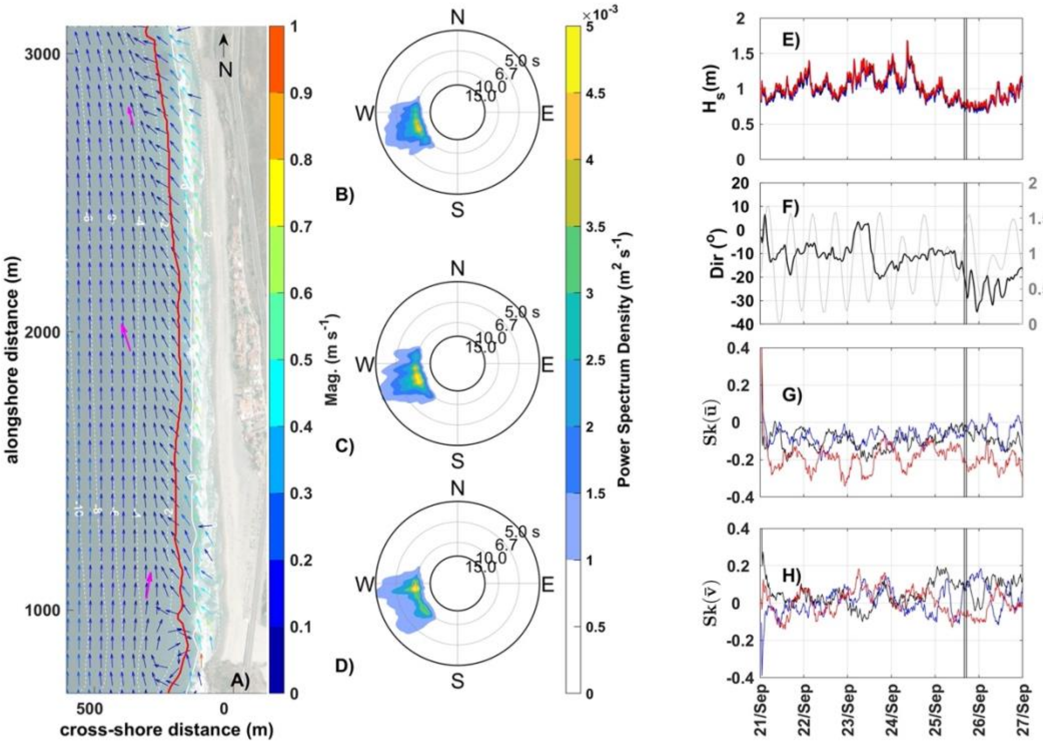

Figure 4.3.3.1.1 Low wave energy conditions instant during flood tide (shadow zone) for summer-fall configuration: Mean circulation (A). Directional wave spectrum for the northern (blue) (B), central (black) (C) and southern section (red) (D). Hs (E). Offshore directionality and tidal level (F). Cross-shore velocity skewness (F). Alongshore velocity skewness (G). Red line denotes the instant surf zone outer limit. Magenta arrows denote ADCP measurements.

Figura 4.3.3.1.1. Condiciones instantáneas de baja energía de oleaje durante marea alta (zona sombreada) para la configuración de verano-otoño: Circulación media (A). Espectro direccional de oleaje para la sección norte (azul) (B), central (negro) (C) y sur (rojo) (D). Hs (E). Direccionalidad del oleaje en mar abierto y nivel de marea (F). Asimetría de la velocidad en la dirección transversal a la costa (F). Asimetría de la velocidad en la dirección paralela a la costa (G). La línea roja indica el límite instantáneo de la zona de rompiente. Las flechas magenta representan las mediciones del ADCP.

During moderate wave conditions (1m < Hs < 2m), current speeds within the surf zone increased, reaching up to 0.6 m/s. During ebb tide, a weak downcoast flow (<0.2m/s) was observed outside the surf zone. However, inside the surf zone, the alongshore current was directed upcoast (Figure 4.3.3.1.2). Maximum current velocities occurred near the southern headland (0.6 m/s) and the northern rocky reef (0.4 m/s), (Figure 4.3.3.1.2A). The cross-shore component intensified due to shore-normal wave incidence and increased wave energy, producing stronger offshore-directed flows in the southern section compared to the central and northern sections. In contrast, the alongshore component weakened relative to the low wave energy scenario (Figures 4.3.3.1.2B, C, and D; 4.3.3.1.2 F, G).

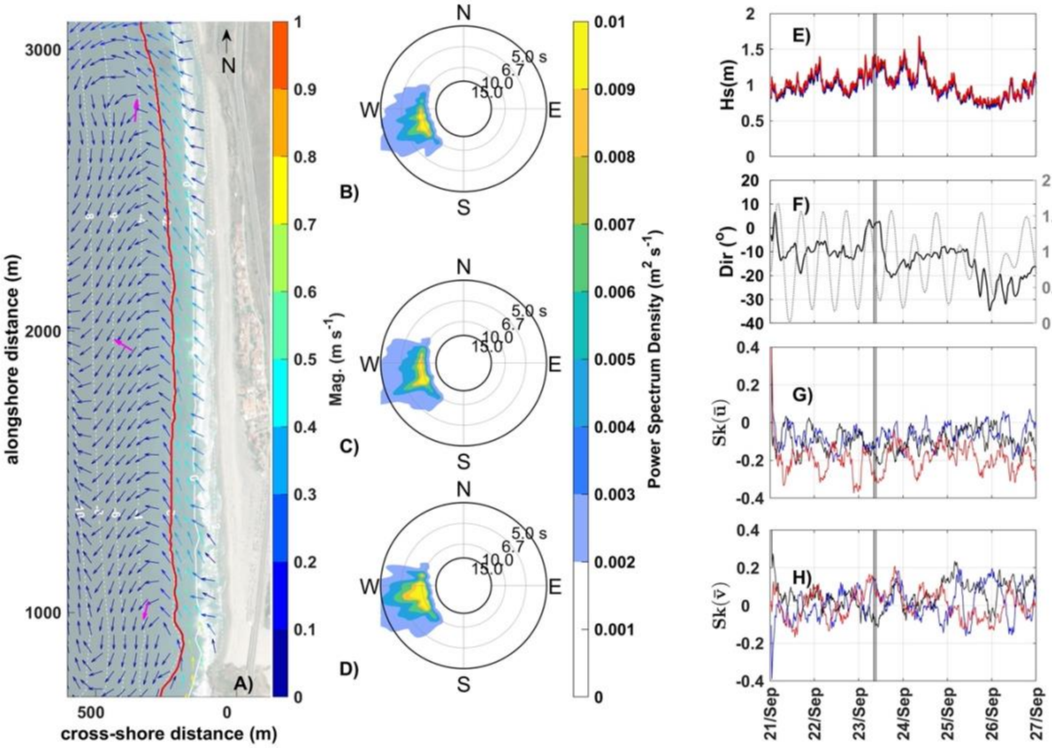

Figure 4.3.3.1.2. Mild wave energy conditions instant during ebb tide (shadow zone) for summer-fall configuration: Mean circulation (A). Directional wave spectrum for the northern (blue) (B), central (black) (C) and southern section (red) (D). Hs (E). Offshore directionality and tidal level (F). Cross-shore velocity skewness(F). Alongshore velocity skewness(G). Red line denotes the instant surfzone outer limit. Magenta arrows denote ADCP measurements.

Figura 4.3.3.1.2. Condiciones instantáneas de baja energía de oleaje durante marea alta (zona sombreada) para la configuración de verano-otoño: Circulación media (A). Espectro direccional de oleaje para la sección norte (azul) (B), central (negro) (C) y sur (rojo) (D). Hs (E). Direccionalidad del oleaje en mar abierto y nivel de marea (F). Asimetría de la velocidad en la dirección transversal a la costa (F). Asimetría de la velocidad en la dirección paralela a la costa (G). La línea roja indica el límite instantáneo de la zona de rompiente. Las flechas magenta representan las mediciones del ADCP.

4.3.3.2. Winter

The presence of sandbars during winter resulted in more complex circulation patterns. Under moderate wave energy conditions, offshore-directed flows (~0.4 m/s) were associated with sandbar gaps and a rhythmic sandbar configuration. These offshore flows dominated within the surf zone, intensifying through sandbar gaps and extending to depths of up to 8 m, although with weaker velocities (<0.1 m/s). Rip circulation was prominent in the central and southern beach, while a persistent southwest-directed rip current developed in the northern beach (Figure 4.3.3.2.1A). The directional wave spectrum indicated predominantly shore-normally wave incidence in the central and northern beach, with a slight dominance of northwest-directed waves in the southern section (Figures 4.3.3.2.1B, C, and D). The cross-shore velocity component was strong, reaching up to 0.4 m/s and dominated by offshore-directed flow. Meanwhile the alongshore component exhibited a downcoast pattern, even during the flood tide phase. (Figures 4.3.3.2.1F and G).

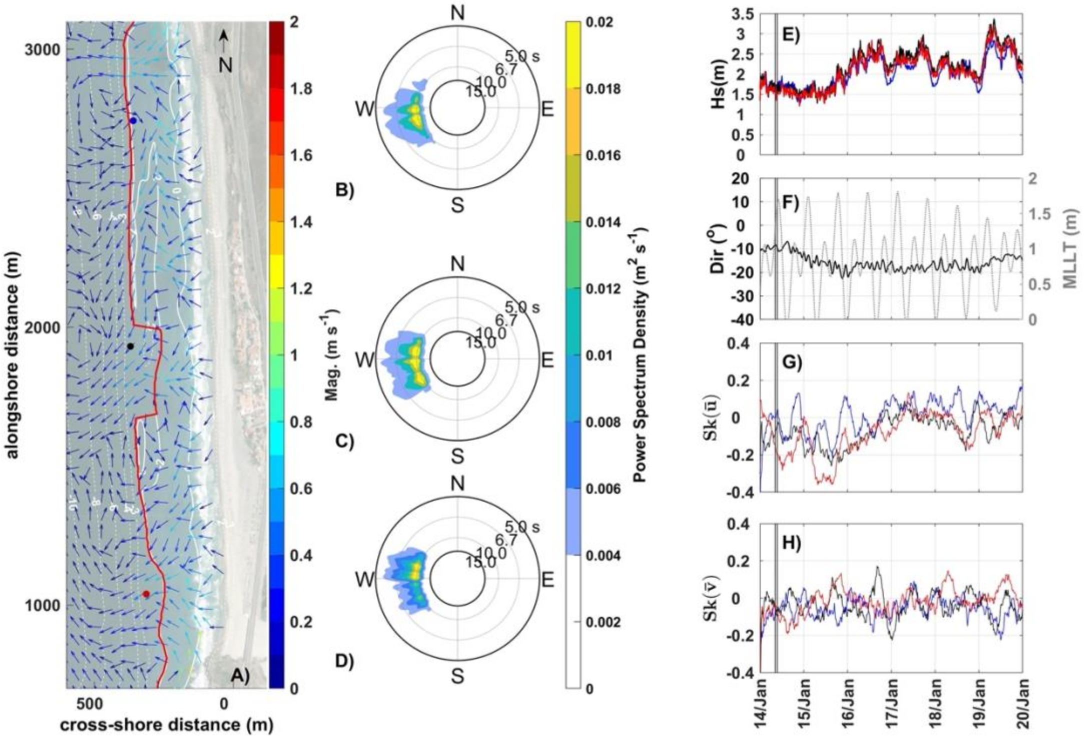

Figure 4.3.3.2.1. Low wave energy conditions instant during flood tide (shadow zone) for winter configuration: Mean circulation (A). Directional wave spectrum for the northern (blue) (B), central (black) (C) and southern section (red) (D). Hs (E). Offshore directionality and tidal level (F). Cross-shore velocity skewness (F). Alongshore velocity skewness (G). Red line denotes the instant surfzone outer limit.

Figura 4.3.3.2.1. Condiciones instantáneas de baja energía de oleaje durante marea alta (zona sombreada) para la configuración de invierno: Circulación media (A). Espectro direccional de oleaje para la sección norte (azul) (B), central (negro) (C) y sur (rojo) (D). Hs (E). Direccionalidad del oleaje en mar abierto y nivel de marea (F). Asimetría de la velocidad en la dirección transversal a la costa (F). Asimetría de la velocidad en la dirección paralela a la costa (G). La línea roja indica el límite instantáneo de la zona de rompiente. Las flechas magenta representan las mediciones del ADCP.

During high-energy conditions, offshore flows dominated down to a depth of 4 m, while a northwestward alongshore current developed near the southern headland (~1 m/s). Offshore flows intensified through sandbar gaps reaching values of 0.6m/s (Figure 4.3.3.2.2A). The southern and central section exhibited the most intense offshore flows, in contrast to the weaker flows observed along the northern beach (Figures 4.3.3.2.2B, C, and D). The cross-shore velocity component increased reaching values of 0.6m/s offshore. Meanwhile, the alongshore component showed a prevailing downcoast trend.Tidal variations outside the surf zone appeared to have a stronger influence on the central and suthern sections than on the northern section (Figures 4.3.3.2.2F and G).

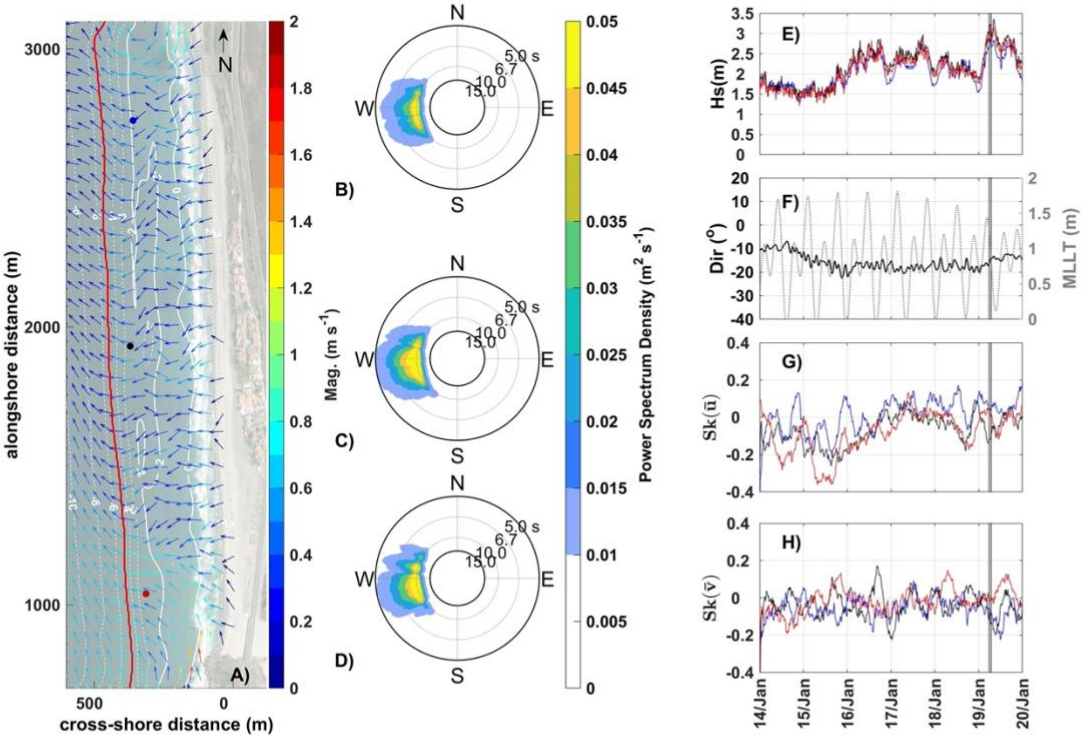

Figure 4.3.3.2.2. High wave energy conditions instant during ebb tide (shadow zone) for winter configuration: Mean circulation (A). Directional wave spectrum for the northern (blue) (B), central (black) (C) and southern section (red) (D). Hs (E). Offshore directionality and tidal level (F). Cross-shore velocity skewness(F). Alongshore velocity skewness(G). Red line denotes the instant surfzone outer limit.

Figura 4.3.3.2.2. Condiciones instantáneas de baja energía de oleaje durante marea alta (zona sombreada) para la configuración de invierno: Circulación media (A). Espectro direccional de oleaje para la sección norte (azul) (B), central (negro) (C) y sur (rojo) (D). Hs (E). Direccionalidad del oleaje en mar abierto y nivel de marea (F). Asimetría de la velocidad en la dirección transversal a la costa (F). Asimetría de la velocidad en la dirección paralela a la costa (G). La línea roja indica el límite instantáneo de la zona de rompiente. Las flechas magenta representan las mediciones del ADCP.

4.3.3.3. Spring

Under low-energy conditions, offshore flows dominated at depths shallower than 2 m, while northward flows prevailed between 2 m and 8 m depth. Offshore flows through sandbar gaps reached velocities of up to 0.3 m/s. Stronger flows (~0.6 m/s) were observed near the rocky reef and southern headland, where rip circulation developed (Figure 4.3.3.3.1 A). The southern section of the beach was the most dynamic, followed by the northern section, both exhibiting a predominant offshore flow direction. In contrast, the central beach displayed weaker offshore flows (Figure 4.3.3.3.1 B, C and D). The cross-shore velocity component showed offshore dominance in the southern and northern beach. However, the alongshore component exhibited spatial variation: a downcoast trend was observed in the southern section, while an upcoast trend was found in the central and northern sections (Figure 4.3.3.3.1 F, G).

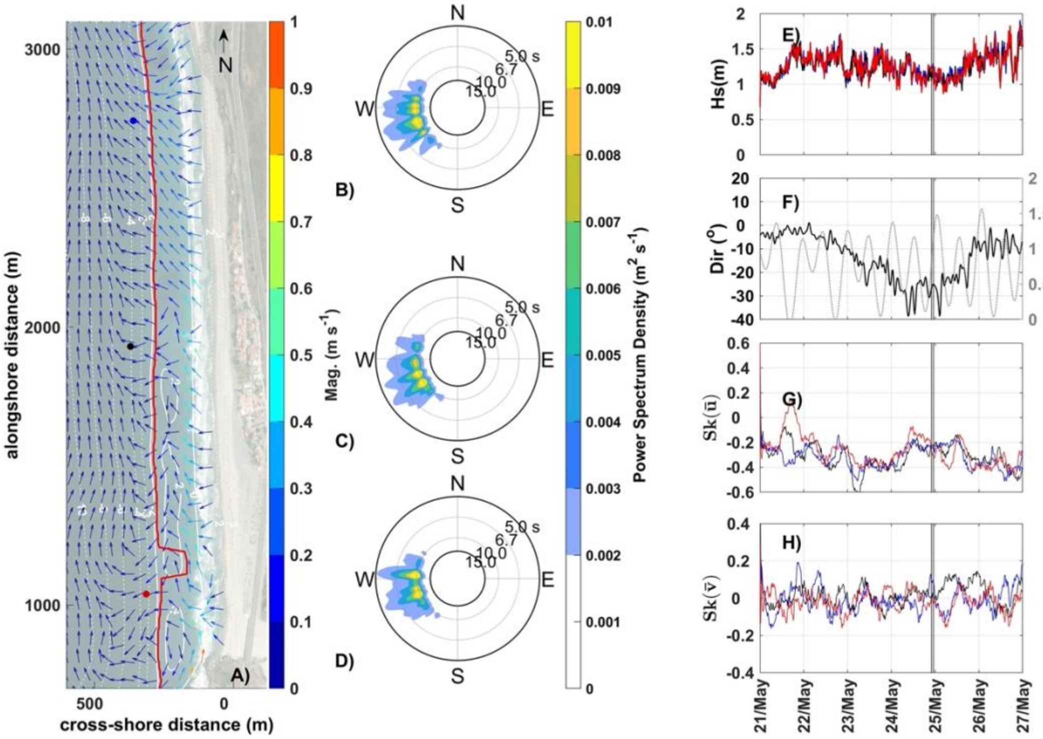

4.3.3.3.1 Low wave energy conditions instant during flood tide (shadow zone) for spring configuration: Mean circulation (A). Directional wave spectrum for the northern (blue) (B), central (black) (C) and southern section (red) (D). Hs (E). Offshore directionality and tidal level (F). Cross-shore velocity skewness(F). Alongshore velocity skewness(G). Red line denotes the instant surfzone outer limit.

Figura 4.3.3.3.1. Condiciones instantáneas de baja energía de oleaje durante marea alta (zona sombreada) para la configuración de primavera: Circulación media (A). Espectro direccional de oleaje para la sección norte (azul) (B), central (negro) (C) y sur (rojo) (D). Hs (E). Direccionalidad del oleaje en mar abierto y nivel de marea (F). Asimetría de la velocidad en la dirección transversal a la costa (F). Asimetría de la velocidad en la dirección paralela a la costa (G). La línea roja indica el límite instantáneo de la zona de rompiente. Las flechas magenta representan las mediciones del ADCP.

During moderate wave energy conditions and at instant during the ebb tide offshore flows persisted at shallower depths than 4 m, while upcoast flows were observed between 4 m to 8 m depth. Offshore flows through sandbar gaps reached 0.4 m/s, with stronger flows (~0.6 m/s) near the rocky reef and southern headland, where rip circulation developed in the central and southern sections

(Figure 4.3.3.3.2 A, B, C and D). The cross-shore velocity component showed offshore dominance in the southern and northern sections, while the central beach exhibited weak flow (<0.1m/s) The alongshore component denoted spatial variation: a downcoast trend in the southern section and an upcoast trend in the central and northern sections (Figure 4.3.3.3.2 F and G).

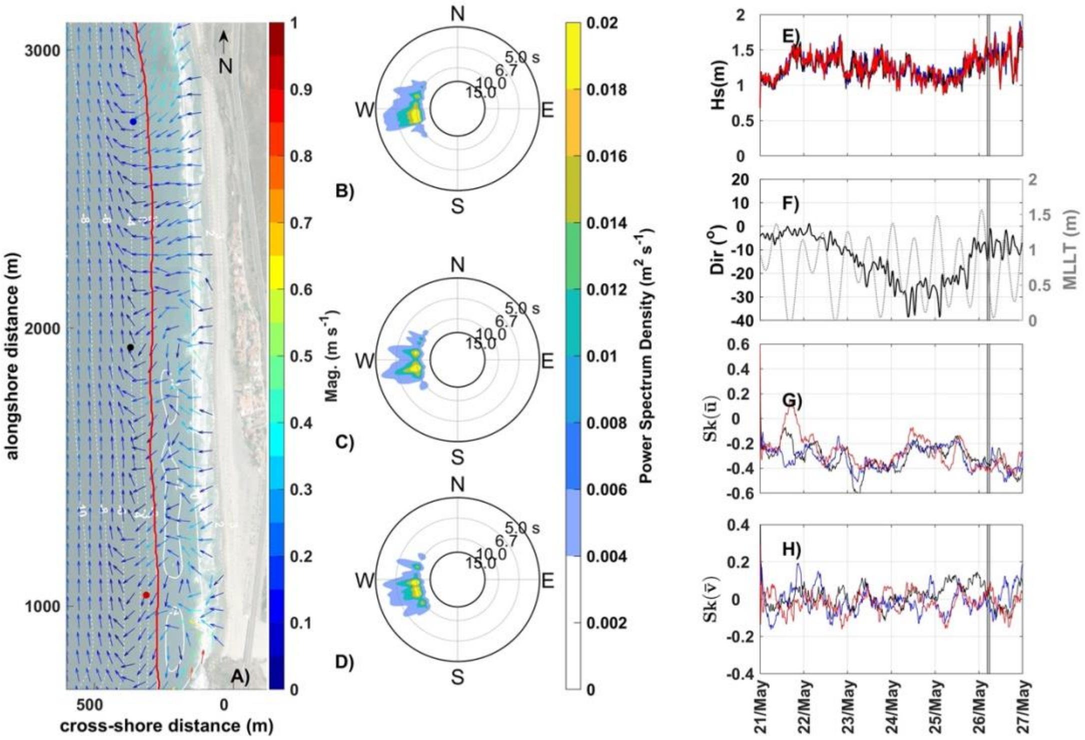

4.3.3.3.2. Mild wave energy conditions instant during ebb tide (shadow zone) for spring configuration: Mean circulation (A). Directional wave spectrum for the northern (blue) (B), central (black) (C) and southern section (red) (D). Hs (E). Offshore directionality and tidal level (F). Cross-shore velocity skewness(F). Alongshore velocity skewness(G). Red line denotes the instant surfzone outer limit.

Figura 4.3.3.3.2. Condiciones instantáneas de baja energía de oleaje durante marea alta (zona sombreada) para la configuración de primavera: Circulación media (A). Espectro direccional de oleaje para la sección norte (azul) (B), central (negro) (C) y sur (rojo) (D). Hs (E). Direccionalidad del oleaje en mar abierto y nivel de marea (F). Asimetría de la velocidad en la dirección transversal a la costa (F). Asimetría de la velocidad en la dirección paralela a la costa (G). La línea roja indica el límite instantáneo de la zona de rompiente. Las flechas magenta representan las mediciones del ADCP.

4.3.4. Morphological change during September 21 until October 21

During the ADCP deployment period (September 21 to October 7, 2021) morphological surveys were carried out at both the beginning and end of the measurement campaign. The morphological changes assessed trough DEM differencing between surveys conducted on September 21 and October 7 revealed notable sediment dynamic across the study area. In the southern section, a sandbar developed at approximately 2m of depth. In the central section, the sandbar was observed at around 1m depth. Meanwhile the northern section showed accretion on the subaerial beach, attributed to the formation of intertidal sandbar.

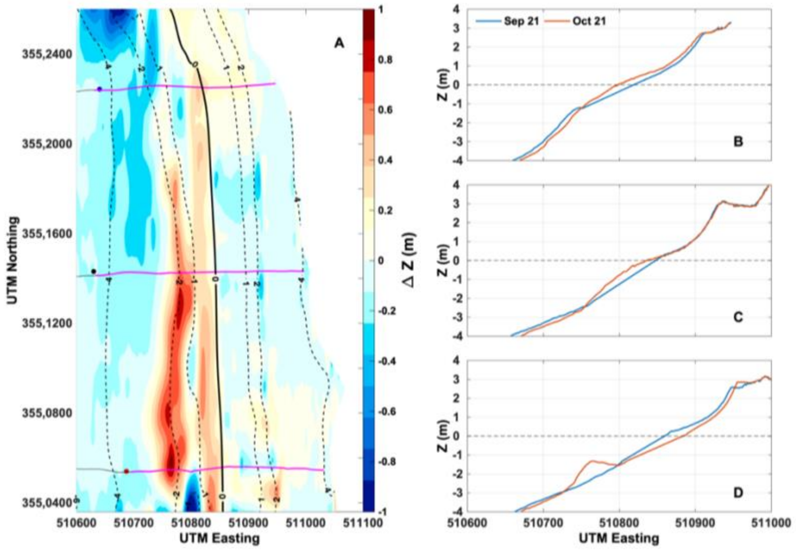

Figure 4.3.4.1. Morphological changes during ADCP deployment period at La Misión beach. (A) Map of elevation change, red denoting accretion and blue denoting erosion. (B) Beach profile for the northern section. (C) Beach profile for the central section. (D) Beach profile for the southern section. Blue lines represent the initial survey (sep 21) and red lines represent the final survey (7 October).

Figura 4.3.4.1. Cambios morfológicos durante el periodo de despliegue de ADCPs en playa La Misión. (A) Mapa de cambio de elevación, donde el color rojo indica acreción y el azul indica erosión. (B) Perfil de playa para la sección norte. (C) Perfil de playa para la sección central. (D) Perfil de playa para la sección sur. Las líneas azules representan el levantamiento inicial (21 de septiembre) y las líneas rojas representan el levantamiento final (7 de octubre).

4.4. Discussion

The nearshore circulation at La Misión exhibits distinct spatial variability, driven by morphological differences related to the presence and size of sandbars and berms. The southern beach experiences higher wave heights (0.1 to 0.25 m) compared to the central and northern sections, with the strongest cross-shore flows influenced by the southern headland. Wave focusing at the headland is modulated by offshore wave angle, which governs refraction and the subsequent intensification of flow near the headland. Other headland-bound beaches have presented similar circulation patterns, such as Torrey Pines Beach, California (MacMahan et al., 2004), and Tairua Beach, New Zealand (Bryan et al., 2009), where wave refraction and convergence tend to focus wave energy at specific locations and promote the formation of rip currents (Castelle et al., 2020).

Despite the predominantly southwesterly offshore wave direction, out of the surf zone, observations and model results indicate that longshore current variability is largely influenced by tidal level (ebb/flood) and inside of the surf zone it is dominated by the wave directionality. Notably, during summer-fall conditions, the longshore current was an upcoast flow trend outside and inside of the surf zone, which may explain the faster berm recovery in the northern section. Additionally, the presence of a rocky outcrop in the northern section reduces wave height and enhances onshore sediment transport. This aligns with Gallop et al. (2011), who showed that rocky reefs dissipate wave energy and contribute to beach stability. As a result, this dissipative effect likely facilitates faster subaerial beach recovery in the northern section compared to the southern. Under high-energy conditions (Hs > 2 m), the strongest offshore currents were observed in the central and southern sections, aligning with Masselink and Black (1995), who reported that increasing wave height enhances offshore-directed flows. Conversely, weaker offshore flows in the north correspond with smaller wave heights and a greater potential for onshore sediment transport during summer.

The direction of alongshore currents is primarily driven by wave approach angles. Waves arriving at approximately -30° relative to the shoreline generate persistent northward flows under high-energy conditions. Tidal forcing also modulates cross-shore and alongshore flow, consistent with observations at other semi-enclosed beaches (Bruneau et al., 2014). In this study, semidiurnal tides significantly influenced longshore current variability (Figure 4.4.1), enhancing hydrodynamic connectivity between the southern and northern sections. During flood tide, the upcoast flow out of the surf zone (at ~4 m depth) promotes alongshore sediment transport toward the north. If wave energy is low, sediment transport trends onshore. In contrast, ebb tide favors downcoast flows that may also contribute to onshore sediment transport. However, in the southern section, the dominance of offshore-directed currents suggests a greater likelihood of sediment being transported and potentially lost offshore. In winter or spring, when the sandbar forms at depths of 2–3 m, strong cross-shore flows, particularly through sandbar gaps, can disrupt longshore connectivity and limit tidal modulation of currents, potentially leading to partial isolation of different beach sections.

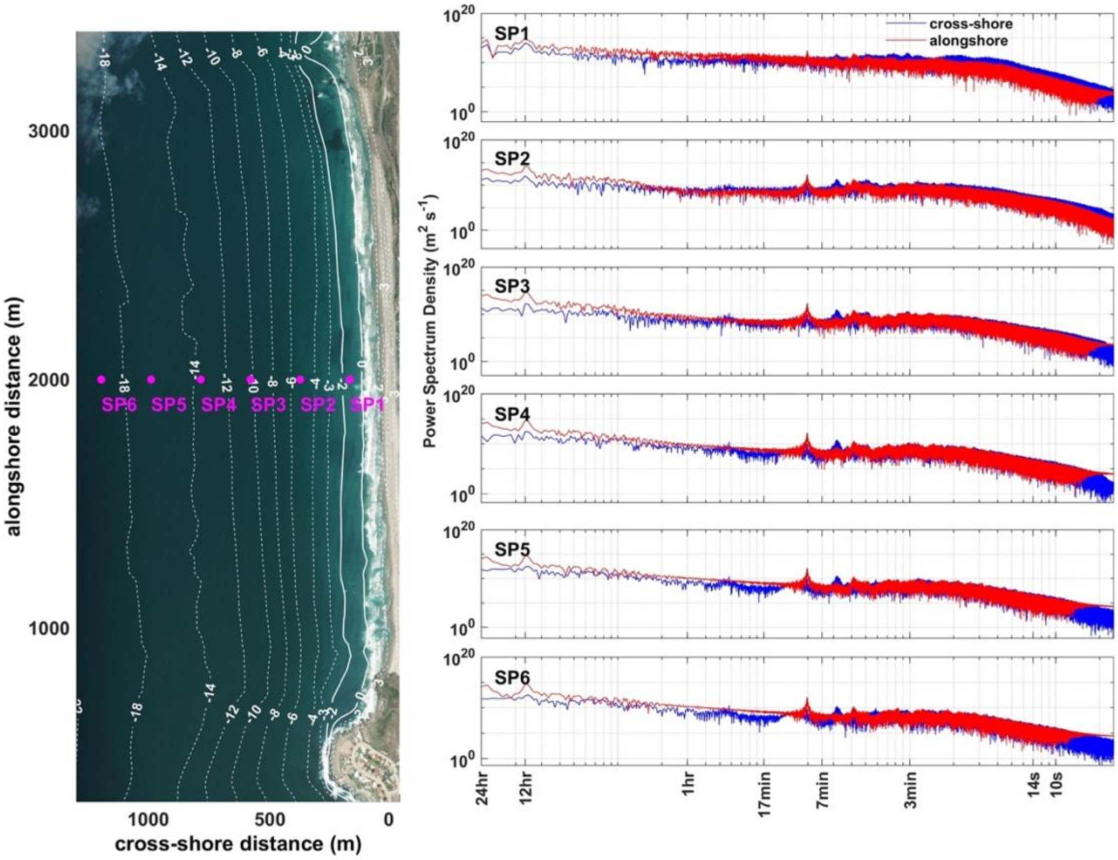

Figure 4.4.1. Location of observation points (left panel) used to obtain power spectrum density (right panel) for cross-shore (blue) and alongshore component (red) corresponding to 9 days of simulation.

Figura 4.4.1. Ubicación de los puntos de observación (panel izquierdo) utilizados para obtener la densidad espectral de potencia (panel derecho) para la componente transversal a la costa (azul) y la componente a lo largo de la costa (rojo), correspondiente a 9 días de simulación.

The seasonal circulation patterns, influenced by morphological changes, can be summarized as follows (Figure 4.4.2):

- **Fall:** As the berm begins forming, the northern section experiences faster recovery. Alongshore flows trend upcoast, and weak onshore cross-shore flows deposit sediment, consistent with observed volumetric differences (Ruiz de Alegría-Arzaburu et al., 2022).

- **Winter:** Dominant offshore cross-shore flows drive sandbar formation. The southern section exhibits more intense offshore flows, causing the sandbar to develop farther offshore (up to 4 m depth) compared to the northern section (Figure 4.4.2B).
- **Spring:** Offshore flows persist in the central and southern sections, due to the presence of a well-formed sandbar, delaying its welding to the shoreline. In contrast, in the northern section, the sandbar migrates shoreward (Figure 4.4.2C).
- **Summer:** Low wave energy conditions promote berm recovery. The direction of the alongshore component plays a key role in the rate of berm development (Figure 4.4.2A).

The persistence of upcoast mean flows during the summer-fall season explains the greater sediment accumulation in the northern section (Figure 4.3.4.1), which exhibits faster berm recovery. Additionally, weak offshore flows in this area promote beach accretion. In contrast, the southern beach experiences persistent offshore flows, likely contributing to its slower berm recovery (Ruiz de Alegría-Arzaburu et al., 2022; Kono-Martínez et al., 2023), but also supporting a more rapid formation of the subtidal sandbar (Figure 4.3.4.1D).

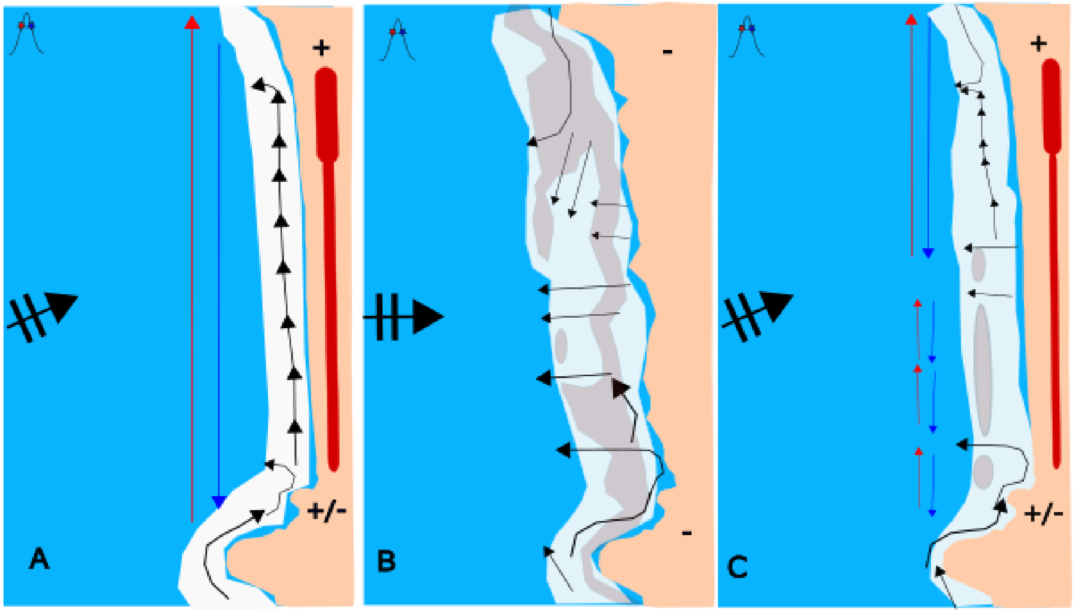

Figure 4.4.2 Schematic representation seasonal circulation patterns based on mean wave directionality: (A) summer–fall, (B) winter, and (C) spring. Blue and red arrows represent ebb and flood tide currents, respectively. Areas of faster accretion, slow accretion and erosion are marked with "+", “+/-” and "–" symbols, respectively. The white zone denotes the surf zone, and the sandbars are shown in gray color. Red shading indicates the berm, with thicker shading denoting faster berm recovery.

Figura 4.4.2. Representación esquemática de los patrones estacionales de circulación basados en la direccionalidad media del oleaje: (A) verano–otoño, (B) invierno y (C) primavera. Las flechas azules y rojas representan las corrientes de marea de vaciante y creciente, respectivamente. Las áreas de acreción rápida, acreción lenta y erosión están marcadas con los símbolos "+", “+/-” y "–", respectivamente. La zona blanca indica la zona de rompiente, y las barras de arena se muestran en color gris. El sombreado rojo indica la berma, siendo más intenso donde se observa una recuperación más rápida de la berma.

Although efforts were made to simulate nearshore circulation using a validated numerical model, the study has several limitations that could not be addressed. The model did not incorporate wind-driven currents, which may affect the accuracy of predicted current directionality, particularly during high-energy events. Future simulations should include wind stress, as previous studies (Reniers and Battjes, 1997) have highlighted its significant role in alongshore current dynamics.

The offshore forcings used in the model applied at 40 m depth were derived from ADCP measurements at a shallower depth of 20 m. To better capture the nearshore hydrodynamics, two key adjustments were implemented: (1) a 1.5% reduction in the tidal signal at the northern boundary, and (2) the implementation of a spatially varying directional wave spectrum at the offshore boundary. These modifications improved the model's ability to reproduce tidal-driven longshore flows, which is particularly relevant in embayed systems where tidal waves interact with complex morphologies (Hegeena and Canestrelli, 2021; Carbajal and Pohlmann, 2004). Despite the overall agreement between the model outputs and measurements, some discrepancies remain. The model slightly overestimates wave directionality in the northern section, likely due to the absence of spatially distributed directional wave data at the offshore boundary. Moreover, while XBeach simulations suggest current magnitudes of > 1 m/s at the headland, these values are clearly overestimated. For comparison, Mouragues et al. (2022), reported velocities of up to 0.7 m/s at 12 m depth near the headland (800 m away). Therefore, while the simulated circulation patterns are acceptable, future adjustments to bottom friction coefficients would be recommended to better represent current magnitudes.

4.5. Conclusions

La Misión exhibited distinct seasonal circulation patterns driven by the morphological configurations and varying incoming wave conditions. In the *summer and fall*, a strong alongshore current developed, constrained within the surf zone and directed upcoast due to wave directionality. The alongshore component outside the surf zone was modulated by tidal forces. In *winter*, alongshore flows were very weak due to the presence of the sandbar, and cross-shore flows dominated, particularly through gaps in the sandbar. In *spring,* offshore flows dominated through the sandbar gaps, with the alongshore flow outside the surf zone showing an upcoast trend in the central and northern sections, and downcoast in the southern beach.

Wave directionality played a critical role in shaping alongshore and cross-shore currents. Waves approaching at oblique angles (-10 degrees from the shoreline) promoted stronger alongshore currents, particularly under high-energy conditions. The southern section consistently experienced higher wave heights due to wave refraction and the convergence around the headland, leading to wave focusing. The presence of the sandbar reduced alongshore currents generated by tidal forces, with the cross-shore component becoming dominant. When the sandbar was absent, the alongshore current component was more strongly modulated by the tide.

References

Battjes, J. A., & Janssen, J. P. F. M. (1978). Energy Loss and Set-Up Due to Breaking of Random Waves. In *Coastal Engineering* (pp. 569–587). https://doi.org/10.1061/9780872621909.034

Brander, R. W., & Short, A. D. (2001). Flow Kinematics of Low-Energy Rip Current Systems. *Journal of Coastal Research*, *17*(2), 468–481. http://www.jstor.org/stable/4300197

Bruneau, N., Bertin, X., Castelle, B., & Bonneton, P. (2014). Tide-induced flow signature in rip currents on a meso-macrotidal beach. *Ocean Modelling*, *74*, 53–59. https://doi.org/https://doi.org/10.1016/j.ocemod.2013.12.002

Bryan, K., Gallop, S., Lageweg, W. I., & Coco, G. (2009). *Observations of rip channels, sandbar-shoreline coupling and beach rotation at Tairua Beach, New Zealand*. https://doi.org/10.13140/RG.2.1.3687.6241

Carbajal, N., & Pohlmann, T. (2004). Comparison between measured and calculated tidal ellipses in the German Bight. *Ocean Dynamics*, *54*(5), 520–530. https://doi.org/10.1007/s10236-004-0096-5

Castelle, B., Bourget, J., Molnar, N., Strauss, D., Deschamps, S., & Tomlinson, R. (2007). Dynamics of a wave-dominated tidal inlet and influence on adjacent beaches, Currumbin Creek, Gold Coast, Australia. *Coastal Engineering*, *54*. https://doi.org/10.1016/j.coastaleng.2006.08.007

Castelle, B., & Coco, G. (2012). The morphodynamics of rip channels on embayed beaches. *Continental Shelf Research*, *43*, 10–23. https://api.semanticscholar.org/CorpusID:140548066

Castelle, B., Scott, T., Brander, R., Mccarroll, R., Tellier, E., de Korte, E., Tackuy, L., Robinet, A., Bruno, S., & Salmi, L.-R. (2020). Wave and Tide Controls on Rip Current Activity and Drowning Incidents in Southwest France. *Journal of Coastal Research*, *95*, 769. https://doi.org/10.2112/SI95-150.1

Cohn, N., & Ruggiero, P. (2016). The influence of seasonal to interannual nearshore profile variability on extreme water levels: Modeling wave runup on dissipative beaches. *Coastal Engineering*, *115*. https://doi.org/10.1016/j.coastaleng.2016.01.006

Daly, C., Bryan, K., & Winter, C. (2014). Wave energy distribution and morphological development in and around the shadow zone of an embayed beach. *Coastal Engineering*, *93*, 40–54.

https://doi.org/10.1016/j.coastaleng.2014.08.003

Dudkowska, A., Boruń, A., Malicki, J., Schönhofer, J., & Gic-Grusza, G. (2020). Rip currents in the non-tidal surf zone with sandbars: numerical analysis versus field measurements. *Oceanologia*, *62*(3), 291–308. https://doi.org/https://doi.org/10.1016/j.oceano.2020.02.001

Gallop, S. L., Bosserelle, C., Pattiaratchi, C. B., & Eliot, I. G. (2011). Rock topography causes spatial variation in the wave, current and beach response to sea breeze activity. *Marine Geology*, *290*, 29–40. https://api.semanticscholar.org/CorpusID:129305667

Hewageegana, V. H., & Canestrelli, A. (2021). Numerical modeling of the influence of tides on cross-shore sediment dynamics of dissipative beaches under moderate wave conditions. *Continental Shelf Research*, *218*, 104381. https://doi.org/https://doi.org/10.1016/j.csr.2021.104381

Kombiadou, K., Costas, S., & Roelvink, D. J. A. (2021). Simulating Destructive and Constructive Morphodynamic Processes in Steep Beaches. *Journal of Marine Science and Engineering*, *9*. https://doi.org/10.3390/jmse9010086

Kono-Martínez, T., Ruiz de Alegria-Arzaburu, A., Mariño-Tapia, I., & Coco, G. (2023). Alongshore variability in berm and sandbar migration patterns on a highly dynamic beach. *Geomorphology*, *443*, 108935. https://doi.org/10.1016/j.geomorph.2023.108935

MacMahan, J. H., Thornton, E. B., & Reniers, A. J. H. M. (2006). Rip current review. *Coastal Engineering*, *53*(2), 191–208. https://doi.org/https://doi.org/10.1016/j.coastaleng.2005.10.009

Macmahan, J., Reniers, A., Thornton, E., Stanton, T., & Symonds, G. (2004). The Torrey Pines Rip Currents. *AGU Fall Meeting Abstracts*.

Masselink, G., & Black, K. P. (1995). Magnitude and cross-shore distribution of bed return flow measured on natural beaches. *Coastal Engineering*, *25*(3), 165–190. https://doi.org/https://doi.org/10.1016/0378-3839(95)00002-S

McCall, R., van Geer, P., Masselink, G., & Poate, T. (2014). Modelling storm response on gravel beaches using XBeach-G. *Proceedings of the ICE - Maritime Engineering*, *167*, 173–191. https://doi.org/10.1680/maen.14.00020

Mouragues, A., Bonneton, P., Castelle, B., & Martins, K. (2021). Headland Rip

Modelling at a Natural Beach under High-Energy Wave Conditions. *Journal of Marine Science and Engineering*, *9*(11). https://doi.org/10.3390/jmse9111161

Mouragues, A., Martins, K., Bonneton, P., & Castelle, B. (2022). Headland Rip Very Low Frequency Fluctuations and Surfzone Eddies During High-Energy Wave Events. *Journal of Physical Oceanography*, *52*(12), 2935–2956. https://doi.org/https://doi.org/10.1175/JPO-D-22-0006.1

Ojeda, E., & Guillén, J. (2008). Shoreline dynamics and beach rotation of artificial embayed beaches. *Marine Geology*, *253*, 51–62. https://api.semanticscholar.org/CorpusID:129592119

Reniers, A. J. H. M., & Battjes, J. A. (1997). A laboratory study of longshore currents over barred and non-barred beaches. *Coastal Engineering*, *30*(1), 1–21. https://doi.org/https://doi.org/10.1016/S0378-3839(96)00033-6

Roelvink, D. J. A., Reniers, A., van Dongeren, A., Thiel de Vries, J., Lescinski, J., & McCall, R. (2010). *XBeach Model – Description and Manual*.

Roelvink, D., Reniers, A. J. H. M., van Dongeren, A., van Thiel de Vries, J. S. M., McCall, R., & Lescinski, J. (2009). Modelling storm impacts on beaches, dunes and barrier islands. *Coastal Engineering*, *56*, 1133–1152. https://api.semanticscholar.org/CorpusID:130979044

Ruiz de Alegría-Arzaburu, A., Gracia-Barrera, A. D., Kono-Martínez, T., & Coco, G. (2022). Subaerial and upper-shoreface morphodynamics of a highly-dynamic enclosed beach in NW Baja California. *Geomorphology*, *413*, 108336. https://doi.org/https://doi.org/10.1016/j.geomorph.2022.108336

Short, A. D., & Masselink, G. (1999). Embayed and structurally controlled beaches. In *Handbook of beach and shoreface morphodynamics* (pp. 230–250). John Wiley and Sons Ltd.

Turki, I., Medina, R., Coco, G., & González, M. (2013). An equilibrium model to predict shoreline rotation of pocket beaches. *Marine Geology*, *346*, 220–232. https://doi.org/10.1016/j.margeo.2013.08.002

Vousdoukas, M. I., Almeida, L. P., & Ferreira, Ó. (2011). Modelling storm-induced beach morphological change in a meso-tidal, reflective beach using XBeach. *Journal of Coastal Research*, 1916–1920. http://www.jstor.org/stable/26482510

Wright, L. D., Chappell, J., Thom, B. G., Bradshaw, M. P., & Cowell, P. (1979). Morphodynamics of reflective and dissipative beach and inshore systems:

Southeastern Australia. *Marine Geology*, *32*(1), 105–140. https://doi.org/https://doi.org/10.1016/0025-3227(79)90149-X

Wright, L. D., & Short, A. D. (1984). Morphodynamic variability of surf zones and beaches: A synthesis. *Marine Geology*, *56*(1), 93–118. https://doi.org/https://doi.org/10.1016/0025-3227(84)90008-2

Yates, M. L., Guza, R. T., & O'Reilly, W. C. (2009). Equilibrium shoreline response: Observations and modeling. *Journal of Geophysical Research: Oceans*, *114*(C9). https://doi.org/https://doi.org/10.1029/2009JC005359

CHAPTER 5. General conclusions/ Conclusiones generales

This study focused on understanding alongshore variations during the cycle of the bar-berm system, based on morphological and hydrodynamic measurements collected over a 5-year period (2015–2020). The XBeach numerical model was used as a complementary tool to analyze the spatial variability of the nearshore circulation. The key findings based on observations are: (1) the northern beach section exhibited a quicker recovery capacity than the south through the early formation of the berm, while the south presented a rapid formation of a subtidal sandbar that remained active for a longer period throughout the seasons; and (2) the spatial variation of flows: in the north, onshore flows predominated, while in the south, offshore flows persisted for longer time.

Seasonal circulation patterns revealed two distinct zones: (1) the surfzone and (2) the zone beyond it (shoaling zone). Within the surfzone, the alongshore current was primarily controlled by the waves direction, while in the shoaling zone tidal forcing determined the flow direction—landward during flood tide and seaward during ebb tide. These tidal currents promoted sediment exchange in deeper waters (3–4 m), while cross-shore flows governed sediment deposition either landward or seaward. During summer–fall, a northward-directed alongshore current developed within the surfzone, reaching speeds up to 0.6 m/s. In contrast, in winter, alongshore flows outside the surfzone weakened, and cross-shore flows became dominant—particularly through bar discontinuities—facilitating more intense offshore sediment transport. Spring conditions exhibited a transitional pattern: moderate offshore flows through bar gaps in the south, while in the north, the absence of a bar enabled wave-driven alongshore flows within the surfzone and tide-driven flows beyond it.

Hydrodynamic variations along the beach were evident. In the northern section, the presence of an adjacent rocky outcrop resulted in lower wave heights (≈0.3 m), oblique wave incidence, and weak net onshore flows (~0.1 m/s). These conditions facilitated rapid bar attachment to the shoreline and accelerated berm recovery. In contrast, the southern section, bounded by a rocky headland, was exposed to higher wave heights (≈0.3 m) and persistent offshore flows (0.3–0.5 m/s) across most seasons. These dynamics favored the retention of the nearshore bar at depths between 2 and 3 m, delaying its attachment to the shore and contributing to shoreline retreat and a slower rate of berm recovery compared to the northern section.

Wave directionality emerged as a key driver of surfzone circulation. During the fall, waves predominantly from the southwest induced northward alongshore currents, promoting faster berm recovery. In winter, dominant westerly wave directions coincided with strong offshore flows; however, when wave approach shifted to the northwest, southward currents developed. In spring, the continued dominance of southwest waves generated northward currents.

These findings highlight the complex interplay between wave directionality, wave energy, tidal forcing, and morphological features such as headlands in controlling sediment transport and coastal morphology. Understanding the spatial and seasonal variability of hydrodynamic processes is essential for improving predictions of beach erosion and recovery. Even small spatial differences can lead to significantly different morphological responses. This knowledge provides a valuable framework for informing beach management strategies and assessing and planning coastal resilience in the face of future climate change and sea-level rise scenarios.

Este trabajo se enfocó en las variaciones a lo largo de la playa durante el ciclo de formación del sistema barra-berma, basándose en mediciones morfológicas e hidrodinámicas recolectadas durante un periodo de cinco años (2015-2020). Se utilizó el modelo numérico XBeach como herramienta complementaria para analizar la variabilidad espacial de la hidrodinámica. Los hallazgos clave fueron los siguientes: (1) la sección norte de la playa mostró una mayor capacidad de recuperación mediante la formación temprana de la berma, mientras que la sección sur mostró una rápida formación de la barra submareal, la cual permaneció activa durante un periodo más prolongado a lo largo de las distintas estaciones; y (2) se identificó una variación espacial en los patrones de corrientes: en el norte predominaron los flujos hacia la costa, mientras que en el sur persistieron flujos hacia mar adentro por mayor tiempo.

Los patrones estacionales de la circulación revelaron dos zonas principales de dinámica diferente: (1) dentro de la zona de rompiente y (2) fuera de ella en la zona de asomeramiento. En la primera, la dirección de la componente longitudinal de la corriente estuvo influenciada por la direccionalidad del oleaje incidente, mientras que en la segunda el forzamiento de marea determinó la dirección del flujo: costa arriba durante el flujo y costa abajo en el reflujo. Estas corrientes de marea facilitaron el intercambio de sedimentos en zonas más profundas (3 – 4 m), mientras que los flujos transversales influyeron en la deposición de sedimentos tanto hacia la línea de costa como mar adentro.

La temporada de verano-otoño se caracterizó por el desarrollo de una corriente longitudinal confinada dentro de la zona de rompiente y orientada hacia el norte, con velocidades de hasta 0.6m/s. En contraste, durante el invierno, los flujos longitudinales fuera de la rompiente se debilitaron, y predominaron los flujos transversales, especialmente a través de las discontinuidades en la barra, lo que facilitó un transporte de sedimentos más intenso hacia mar adentro. La primavera mostró una combinación de patrones, con flujos moderados hacia mar adentro a través de las discontinuidades en la barra al sur, mientras que en el norte, la ausencia de la barra favoreció la formación de flujos longitudinales, dominados por el oleaje dentro de la rompiente y por la marea fuera de ella en la zona de asomeramiento.

Las variaciones hidrodinámicas a lo largo de la playa fueron evidentes. La sección norte, influenciada por la presencia de un saliente rocoso adyacente, presentó oleaje de menor altura (≈0.3m), con incidencia oblicua, y flujos netos débiles hacia la costa (~0.1 m/s). Esto favoreció una rápida unión de la barra a la línea de costa y una recuperación acelerada de la berma. En contraste, la sección sur, limitada por una saliente rocosa, experimentó mayores alturas de ola (≈0.3m) y flujos sostenidos hacia mar adentro (0.3–0.5 m/s) durante la mayoría de las temporadas. Estas condiciones favorecieron la retención de la barra en profundidades de entre 2 y 3 m, retrasando la unión de la barra a la costa, y contribuyendo al retroceso de la línea costera, así como a una recuperación más lenta de la berma en comparación con la sección norte.

La direccionalidad del oleaje se destacó como un factor clave en el control de la circulación dentro de la zona de rompiente. Durante el otoño, el oleaje proveniente predominantemente del suroeste indujo corrientes a lo largo de la costa hacia el norte, lo que favoreció una recuperación acelerada de la berma. En invierno, las direcciones dominantes del oeste coincidieron con flujos fuertes hacia mar adentro; sin embargo, cuando el oleaje fue del noroeste, se observaron corrientes hacia el sur. En primavera, la direccionalidad predominante del suroeste generó corrientes con direccionalidad hacia el norte.

En conjunto, estos resultados subrayan la complejidad de las interacciones locales entre la direccionalidad del oleaje, la energía del oleaje, el forzamiento de marea y elementos morfológicos como las salientes rocosas, en el control del transporte de sedimentos y la evolución morfológica de la costa. Comprender la variabilidad espacial y estacional de los procesos hidrodinámicos resulta fundamental para mejorar las predicciones sobre erosión y recuperación de la playa, ya que pequeñas diferencias espaciales pueden derivar en respuestas morfológicas significativamente distintas. Este conocimiento proporciona un marco valioso para informar estrategias de gestión de playas, así como la evaluación y planificación de la resiliencia ante escenarios futuros de cambio climático y aumento del nivel del mar.

Appendix A. XBeach model description

A.1. System coordinates

The XB coordinate system is relative to the global coordinates (X_w, Y_w) defined horizontally and vertically from the origin, and α defines the angle of rotation clockwise or counterclockwise of the X_w axis (see Figure A.1.1). The grid applied by XB is staggered rectangular, non-equidistant, where depth levels (bathymetry), water, and particle concentrations (sediments) are defined at the cell centers, while velocities are defined on the faces of the grid, thus defining a staggered Arakawa-C grid (Arakawa and Lamb, 1977). The magnitude of velocity (V) and sediment transport are calculated by determining the velocity components u and v, which are coupled to sediment load and suspension equations, defining sediment concentration at the cell centers. The calculation process is similar for wave processes, considering wave-current interaction through radiation stresses and wave breaking.

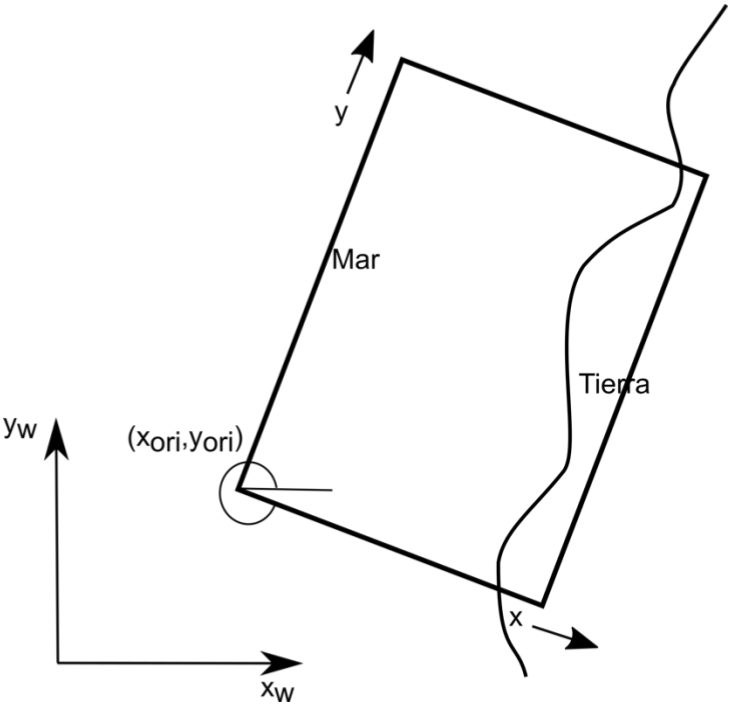

Figure A.1. 1 XBeach coordinate system relative to the origin (Xori, Yori).

A.2. Wave action equation

First, the model solves the wave action balance equation (Eq. 12). Where the wave energy varying in space and time (x, y, θ, t) propagating at a phase velocity (c) for each component is equal to the amount of energy dissipated by wave breaking (D_w) and bottom friction (D_f) represented by an intrinsic frequency (σ):

$$\frac{\partial A}{\partial t} + \frac{\partial c_x A}{\partial x} + \frac{\partial c_y A}{\partial y} + \frac{\partial c_\theta A}{\partial \theta} = -\frac{D_w + D_f}{\sigma} \quad (12)$$

Here, S_w represents the wave energy density and based on linear wave theory, it can be represented as the sum of potential and kinetic energy:

$$A(x, y, t, \theta) = \frac{S_w(x, y, t, \theta)}{\sigma(x, y, t)} \quad (13)$$

Here, ρ represents the density of seawater (1024 Kg m^{-3}), g the gravitational acceleration (9.81 m s^{-2}), and the wave amplitude.

$$E_w(x,y,t) = \int_0^{2\pi} S_w(x,y,t,\theta)\, d\theta$$

$$E_w = \frac{1}{2}\rho g a^2 \tag{14}$$

Referring to Eq. 8, the wave velocity components can be derived from the dispersion relationship obtained from linear wave theory, where the phase velocity (c) and group velocity (c$_g$) are defined as:

$$c = \frac{\sigma}{k}$$

$$c_g = \frac{\partial \sigma}{\partial k} = \frac{1}{2}\left[1 + \frac{2kh}{\sinh 2kh}\right] c \tag{15}$$

Where k represents the wave number. The propagation velocity for the "x" and "y" components in the presence of a current can be described in geographical space as follows:

$$c_x = c_g \cos(\theta) + u^L$$

$$c_y = c_g \operatorname{sen}(\theta) + v^L \tag{16}$$

The propagation velocity in the direction θ is obtained as follows:

$$c_\theta = \frac{\sigma}{senh2kh}\left(\frac{\partial h}{\partial x} sen(\theta) - \frac{\partial h}{\partial x}\cos(\theta)\right) + cos\theta\left(sen(\theta)\frac{\partial u}{\partial x} - \cos(\theta)\frac{\partial u}{\partial y}\right)$$
$$+ sen\theta\left(sen(\theta)\frac{\partial v}{\partial x} - \cos(\theta)\frac{\partial v}{\partial y}\right) \tag{17}$$

being *h* the depth. The first term on the right represents bottom refraction, while the last two represent current refraction. Wave-current interaction involves an exchange of energy between both processes; thus, it is necessary to correct the wave number k using eikonal equations:

$$k_x = k_x^{n-1} + k_x^{\sim}$$

$$k_y = k_y^{n-1} + k_y^{\sim} \tag{18}$$

where n^{-1} refers to the wave number prior to the time step, and $k_x^{\sim}$ and $k_y^{\sim}$ represent the wave number corrections in the x and y directions, respectively. The correction terms are determined by a second set of eikonal equations.

$$\frac{\partial k_x}{\partial t} + \frac{\partial \omega}{\partial x} = 0 \tag{19}$$

$$\frac{\partial k_y}{\partial t} + \frac{\partial \omega}{\partial y} = 0 \tag{20}$$

the subscripts denote the direction of the components of the wave vector, and ω represents the absolute radial frequency. The wave number (k) can be obtained as follows:

$$k = \sqrt{k_x^2 + k_y^2} \tag{21}$$

While the absolute radial frequency is given by:

$$\omega = \sigma + k_x u^L + k_y v^L \tag{22}$$

It is important to mention that XBeach does not consider wave generation from wind (S_{in}), so it is discarded in the simulation.

A.3. Wave dissipation

XBeach takes into account three processes contributing to wave dissipation: wave breaking (D_w), bottom friction (D_f), and vegetation friction (D_v); however, in this work, the latter will not be considered due to the objectives of the study. When waves experience shoaling, they tend to destabilize due to amplitude growth and break. It contains five parametrizations for wave breaking that have been studied through experiments in wave flumes. Three parametrizations are employed when using non-stationary wave input, while the other two are used for stationary wave cases. This work will only focus on irregular waves, so only the non-stationary wave breaking parameters will be described; for more information on the other parametrizations, the manual can be consulted.

Roelvink (1993) proposed the following formulation for the wave energy dissipation coefficient:

$$\overline{D_w} = \frac{\alpha}{T_{rep}} Q_b E_w \qquad (23)$$

where Q_b represents the fraction of waves breaking, α represents the wave dissipation coefficient, T_{rep} is the representative period, and E_w is the total wave energy. Q_b is determined as follows:

$$Q_b = 1 - exp\left(\left(-\frac{H_{rms}}{H_{max}}\right)^n\right) \qquad (24)$$

being n a free parameter rewritten in terms of energy by (Klopman, 1989), Hrms is the root mean square wave height, and H_{max} is the maximum wave height, obtained as follows:

$$H_{rms} = \sqrt{\frac{8E_w}{\rho g}}$$

$$H_{max} = \gamma \cdot (h + \delta H_{rms}) \qquad (25)$$

Here, γ represents the breaking index where 0.55 is the default value, while δH_{rms}

represents the wave height fraction. Finally, E_w is obtained from Equation (25). However, there are other possible ways to calculate breaking dissipation (eq. 23). For example, a variant of equation (23) includes the ratio H_{rms} / h, where h is the depth:

$$\overline{D_w} = \frac{\alpha}{T_{rep}} Q_b E_w \frac{H_{rms}}{h} \quad (26)$$

Equation (26) is more suitable than equation (23) when wave breaking depends more on depth than maximum height. On the other hand, Daly et al. (2010) proposed two solutions for Q_b where they establish that wave breaking occurs when the wave height exceeds a critical limit (γ), and this cannot occur if it does not exceed the required limit:

$$\begin{cases} Q_b = 1 \; si \; H_{rms} > \gamma h \\ Q_b = 0 \; si \; H_{rms} < \gamma h \end{cases} \quad (27)$$

The total wave dissipation due to breaking is distributed proportionally over the directions by:

$$D_w(x,y,t,\theta) = \frac{S_w(x,y,t,\theta)}{E_w(x,y,t)} \overline{D}_w(x,y,t) \quad (28)$$

When waves are generated, they possess momentum and direction parallel to the wave propagation direction. However, when waves break, they generate turbulence, implying a forcing that propagates in all directions of the system, known as radiation stresses, which interact with the flow of the system and are defined according to their component (using linear wave theory) as follows:

$$S_{xx,w}(x,y,t) = \int \left(\frac{c_g}{c} (1 + cos^2\theta) - \frac{1}{2} \right) S_w \, d\theta$$

$$S_{xy,w}(x,y,t) = S_{yx,w}(x,y,t) = \int sen\theta cos\theta \left(\frac{c_g}{c} S_w \right) \, d\theta$$

$$S_{yy,w}(x,y,t) = \int \left(\frac{c_g}{c}(1 + sen^2\theta) - \frac{1}{2}\right) S_w \, d\theta \qquad (29)$$

Where S_{xx} is the longitudinal component, S_{yy} is the transverse component, and S_{xy} or S_{yx} are the shear radiation stresses.

A.4. Bottom friction dissipation

When waves interact with the bottom, they lose energy due to dissipation. Jonsson (2011) found a mathematical expression to parameterize this effect using a coefficient f_w:

$$D_f = \frac{2}{3\pi} \rho f_w \left(\frac{\pi H_{rms}}{T_{m01} \sinh kh}\right)^3 \qquad (30)$$

where f_w is the wave friction coefficient and T_{m01} is the mean period defined by the zeroth and first moments of the wave spectrum. Some authors have found that this coefficient has particular importance in areas where the bottom has high roughness (van Dongeren et al., 2013; Quataert et al., 2015). XBeach applies this friction coefficient to the wave action equation (eq. 12), and it is not related to bottom friction, cf, in the flow equation.

A.5. Energy balance in the breaker zone

Wave breaking transmits momentum to the domain, and this energy is represented by the wave breaking energy balance equation (eq. 31), establishing that the latter will propagate throughout the domain being dissipated by wave breaking again (D_w) and dissipation of the same (D_r):

$$\frac{\partial S_r}{\partial t} + \frac{\partial c_x S_r}{\partial x} + \frac{\partial c_y S_r}{\partial y} + \frac{\partial c_\theta S_r}{\partial \theta} = D_w - D_r \qquad (31)$$

In the above equation, the energy from breaking in each direction is represented by Sr, while Dr according to Reniers et al. (2004) is obtained from the following expression:

$$\overline{D}_r = \frac{2g\beta_r E_r}{c} \tag{32}$$

Where $\overline{D_r}$ is the average breaking energy dissipation, β_r is the breaker slope, c is the phase velocity (eq. 4), and E_r is the breaking energy density. The total breaking energy dissipation is distributed proportionally over the wave directions by:

$$D_r(x, y, t, \theta) = \frac{S_r(x,y,t,\theta)}{E_r(x,y,t)} \overline{D_r}(x, y, t) \tag{33}$$

Where the contribution of breaking energy for each component of the radiation stresses is given by:

$$S_{xx,r}(x, y, t) = \int cos^2\theta S_r \ d\theta$$

$$S_{xy,r}(x, y, t) = S_{yx,r}(x, y, t) = \int sen\theta cos\theta S_r \ d\theta$$

$$S_{yy,r}(x, y, t) = \int sen^2\theta S_r \ d\theta \tag{34}$$

Taking into account the radiation stresses determined in the wave action balance equation (eq. 12) and those of wave breaking (eq. 31), the total radiation stress for each component can be expressed as follows:

$$F_x(x, y, t) = -\left(\frac{\partial S_{xx,w} + S_{xx,r}}{\partial x} + \frac{\partial S_{xy,w} + S_{xy,r}}{\partial y}\right)$$

$$F_y(x, y, t) = -\left(\frac{\partial S_{xy,w} + S_{xy,r}}{\partial x} + \frac{\partial S_{xy,w} + S_{yy,r}}{\partial y}\right) \tag{35}$$

Where each directional wave component (x, y, θ) in the presence of a current will have a propagation velocity in a geographical space.

A.6. Shallow water equations

The equations that XBeach uses to simulate variations in water surface and flow, taking into account waves and currents induced by waves, are as follows:

$$\frac{\partial u^L}{\partial t} + u^L \frac{\partial u^L}{\partial x} + v^L \frac{\partial u^L}{\partial y} - f v^L - v_h \left(\frac{\partial^2 u^L}{\partial x^2} + \frac{\partial^2 u^L}{\partial y^2} \right) = \frac{\tau_{sx}}{\rho h} - \frac{\tau_{bx}^E}{\rho h} - g \frac{\partial \eta}{\partial x} + \frac{F_x}{\rho h}$$

$$\frac{\partial v^L}{\partial t} + u^L \frac{\partial v^L}{\partial x} + v^L \frac{\partial v^L}{\partial y} + f u^L - v_h \left(\frac{\partial^2 v^L}{\partial x^2} + \frac{\partial^2 v^L}{\partial y^2} \right) = \frac{\tau_{sy}}{\rho h} - \frac{\tau_{by}^E}{\rho h} - g \frac{\partial \eta}{\partial y} + \frac{F_y}{\rho h}$$

$$\frac{\partial \eta}{\partial t} + \frac{\partial h u^L}{\partial x} + \frac{\partial h v^L}{\partial y} = 0 \qquad (36)$$

Here, τ^E_{bx}, τ^E_{by} are the bed shear stresses, τ_{sx}, τ_{sy} are the components of the wind stress on the sea surface, η is the sea level, F_x, F_y (Eq. 35) are the components of wave-induced radiation stresses, v_h is the horizontal viscosity, and f is the Coriolis parameter.

To account for the flow induced by waves and the return flow, the velocity of the average depth is used (Andrews and McIntyre, 1978; Walstra et al., 2000). The momentum and continuity equations are formulated in terms of Lagrangian velocity (v^L), which is defined as the distance traveled by a fluid particle in one wave period divided by the wave period. This velocity is related to the Eulerian velocity by:

$$u^L = u^E + u^S \; ; \; v^L = v^E + v^S$$

$$u^E = u^L - u^S;\ v^E = v^L - v^S \tag{37}$$

where u^s, v^s represent the Stokes drift in the x and y axes, respectively (Philips, 1977)

$$u^S = \frac{E_w cos\theta}{\rho hc};\ v^S = \frac{E_w sen\theta}{\rho hc} \tag{38}$$

A.7. Bottom shear stress

The bottom friction exerted on the flow is determined by the Eulerian and orbital velocities, which depend on the roughness of the seabed, using the approximation proposed by Ruessink et al. (2001).

$$\tau_{bx}^E = c_f \rho u_E \sqrt{(1.16 u_{rms})^2 + (u_E + v_E)^2}$$

$$\tau_{by}^E = c_f \rho v_E \sqrt{(1.16 u_{rms})^2 + (u_E + v_E)^2} \tag{39}$$

where cf represents the flow friction coefficient. This coefficient is typically an order of magnitude smaller than f_w in coral reef areas (van Dongeren et al., 2013; Quataert et al., 2015). The orbital velocity (u_{rms}) is obtained from linear wave theory using the following expression:

$$u_{rms} = \frac{1}{\sqrt{2}} \frac{\pi H_{rms}}{T \sinh(kd)} \tag{40}$$

A.8. References

Andrews, D. G. & Mcintyre, M. E. (1978). An exact theory of nonlinear waves on a Lagrangian-mean flow. *Journal of Fluid Mechanics*, *89*, 609-646.

Arakawa, A. & Lamb, V. R. (1977), *Methods of Computational Physics*, 173-265 pp., New York: Academic Press.

Daly, C. , Roelvink, D. , van Dongeren, A. R. & McCall, R. T. (2010), Short wave breaking effects on low frequency waves, Coastal Engineering Proceedings, 1(32), waves.20.

Jonsson, I. G. (2011). Wave boundary layers and friction factors, paper presented at Proceedings 10th Coastal Engineering Conference, Tokyo, pp. 127-148.

Klopman, G., and M.J.F. Stive. (1989). Extreme waves and wave loading in shallow water. Coastal Engineering Proceedings, 1(32), waves.63. doi: http://dx.doi.org/10.9753/icce.v32.waves.63

Philips, O. M. (1977). The dynamics of the upper ocean. 366 pp., Cambridge University Press.

Quataert, E., Storlazzi, C. , van Rooijen, A. , Cheriton, O. & van Dongeren, A. (2015). The influence of coral reefs and climate change on wave-driven flooding of tropical coastlines, Geophysical Research Letters (42), 6407-6415.

Reniers, A., Roelvink, D. & Thornton, E. B. (2004). Morphodynamic modeling of an embayed beach under wave group forcing. Journal of Geophysical Research, 109(C01030), 22.

Roelvink, D. (1993). Dissipation in random wave group incident on a beach., Coastal Engineering, 19, 127-150.

van Dongeren, A., Lowe, R. , Pomeroy, A. , Minh-Trang, D. , Roelvink, D. , Symonds, G., et al. (2013). Numerical modeling of low-frequency wave dynamics over a fringing coral reef. Coastal Engineering, 73, 178-190.

Walstra, D. J. R., Roelvink, D. & Groeneweg, J. (2000). Calculation of wave-driven currents in a 3D mean flow model, paper presented at 27th International Conference on Coastal Engineerring, pp. 1050-1063, Sydney, Australia.

Appendix B. XBeach model input parameters

XBeach requires the input of a set of parameters related to the bathymetry, waves, flow, boundary and tides. In addition, model run time and output variables need to be specified. All these parameters will be input into the model through the params.txt file, and these will be explained in the following Sections.

B.1 Bathymetric Grid

Xbeach requires the input of a file (.grd) wich specifies the elevation of the model bathymetry, and the characteristics of the grid as shown in Table B.1.

Table B,1 Grid input parameters fo Xbeach

nx	number of cells in x direction
ny	number of cells in y direction
xori	x coordinate origin
yori	y coordinate origin
alpha	grid orientation
vardx	non-equidistant grid
depfile	file contains bathymetry
xfile	x grid file for bathymetry
yfile	y grid file for bathymetry
posdwn	vertical elevation defined negative downwards
thetamin	lower directional limit
thetamax	upper directiona limit
dtheta	directional resolution

B.2 Wave input

The sequence of wave parameters required by XBeach are specified in Table B.2. The model allows the boundary waves to be input in the stationary or non-stationary form. It is also possible to use a sequence of varying spectra to compute boundary conditions (described by Van Dongeren et al. (2003)), and within the instat options the raw wave data are given the option to be fitted into a JONSWAP spectra.

Table B.2.Wave input parameters for XBeach

instat	time varying wave boundary conditions
bcfile	raw wave data
break	breaker model
roller	include roller energy
beta	breaker slope coefficient
gamma	wave breaking dissipation coefficient
alpha	wave breaking dissipation coefficient
nspectrumloc	Number of directional wave spectrum at boundary

B.3 Boundary input

The model boundary conditions are defined specifying the front, back, left and right limits as indicated in Table B.3.

Table B.3. XBeach input parameters to define model boundaries

front	offshore boundary condition
back	land boundary condition
left	north boundary condition
right	south boundary contidion

B.4 Tide input

The tidal input parameters within Xbeach are shown in Table B.4

Table B.4. Xbeach input parameters to define the characteristics of the tides

tideloc	number of model corners of tidal input time series
zs0file	input file with tidal data

B.5 Time input/output

The model parameters to define simulation input and output times and time intervals to safe outputs are specified in B.5.

Table B.5. Xbeach input parameters to define starting and finishing run times

tstop	stop time simulation

tstart	start time simulation
tintg	time interval global variables
tintp	tine interval point variables

B6. Output options

The ouput variables for the model simulatios is specified in Table B.6.

Table B.6. An example of model ouput options

nglobalvar	number of output variables
zs	water surface
ue	x component eulerian velocity
ve	y component eulerian velocity

B.7 Xbeach model input parameters file example

```
%%%%%%%%%%%%%%%%%%%%%%%%%%%%%%%%%%%%%%%%%%%%
%%%%%%%%%%%%%%%%%%%%%%%%%%%%%%%%%%%%%%
%%% XBeach parameter settings input file                    %%%
%%%                                                     %%%
%%% date:     22-feb-2024 18:11:43                       %%%
%%% function: xb_write_params                            %%%
%%%%%%%%%%%%%%%%%%%%%%%%%%%%%%%%%%%%%%%%%%%%
%%%%%%%%%%%%%%%%%%%%%%%%%%%%%%%%%%%%%%

%%%        Flow        boundary        condition        parameters
%%%%%%%%%%%%%%%%%%%%%%%%%%%%%%%%%%%%%%%%%%

left          = neumann
right         = neumann


%%%                                                          General
%%%%%%%%%%%%%%%%%%%%%%%%%%%%%%%%%%%%%%%%%%%%
%%%%%%%%%
```

```
wavemodel    = surfbeat
lat = 32

%%%                              Grid                              parameters
%%%%%%%%%%%%%%%%%%%%%%%%%%%%%%%%%%%%%%%%%%%
%%%%%%%%%%%%%%%%%

gridform     = delft3d
xyfile        = 4100x700_derefinedx5.grd
depfile      = Bati21SEP_derefinedx4v5smooth_vfinal_slope.dep
posdwn       = -1
alfa         = 0
thetamin     = 180
thetamax     = 280
dtheta       = 20
thetanaut    = 1
dtheta_s     = 10
%%%                              Model                              time
%%%%%%%%%%%%%%%%%%%%%%%%%%%%%%%%%%%%%%%%%%%
%%%%%%%%%%%%%%

CFL          = 0.7
tstop        = 864000


%%%                              Physical                              processes
%%%%%%%%%%%%%%%%%%%%%%%%%%%%%%%%%%%%%%%%%%%
%%%%%%%%%%%%%%

sedtrans     = 0
morphology   = 0

%%%                              Physical                              constants
%%%%%%%%%%%%%%%%%%%%%%%%%%%%%%%%%%%%%%%%%%%
%%%%%%%%%%%%%%

g            = 9.8100
rho          = 1025

%%%                              Initial                              conditions
%%%%%%%%%%%%%%%%%%%%%%%%%%%%%%%%%%%%%%%%%%%
%%%%%%%%%%%%%%

tideloc            = 4
zs0file          = tide_sep21_xbeach.txt

%%%          Wave          boundary          condition          parameters
%%%%%%%%%%%%%%%%%%%%%%%%%%%%%%%%%%%%%%%%%
wbcversion    = 3
```

```
nspectrumloc     = 16
instat       = 41
bcfile       = loclist.txt
dtbc         = 2
wavint       = 600
lateralwave  = wavecrest


%%% Wave breaking parameters %
fw = 0
%%%%                              Bed                              composition
parameters%%%%%%%%%%%%%%%%%%%%%%%%%%%%%%%%%%%%%
%%%%%%

  D50 =.00025

%%%                              Output                              variables
%%%%%%%%%%%%%%%%%%%%%%%%%%%%%%%%%%%%%%%%%%%%%%%%
%%%%%%%%%%%%%%%%

outputformat = netcdf
tintg       = 3600
tintm     = 1024
tintp = 1
tstart      = 0
taper       = 100

npoints = 17
509838           3550941
510800    3550900
510687           3550540
510630           3551431
510640           3552243
509000    3550600
509000           3551770
509000           3552270
509000    3551500
509200    3551500
509400    3551500
509600    3551500
509800    3551500
510000    3551500
510200    3551500
510400    3551500
510600    3551500
510800    3551500

nglobalvar   = 15
zs
```

```
H
ue
ve
As
cgx
cgy
taubx
tauby
Sxx
Sxy
Syy
Fx
Fy
thetamean

npointvar = 14
zs
H
ue
ve
L1
taubx
tauby
Sxx
Sxy
Syy
Fx
Fy
thetamean
sigm

nmeanvar    = 15
zs
H
ue
ve
hh
cgx
cgy
L1
taubx
tauby
Sxx
Sxy
Syy
Fx
```

Appendix C. XBeach sensitivity analysis

C.1 Tideloc test parameter

The XBeach simulations demonstrated moderate to good agreement (R>0.4; see Table C.1.1) in reproducing near-surf zone time series for H_s and T_p in the southern and central sections (see Figure C.1.1) using default parameters (see Table C.1.1). However, performance in the northern section was poor (R < 0.4), particularly in capturing wave directionality. Additionally, XBeach struggled to accurately reproduce current directionality, especially for the alongshore component (Figure C.1.2). To address this issue, the **tideloc** parameter was adjusted from 2 to 4, which, according to the XBeach Manual (Roelvink et al., 2010), this adjustment enhances the generation of tidal alongshore currents. However, here this modification did not improve the statistical performance for alongshore currents (see Table C.1.2).

Table C.1. 1 Statistical results using default model parameters

Default									
STATISTIC TEST	**RSME**			**Bias**			**R**		
Variable/Site	**S**	**C**	**N**	**S**	**C**	**N**	**S**	**C**	**N**
Hs (m)	0.2	0.2	0.2	0.2	0.1	0.1	0.8	0.8	0.7
Tp (s)	0.4	0.6	1.1	-0.1	-0.1	-0.1	0.7	0.6	0.4
Dir (o)	6.2	4.4	15.7	3.2	4.4	3.2	0.5	0.5	0.6
u (m/s)	0.1	0.0	0.1	0.0	0.0	0.0	0.4	0.3	0.2
v (m/s)	0.1	0.1	0.1	0.0	0.0	0.0	0.3	0.2	0.1

Table C.1. 2 Statistical results modifying tideloc = 4.

Tideloc = 4									
STATISTIC TEST	**RSME**			**Bias**			**R**		
Variable/Site	**S**	**C**	**N**	**S**	**C**	**N**	**S**	**C**	**N**
Hs (m)	0.2	0.2	0.2	0.2	0.1	0.1	0.8	0.8	0.7
Tp (s)	0.4	0.6	1.1	-0.1	-0.1	-0.1	0.7	0.6	0.4
Dir (o)	6.2	4.4	15.7	3.1	4.3	3.2	0.5	0.5	0.6
u (m/s)	0.1	0.0	0.1	0.0	0.0	0.0	0.4	0.3	0.2
v (m/s)	0.1	0.1	0.1	0.0	0.0	0.0	0.3	0.2	0.1

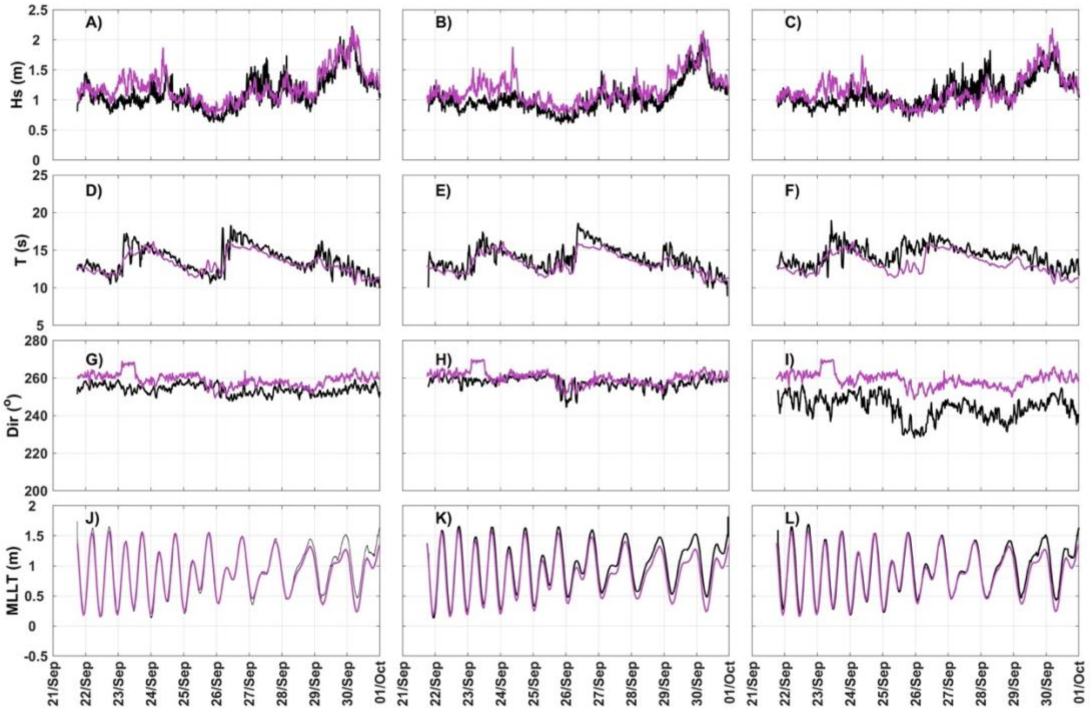

Figure C.1. 1 Modeled (purple lines) vs measured (black lines) H_s, T_p, Dir and Tidal level (top to bottom) for the near-surfzone ADCPs in the South (A, D, G, J), Center (B, E, H, K) and North (C, F, I, L), using default model parameters.

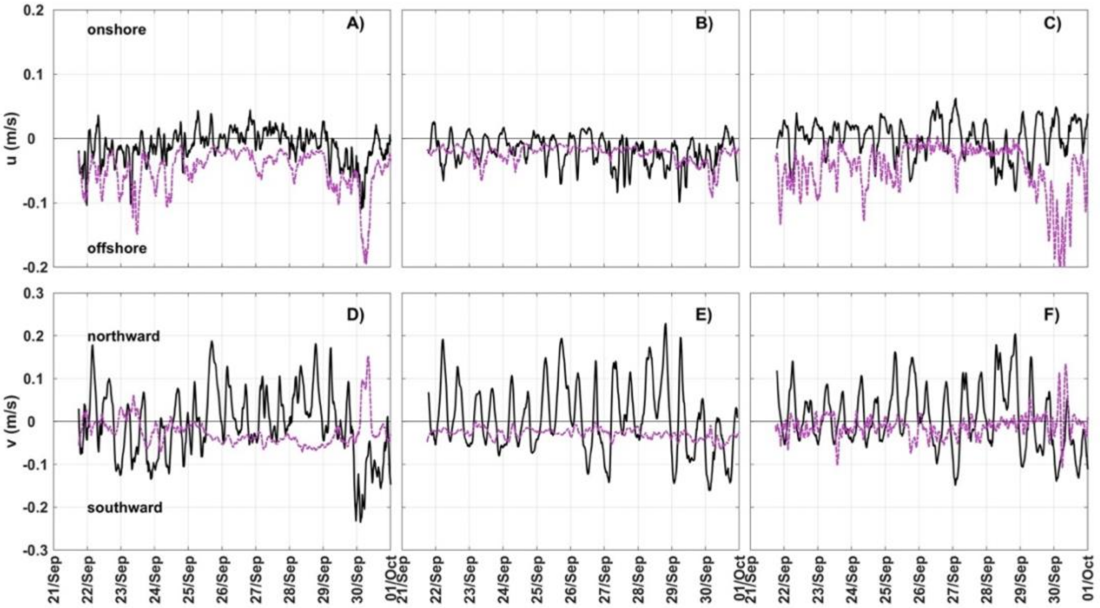

Figure C.1. 2. Modeled (purple lines) vs measured (black lines) cross-shore (U) and alongshore (V) flow components for the southern (A and D), central (B and E) and northern (C, F) near-surfzone ADCP locations using default model parameters.

C.2 Tidal signal reduction

To better reproduce alongshore currents, the tidal signal at the northern boundary was reduced by 5%, 2%, and 1.5% from the original tidal values. This adjustment was necessary due to the model's inability to input the tidal signal through harmonic components, which is equivalent to altering the harmonic amplitude (Hewageegana and Canestrelli, 2021) specially in locations where the tide can interact with the coastal geometries such the embayment (Carbajal and Pohlmann, 2004). The northern boundary was selected because reducing the tidal signal at the southern boundary resulted in poor performance, as the alongshore component tends to dominate southward of La Misión (Figure C.2.1).

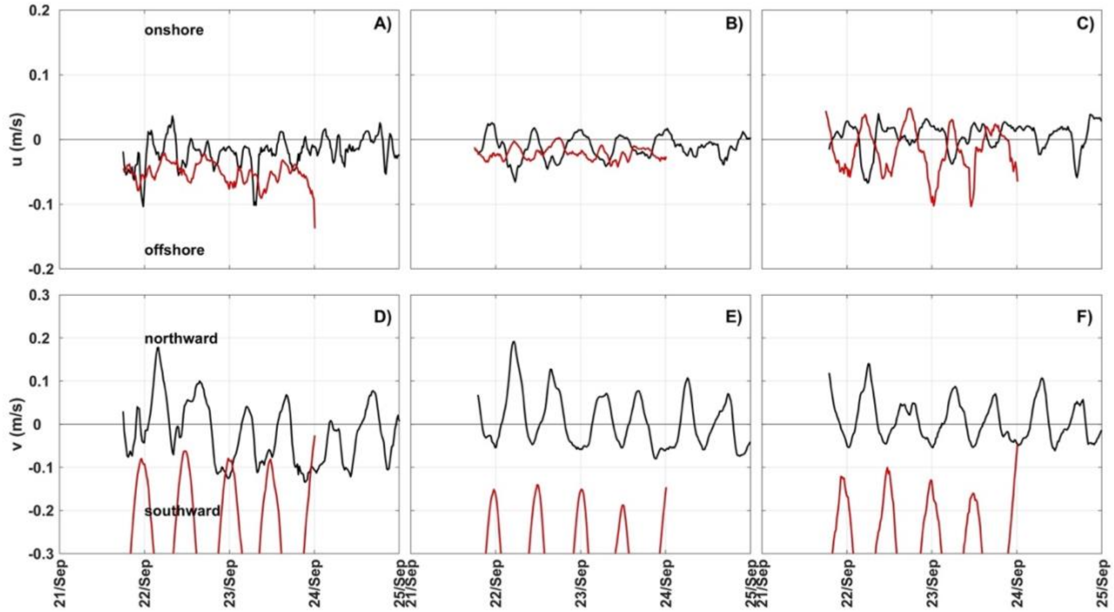

Figure C.2. 1. Modeled (red) vs measured (black lines) cross-shore (U) and alongshore (V) flow components for the southern (A and D), central (B and E) and northern (C, F) near-surfzone ADCP locations reducing the tidal signal (5%) on the southern boundary.

The tidal reduction did not improve the wave integral parameters (Table C.2.1, Table C.2.2 and Table C.2.3, Figure C.2.2). However, it significantly enhanced the alongshore current results (Figure C..2.3) compared to solely modifying the tideloc parameter (Table C.1.2). A 5% reduction (blue line) led to an overestimation of alongshore currents, while the 2% reduction showed reasonable results. Nonetheless, the 1.5% reduction yielded the best performance based on RMSE, Bias close to 0, and correlation (R > 0.4), making it the selected configuration (Figure C.2.4).

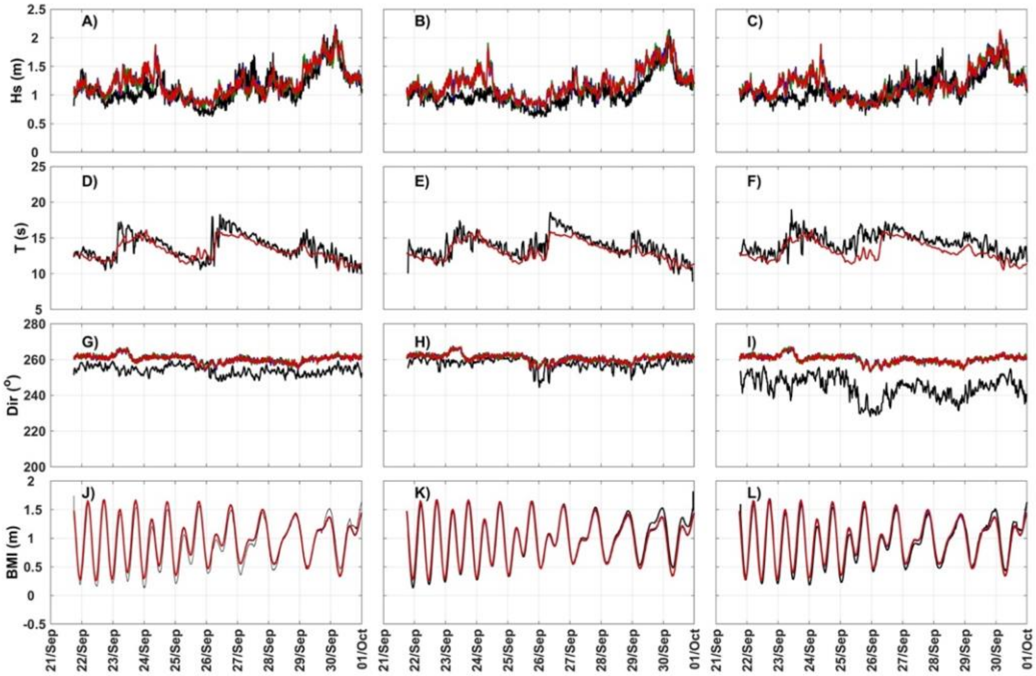

Figure C.2. 2 Modeled (color lines) vs measured (black lines) H_s, T_p, Dir and Tidal level (top to bottom) for the offshore ADCP location (left; A, E, I, M) and near-surfzone ADCPs in the South (B, F, J, N), Center (C, G, K, O) and North (D, H, L, P) using tideloc=4 and 5% (blue), 2% (green) and 1.5% (red) of tidal signal reduction in the northern boundary.

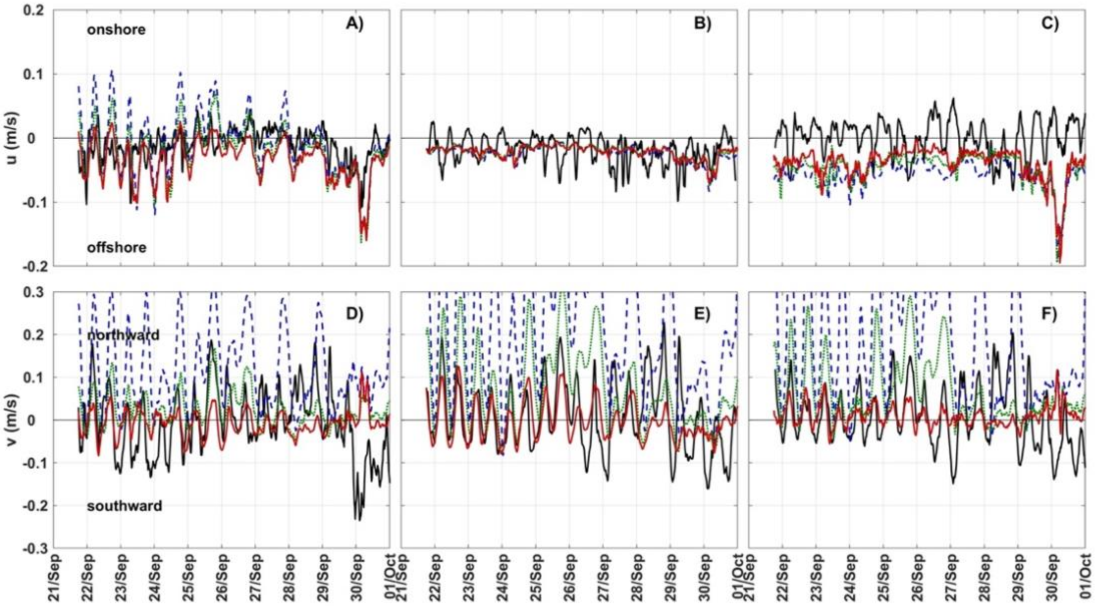

Figure C.2. 3. Modeled (blue lines) vs measured (black lines) cross-shore (U) and alongshore (V) flow components for the southern (A and D), central (B and E) and northern (C, F) near-surfzone ADCP locations, using tideloc= 4 and 5% (blue), 2% (green) and 1.5% (red) of tidal signal reduction in the northern boundary.

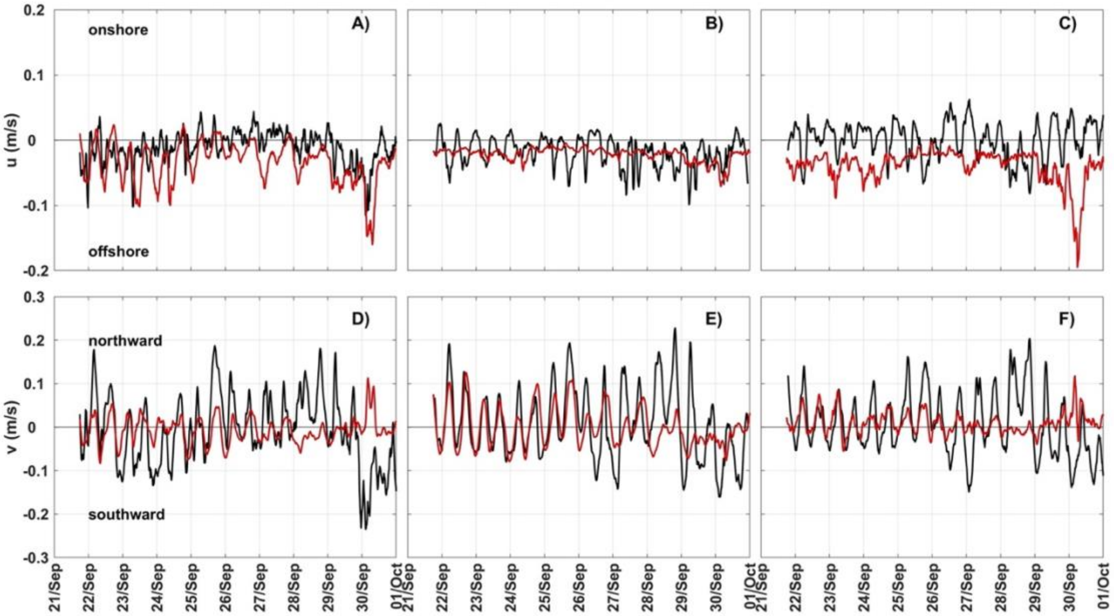

Figure C.2. 4. Modeled (blue lines) vs measured (black lines) cross-shore (U) and alongshore (V) flow components for the southern (A and D), central (B and E) and northern (C, F) near-surfzone ADCP locations, using tideloc= 4 and 1.5% (red) of tidal signal reduction in the northern boundary.

Table C.2. 1 Statistical results for tideloc = 4 and tidal signal reduced 5% at northern boundary.

Tidal signal reduced 5%									
STATISTIC TEST	**RSME**			**Bias**			**R**		
Variable/Site	**S**	**C**	**N**	**S**	**C**	**N**	**S**	**C**	**N**
Hs (m)	0.2	0.2	0.2	0.2	0.2	0.2	0.8	0.8	0.7
Tp (s)	0.4	0.6	1.1	-0.1	-0.1	-0.1	0.7	0.6	0.4
Dir (o)	7.0	4.4	16.9	4.5	5.1	4.4	0.5	0.5	0.6
u (m/s)	0.1	0.0	0.1	0.0	0.0	-0.1	0.4	0.3	0.2
v (m/s)	0.2	0.3	0.2	0.1	0.2	0.2	0.4	0.5	0.5

Table C.2. 2. Statistical results for tideloc = 4 and tidal signal reduced 2% at northern boundary

Tidal signal reduced 2%									
STATISTIC TEST	**RSME**			**Bias**			**R**		
Variable/Site	**S**	**C**	**N**	**S**	**C**	**N**	**S**	**C**	**N**
Hs (m)	0.2	0.2	0.2	0.2	0.2	0.2	0.8	0.8	0.7
Tp (s)	0.4	0.6	1.1	-0.1	-0.1	-0.1	0.7	0.6	0.4
Dir (o)	7.1	4.4	16.8	4.6	5.1	4.4	0.4	0.5	0.6
u (m/s)	0.0	0.0	0.1	0.0	0.0	0.0	0.4	0.2	0.3
v (m/s)	0.1	0.1	0.1	0.0	0.1	0.1	0.4	0.5	0.5

Table C.2. 3. Statistical results for tideloc = 4 and tidal signal reduced 1.5% at northern boundary.

Tidal signal reduced 1.5%									
STATISTIC TEST	**RSME**			**Bias**			**R**		
Variable/Site	**S**	**C**	**N**	**S**	**C**	**N**	**S**	**C**	**N**
Hs (m)	0.2	0.2	0.2	0.2	0.2	0.2	0.8	0.8	0.7
Tp (s)	0.4	0.6	1.1	-0.1	-0.1	-0.1	0.7	0.6	0.4
Dir (o)	7.0	4.4	16.8	4.4	5.0	4.3	0.4	0.5	0.6
u (m/s)	0.0	0.0	0.1	0.0	0.0	0.0	0.4	0.2	0.3
v (m/s)	0.1	0.1	0.1	0.0	0.0	0.0	0.3	0.5	0.4

C.3 Spatially varying wave spectrum at offshore boundary

To improve wave directionality for the northern section, the wave spectrum at the offshore boundary was spatially varied by dividing the boundary into 1, 6, and 16 segments (see Figure C.3.1). For the southern half of the boundary, the JONSWAP spectrum was defined using offshore ADCP data. For the northern half, wave spectral data were replicated from the offshore ADCP but adjusted by subtracting 50 degrees from the original time series (see Figure C.3.2). This approach notably improved nearshore wave directionality and current accuracy (Figure C.3.3 and Figure C.3.4), yielding better results for both wave integral parameters and current components (Table C.3.1 and Table C.3.2). Among the configurations, the 16-segment division demonstrated the best performance based on RMSE, Bias, and correlation values (R), making it the optimal setup for accurately reproducing wave and current characteristics in comparison with measurements.

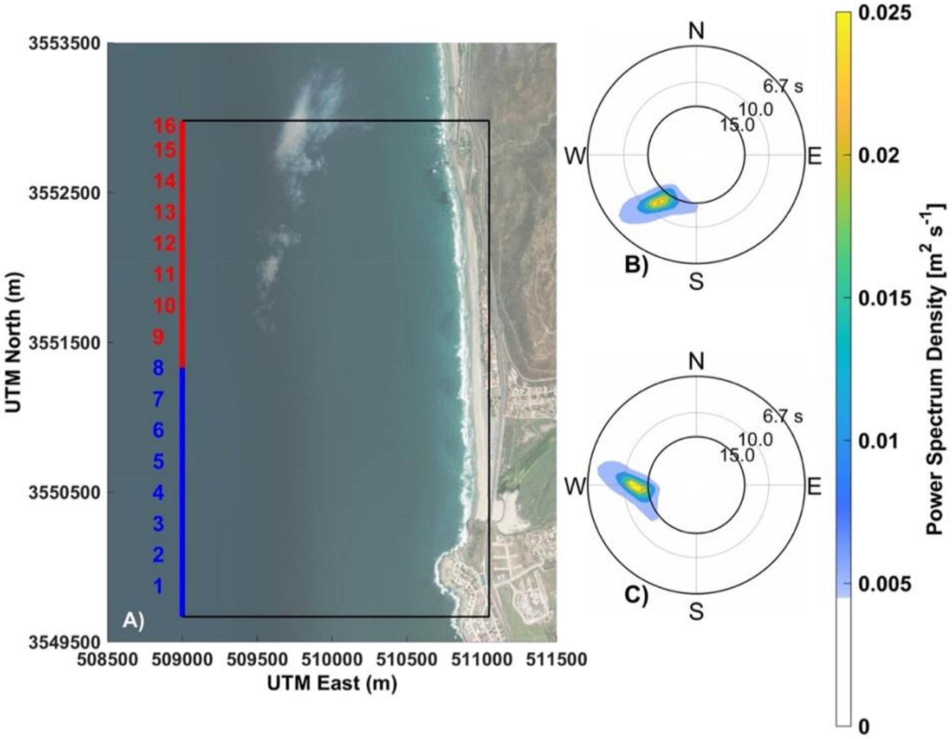

Figure C.3. 1. Model XBeach configuration denoting 16 segments for the offshore boundary A). JONSWAP mean directional wave spectrum for northern section (B). JONSWAP mean directional wave spectrum for southern section (C).

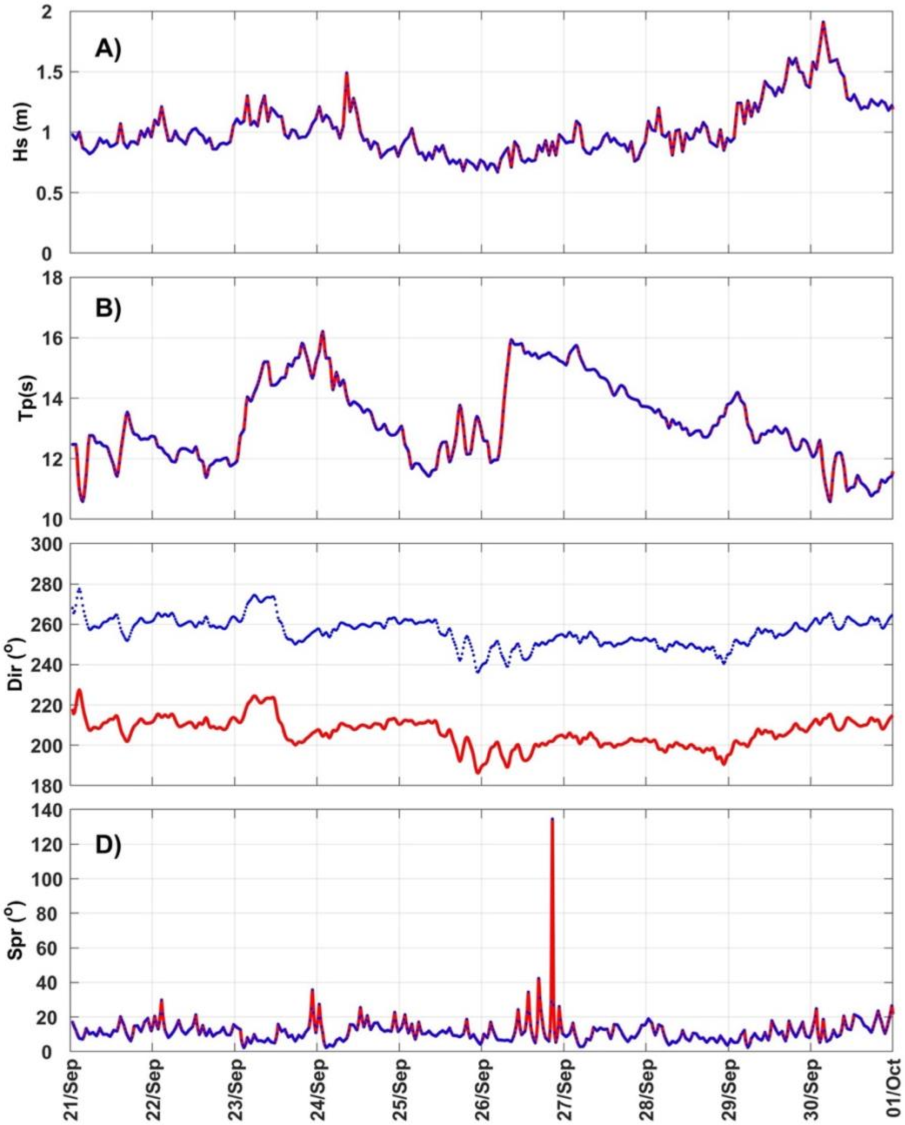

Figure C.3. 2. Wave integral parameters time series for the southern segments (blue) and northern segments (red). A) Hs. B) Peak period. C) Wave directionality and D) Wave directional spreading.

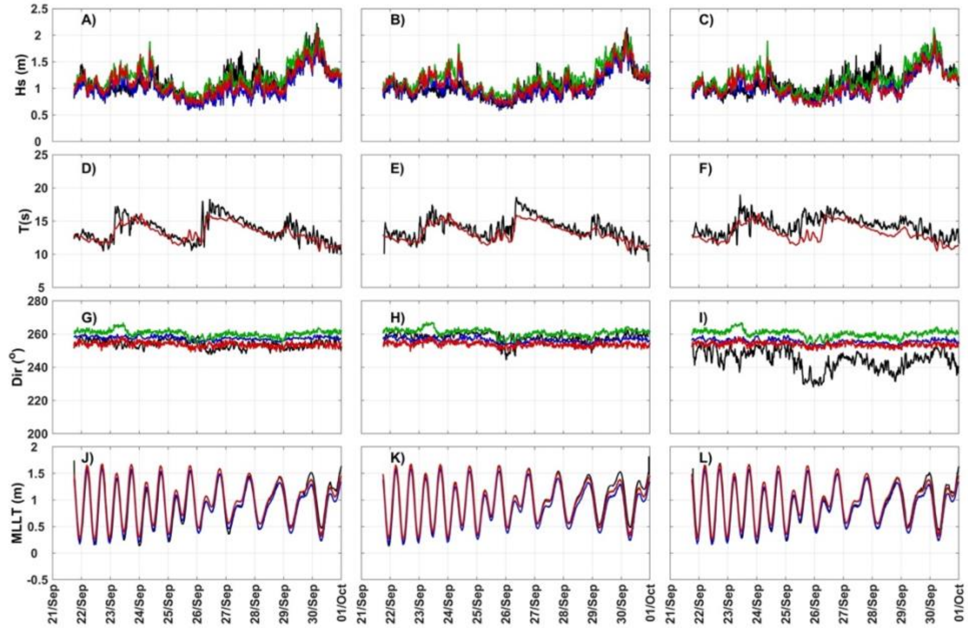

Figure C.3. 3. Modeled (color lines) vs measured (black lines) Hs, Tp, Dir and Tidal level (top to bottom) for the offshore ADCP location (left; A, E, I, M) and near-surfzone ADCPs in the South (B, F, J, N), Center (C, G, K, O) and North (D, H, L, P) nspectrum=: 1 (green), 6 (blue) and 16 (red) at the offshore boundary.

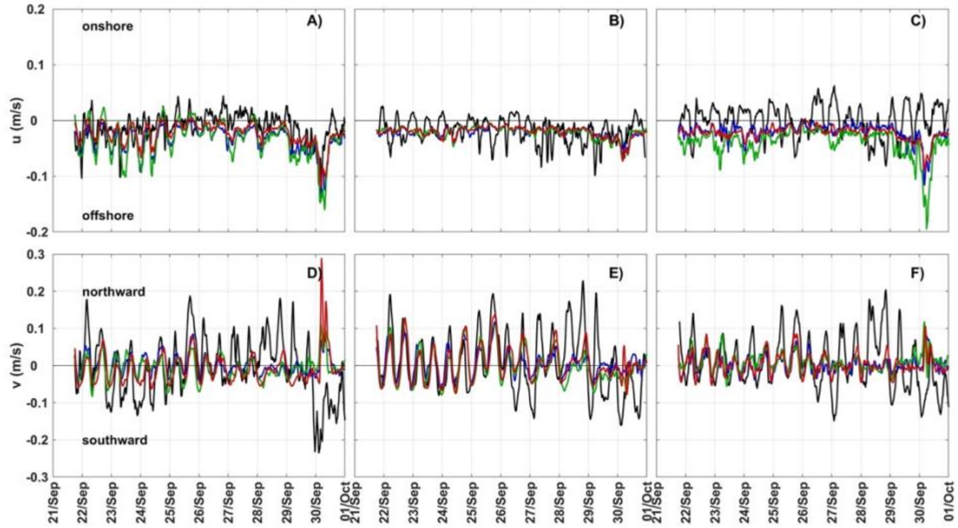

Figure C.3. 4. Modeled (color lines) vs measured (black lines) cross-shore (U) and alongshore (V) flow components for the southern (A and D), central (B and E) and northern (C, F) near-surfzone ADCP locations, using nspectrum=: 1 (green), 6 (blue) and 16 (red) at the offshore boundary.

Table C.3. 1 Statistical results for tideloc = 4 and tidal signal reduced 1.5% at northern boundary and homogenous wave spectrum on offshore boundary.

Nspectrum = 1									
STATISTIC TEST	**RSME**			**Bias**			**R**		
Variable/Site	**S**	**C**	**N**	**S**	**C**	**N**	**S**	**C**	**N**
Hs (m)	0.2	0.2	0.2	0.2	0.2	0.2	0.8	0.8	0.7
Tp (s)	0.4	0.6	1.1	-0.1	-0.1	-0.1	0.7	0.6	0.4
Dir (o)	7.0	4.4	16.8	4.4	5.0	4.3	0.4	0.5	0.6
u (m/s)	0.0	0.0	0.1	0.0	0.0	0.0	0.4	0.2	0.3
v (m/s)	0.1	0.1	0.1	0.0	0.0	0.0	0.3	0.5	0.4

Table C.3. 2 Statistical results for tideloc = 4 and tidal signal reduced 1.5% at northern boundary and offshore boundary segmented on 6.

Nspectrum = 6									
STATISTIC TEST	**RSME**			**Bias**			**R**		
Variable/Site	**S**	**C**	**N**	**S**	**C**	**N**	**S**	**C**	**N**
Hs (m)	0.2	0.1	0.2	0.0	0.0	0.0	0.8	0.8	0.7
Tp (s)	0.4	0.6	1.1	-0.1	-0.1	-0.1	0.7	0.6	0.4
Dir (o)	4.4	3.4	12.5	1.5	0.5	-0.4	0.5	0.5	0.8
u (m/s)	0.0	0.0	0.0	0.0	0.0	0.0	0.4	0.3	0.3
v (m/s)	0.1	0.1	0.1	0.0	0.0	0.0	0.4	0.6	0.4